2013-12

Manufacture and Investigation of Organic Composite Polymer Based Films for Advanced Flexible Solar Cells

Raffie Arshak
Technological University Dublin

Manufacture and Investigation of Organic Composite Polymer Based Films for Advanced Flexible Solar Cells

Raffie Arshak, B.Sc.

MPhil Thesis

Dublin Institute of Technology

Supervisors: Dr. Olga Korostynska, Dr. John Doran

School of Physics

Submitted December 2013

Abstract

Modern society has created big challenges in the area of sustainable supply of energy to satisfy the needs of growing population and to account for depleting fossil fuel resources. The Irish Government has set targets for the energy sector by 2020, with 33% of electricity to be generated from renewable sources. Organic photovoltaic devices offer several advantages over expensive silicon solar cells, including deposition of ultra-thin films by spin-coating, printing and spray-coating. This in turn provides for the exciting possibility to make lightweight, flexible solar cells for a broad range of existing and emerging applications for security, military and medicine.

This research project was inspired by the current drive into finding alternative technologies and materials for the design and manufacture of advanced solar cells. The primary objective was to tailor the properties of Poly3Hexylthiophene: PhenylC_{60} Buturic Acid Methyl Esther composite (P3HT:PCBM) thin films for flexible organic solar cells performance. The extensive experimental work was conducted to reveal the effect of the solar irradiation and thermal annealing on the dielectric, optical and electrical properties of P3HT:PCBM thin films. A common degradation pattern was demonstrated in the films after UV exposure whereby the optical absorbance and the resistivity were shown to be inversely proportionate. These two correlating techniques showed similar patterns after exposure. It was also shown that annealing the structure after deposition increased the absorbance in the thin film and the quantum efficiency of the final prototype device was related to film morphology.

The dielectric properties of these films were studied using a novel microwave spectroscopy technique and it is believed to be the first report on the application of this novel technique to photovoltaic materials characterisation.

To examine the dielectric properties of the P3HT:PCBM films using microwave spectroscopy, two types of Electro Magnetic (EM) wave sensors were fabricated, one on a Rogers substrate with Cu patterns and a second on a flexible substrate with Ag patterns. Both types of EM sensors exhibited shifts in resonant peak frequencies and amplitude during exposure to solar irradiation. All other experimental parameters and environmental conditions were kept constant. Therefore it is reasonable to conclude that the proposed method of microwave spectroscopy is a reliable tool to trace the changes in the properties of the materials caused by solar irradiation. The optical properties of the P3HT:PCBM films displayed a decrease in absorbance after 40mins solar simulator irradiation and then an increase in absorbance from 40 min to 20hrs. The electrical properties of P3HT:PCBM films showed a resistance decrease as the films were illuminated by a solar simulator from 0 to 40 min, and a subsequent increase in resistance up to 20hrs. In addition, a bespoke solar cell on flexible Polyethylene terephthalate (PET) was constructed and tested. It exhibited a fill factor and an efficiency of 0.3238 and 0.49% respectively. Although the performance is poor compared to reported state of the art for organic solar cells, the work demonstrates that operational devices can be manufactured under non-optimised laboratory conditions.

Declaration

I certify that this thesis entitled “Manufacture and Investigation of Organic Composite Polymer Based Films for Advanced Flexible Solar Cells” which I now submit for examination for the award of MPhil in Physics, is entirely my own work and has not been taken from the work of others, save and to the extent that such work has been cited and acknowledged within the text of my work.

This thesis was prepared according to the regulations for postgraduate study by research of the Dublin Institute of Technology and has not been submitted in whole or in part for another award in any other third level institution.

The work reported on in this thesis conforms to the principles and requirements of the DIT's guidelines for ethics in research.

DIT has permission to keep, lend or copy this thesis in whole or in part, on condition that any such use of the material of the thesis be duly acknowledged.

Signature _____ Date _____

Candidate: Mr Raffie Arshak

Acknowledgements

First and foremost, I would like to thank my supervisor Dr. Olga Korostynska for her excellent supervision, by giving me freedom in my work and engaging me in new ideas. In addition, I would like to thank my co-supervisor, Dr John Doran for his support during this work.

Thanks goes to all the members of FOCAS for their help on various issues during my research, it is greatly appreciated, and especially to Prof. Hugh Byrne and Dr. Manus Kennedy for their helpful discussions on various aspects of my research.

I would like to thank all the people who contributed in some many ways to the work described in this thesis, including John Harris and Declan McDonagh.

Thanks also, to my girlfriend Emma who was always there for me.

Finally, I would like to acknowledge and sincerely thank my parents, Arousian and Anto, who supported me in so many ways during my time here and in years past. Without them, I would not be the person I am today.

Abbreviations and Symbols

AFM	Atomic Force Microscope
A_g	Silver
AM	Air Mass
C_u	Copper
EM	Electro Magnetic
ε_r	Relative Permittivity
FF	Fill Factor
HFSS	High Frequency Structural Simulator
HOMO	Highest Occupied Molecular Orbital
IDE	Interdigitated Electrode
Imp	Current at Max Power
I_{SC}	Short Circuit Current
ITO	Indium Tin Oxide
J_{sc}	Short Circuit Current
LUMO	Lowest Unoccupied Molecular Orbital
OSC	Organic Solar Cell
OPV	Organic Photovoltaic

P3HT	Poly3Hexylthiophene
PCBM	PhenylC_{60} Buturic Acid Methyl Esther
PEDOT	Poly(3,4-ethylenedioxythiophene)
PET	Polyethylene terephthalate
PSS	Polystyrene sulfonate
PV	Photovoltaic
R_s	Series Resistance
R_{sh}	Shunt Resistance
SMA	Sub Miniature version A
TE	Transverse Electric
TEM	Transverse Electromagnetic
TM	Transverse Magnetic
UV	Ultraviolet
VIS	Visible
Vmp	Voltage at Max Power
VNA	Vector Network Analyser
V_{OC}	Open Circuit Voltage

Table of Contents

Abstract i

Declaration iii

Acknowledgements iv

Abbreviations and Symbols v

Table of Figures 5

Chapter 1: Introduction 10

Chapter 2: Operating Principles of Semiconductor and Organic Solar Cell 14

2.1. Foreword 14

2.2. Fundamentals of Traditional Semiconductor Photovoltaic Cells 15

2.2.1. PN Junction Structure 15

2.2.2. Operation and Characteristics of PN Junctions under Solar Illumination 15

2.2.3. Limitations of Modern Semiconductor PV Devices and Need for New Materials 21

2.3. Basic Processes in Organic Solar Cells 23

2.3.1. Absorption of Photons and Generation of Charge Carriers in Organic Materials 23

2.3.2. Efficient Organic Solar Cell Structures 27

2.4. Recent Advances in Polymer Solar Cells 27

2.4.1. Alternatives to ITO 28

2.4.2. Dye-Sensitised Solar Cells 30

2.5. Novel P3HT:PCBM Films for Flexible Solar Cells 32

Chapter 3: Experimental Procedure 35

3.1. Materials and Equipment Used 36

3.1.1. Q-Sun Xenon test chamber 36

3.1.2. UV-Vis 37

3.2. Organic Materials Films Preparation 38

3.2.1. Materials Mixture and Curing 38

3.2.2. Substrates 39

3.2.3. Spin-coating 39

3.3. Electrodes Design and Manufacture 42

3.3.1. Electrodes Pattern Design 42

3.3.2. Screen-Printing Technique 44

3.4. Testing the Optical Properties of the Films 49

3.4.1. Samples Preparation on Glass Slides 49

3.5. Organic Solar Cell Prototype Structure Design and Manufacturing Procedure 49

3.5.1. Deposition of Transparent Indium Oxide using Thermal Vacuum Evaporation 50

3.5.2. Bespoke Solar Cell Structure 56

Chapter 4: Results and Discussion 60

4.1. Structural Characterisation by AFM 60

4.2. Microwave Spectroscopy of P3HT:PCBM films 63

4.2.1. Brief review of microwave spectroscopy 63

4.2.2. Experimental setup for microwave spectroscopy measurements 77

4.2.3. Films reproducibility verification by microwave measurements 82

4.2.4. Solar Exposure Effects on a microwave sensor with a flexible polymer substrate and Ag pattern 84

4.2.5. Solar Exposure Effects on a Microwave sensor with a Rogers substrate and a Cu pattern 88

4.3. Optical Properties of P3HT:PCBM 93

4.3.1. Optical Properties of P3HT:PCBM Solutions 93

4.3.2. The effect of Annealing on the Optical Properties of P3HT:PCBM Films 95

4.3.3. The effect of Q-sun Exposure on the Optical Properties of P3HT:PCBM Films 96

4.4. Electrical Properties of P3HT:PCBM Films 98

4.5. Flexible Solar Cell Prototype Testing 102

Chapter 5: Summary, Conclusion and Future Work 106

References 108

Table of Figures

Figure 1. Solar radiation spectrum [15]. 14

Figure 2. (a) Dark I-V curve and (b) its downward shifting when light shines on pn-junction [21]. 16

Figure 3. Short circuit current (I_{SC}), open circuit voltage (V_{OC}), Fill Factor (FF) and Efficiency (η) of a solar cell [22]. 17

Figure 4. Energy band diagram of pn junction solar cell showing V_{oc} [23]..... 18

Figure 5. Simplified circuit model for a typical solar cell [22]. 22

Figure 6. Charge carrier generation in organic photovoltaics [42]..... 23

Figure 7. Donor-acceptor active layer (Bulk Heterojunction) concept [48]. 26

Figure 8. (A) Photograph of a graphene-coated PET substrate, and schematic diagram of the fabrication steps involved in preparing a DSSC with a graphene/PEDOT counter electrode on a PET substrate. (B) J–V characteristics of DSSCs using as counter electrode: graphene/PEDOT/PET (black), PEDOT/PET (green), and Pt/ITO/PET (red). (C) J–V characteristics of bended (•) and pristine (▪) DSSCs using PEDOT/graphene/PET as counter electrode [1]..... 30

Figure 9. Donor(left)−Acceptor(right) Pair for Polymer Solar Cells Containing Poly(3-hexylthiophene) P3HT (left) and [6,6]-Phenyl C61-Butyric Acid Methyl Ester PCBM (right) [5]. 32

Figure 10. Q-Sun Xenon test chamber in FOCAS Research Institute, DIT..... 37

Figure 11. Perkin Elmer Lambda 900 UV/VIS/NIR spectrophotometer for assessment of the optical properties. 38

Figure 12. Illustration of the spin coating process [82]. 40

Figure 13. SCS G3p–8 spin-coater. 41

Figure 14. a) Layout of an interdigitated electrodes pair; b) Dimensions of a single electrodes pair pattern in mm. 43

Figure 15. Photo of the bare thick film silver electrodes pair printed on Alumina substrate used for the electrical measurements of the films properties. 44

Figure 16. The screen printing process [86]. 46

Figure 17. DEK 1022 semi-automatic screen printer. 47

Figure 18. Typical thermal vacuum deposition system. The photo is taken in the laboratory of the FOCAS Institute, Dublin Institute of Technology. 51

Figure 19. Edwards E306A vacuum thermal coating system. 52

Figure 20. Bespoke mask used for evaporating Indium Oxide pattern in Edwards 306E system. 53

Figure 21. Evaporated Al illustrating the pattern for the transparent layer. 53

Figure 22. Experimental set-up for measuring sheet conductance of the deposited films. 55

Figure 23. Jandal four point probe. 55

Figure 24. Bespoke OPV Cell Layout. 56

Figure 25. (a) final manufactured prototype structure; (b) close-up view of the electrical connections. 57

Figure 26. Testing the electrical properties of the glass substrate cell. 59

Figure 27. MFP-3D-BIO AFM in FOCAS Research Institute, DIT. 61

Figure 28. AFM topographic image of the spin coated layer. (left) edge of a spin coated film (right) a scratch in the spin coated film. 62

Figure 29. Loop antenna coupling method [152]. 70

Figure 30. Block diagram of S-parameters for two ports cavity. 72

Figure 31. Coaxial cable. 73

Figure 32. N-Type and SMA coaxial cable connectors. 73

Figure 33. Typical microstrip transmission line [169]..... 74

Figure 34. PCB with microstrip transmission line connected to resistor [170]. 74

Figure 35. Electromagnetic wave sensor with printed metal pattern and light-sensitive P3HT:PCBM layer. 78

Figure 36. Optical image of the 3 pair IDE microwave sensor, which is bent to illustrate the flexibility of the polymer substrate [177]. 79

Figure 37. Optical image of a EM wave sensor head constructed on Rogers® substrate and having Cu metal patterns. 79

Figure 38. HFSS model of EM wave sensor field [177]. 80

Figure 39. Measurement setup showing VNA and a microwave sensor connected via coaxial cable [177]. 82

Figure 40. S_{11} signal distribution of the microwave sensor on Rogers substrate with Cu pattern in 0.01-15 GHz range when in contact with two P3HT:PCBM samples. 83

Figure 41. S_{11} signal distribution of the microwave sensor on flexible substrate with Ag pattern in 0.01-15 GHz frequency range when in contact with air and P3HT:PCBM films irradiated for 0, 1 and 20 hours. 85

Figure 42. S_{11} signal distribution of the microwave sensor on flexible substrate with Ag pattern in 0.6-1.4 GHz frequency range when in contact with air and P3HT:PCBM films irradiated for 0, 1 and 20 hours. 86

Figure 43. S_{11} signal distribution of the microwave sensor on flexible substrate with Ag pattern in 2.2-3.2 GHz frequency range when in contact with air and P3HT:PCBM films irradiated for 0, 1 and 20 hours. 87

Figure 44. S_{11} signal distribution of the microwave sensor on flexible substrate with Ag pattern in 6.0-10.0 GHz frequency range when in contact with air and P3HT:PCBM films irradiated for 0, 1 and 20 hours. 88

Figure 45. S_{11} signal distribution of the electromagnetic wave sensor on Rogers substrate with Cu pattern in 0.01-15.0 GHz frequency range when in contact with air and P3HT:PCBM films irradiated for 0, 1 and 20 hours. 91

Figure 46. S_{11} signal distribution of the microwave sensor on Rogers substrate with Cu pattern in 6.5-8.5 GHz frequency range when in contact with air and P3HT:PCBM films irradiated for 0, 1 and 20 hours. 92

Figure 47. Illustration of the spectra for PCBM, P3HT and PCBM:P3HT solutions. ... 94

Figure 48. UV-Vis absorption of P3HT:PCBM thin films spin coated from 1,2 dichlorobenzene (1:1) annealed and dried naturally. 96

Figure 49. Screen-shot images that trace the changes in the optical absorption spectra after 0, 10 min, 20 min, 40 min and 20 hours of irradiation. 98

Figure 50. Measurement points for the electrical characterisation of the films. 99

Figure 51. Dependence of the resistance on exposure time for the four samples at MP.1. 100

Figure 52. Dependence of the resistance on exposure time for the four samples at MP.2. 101

Figure 53. Experimental setup for solar cell prototype characterisation. 102

Figure 54. Pyranometer from Kipp & Zonen, for measuring the simulated solar irradiance/light intensity..... 103

Figure 55. Graphical interface illustrating the electrical properties of a commercially available solar cell. 103

Figure 56. (a) Current-voltage characteristics of the prototype solar cell and (b) the dependence of power on voltage. 104

Chapter 1: Introduction

Solar cells are designed to directly convert solar energy to electrical power. Inorganic solar cells, especially silicon-based, have been industrialised for a long time because of their high power conversion efficiencies [1]. However, they suffer from high costs and serious pollution problems. Organic solar cells (OSCs) are regarded as promising alternatives to traditional first and second generation solar cells [2-4]. Therefore, the research investigations in finding innovative materials, technologies and structures for solar cells to satisfy this demand are ongoing. Organic solar cells are of considerable importance for use as the next-generation renewable energy sources. Their low cost and high flexibility make OSCs attractive candidates as cost-effective and flexible power sources, with vast potential for a range of novel applications.

Polymer solar cells are a new type of photovoltaic conversion device with high potential applications in the future energy market since their unique advantages in potential low-cost production, their flexibility, and light weight. In contrast to many inorganic semiconductors, in which photon absorption directly produces free electrons and holes, optical absorption in organic molecular and polymer semiconductors mainly creates electron−hole pairs (excitons) that are bound at room temperature [5].

A special focus in this thesis is made on the materials deposition techniques, as through tailoring the properties of active layers, the efficiency of the overall solar cell can be increased. In particular, the thin film technology was used due to its cost-effectiveness and flexibility in using various substrates and materials, in line with the recent developments that suggest that this technology is becoming a prime candidate for future organic photovoltaic (OPV) devices.

Notably, OPVs structures utilizing semiconducting conjugated polymer photoactive layers offer several advantages over expensive silicon solar cells, including deposition of ultra-thin films by simple solution processing technologies such as spin coating, printing and spray coating. For bulk heterojunction structures, which use an active layer made of an intimate mixture of donor and acceptor materials, energy conversion efficiency as high as ~7% could be obtained with a poly-(3-hexylthiophene) (P3HT) and [6,6]-phenyl-C61 butyric methyl ester (PCBM) blend. Theoretical investigations predict for these materials an efficiency reaching 11%, which is significantly higher than the best performance of present devices [6-8].

The production of polymers is less financially demanding as compared to traditional Si wafers, which are the basis for the first-generation solar cells. Additionally, polymers normally have high optical absorption coefficient and therefore very little material is needed. Polymers can be dissolved in solvents and deposited on substrates using wet-processing techniques such as spin coating or roll-to-roll printing [9]. Organic solar cells are also attractive because they lack a rigid crystalline lattice and can be deposited in flexible substrates. Currently available in the market are up to 180W flexible solar panels with 20% efficiency manufactured by companies such as Longsheng Electric Co., Ltd.. These are being used to power street lights and other outdoor LED lighting systems for example.

However, technological improvements in new material synthesis and device fabrication approaches are necessary for enhancing the solar cell performance to meet the modern industry demands. In this context, the field of Organic solar cells can learn much from the area of organic light emitting devices, which has already realised commercial exploitation.

This thesis, entitled “Manufacture and Investigation of Organic Composite Polymer Based Films for Advanced Flexible Solar Cells”, reports on the research work undertaken towards the development of next-generation organic polymer composite materials for flexible solar cell applications. In particular, it investigates the use of non-optimised laboratory conditions to produce prototype devices and establish the effects of thermal annealing, commonly employed in production of commercial devices [10-14], and exposure to simulated solar radiation, to mimic operational conditions. The work therefore explores the possibility of producing operational devices under non-capitally expensive conditions, without the need of clean rooms etc., as may be encountered in third world countries To achieve this aim, thin film technology was used because recent developments suggest that it is becoming a prime candidate for future photovoltaics due to its versatility in terms of both deposition of functional materials and the range of substrates compatible with the process requirements.

The thesis structure is as follows. Chapter 1 has briefly outlined the area of research and justified the need for developing new materials and manufacturing techniques for sustainable solar cells. Chapter 2 reviews traditional pn-junction based solar cells and the factors that limit their performance, along with discussing the state-of-the-art organic solar cells.

Chapter 3 details the Experimental Procedure employed in this research work, including the materials and equipment used, electrodes design methods and parameters, preparation procedure for organic films, and testing arrangements for the electrical and optical properties characterisation.

Chapter 4 focuses on the Results of these optical and electrical tests, with specific emphasis on novel approach to characterise the dielectric properties of the materials

using the microwave spectroscopy. The fundamental principles of operation and design of sensors for this task are thoroughly discussed. As a culmination of the research experiments, the bespoke prototype organic solar cell was designed and tested and the performance of this device is also discussed at the end of this Chapter.

Finally, Chapter 5 concludes the description of the research outcomes so far and suggests directions and options for future work in this area.

Chapter 2: Operating Principles of Semiconductor and Organic Solar Cell

2.1. Foreword

Modern society is confronting big challenges in the area of sustainable supply of energy to satisfy the needs of growing population and to account for depleting fossil fuel resources. Naturally, solar cell devices are considered as a sustainable and secure approach to solve this issue.

Solar radiation emitted from the sun is electromagnetic radiation with the spectral solar radiation distribution in the wavelength range of 200 - 2500 nm, which includes the total irradiance of 96.3% and most of the remaining 3.7% at longer wavelengths as shown in Fig. 1 [15].

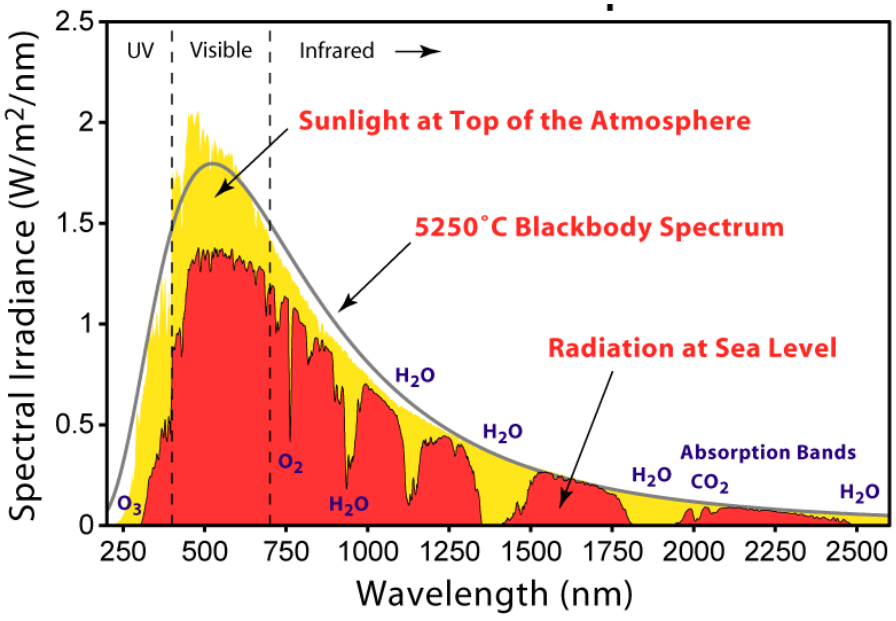

Figure 1. Solar radiation spectrum [15].

2.2. Fundamentals of Traditional Semiconductor Photovoltaic Cells

2.2.1. PN Junction Structure

In traditional inorganic photovoltaic devices the pn-junction structure is responsible for conversion of sunlight into electrical energy. A pn-junction is formed by combining a positively doped (P-type) and a negatively doped (N-type) semiconductor together. A P-type semiconductor is achieved by diffusing elements that have three valence electrons, such as Boron, onto a silicon wafer. This creates positively charged holes on the crystalline silicon matrix. The N-type semiconductor has elements with five valence electrons, such as Phosphorus, that are scattered throughout the silicone lattice. When P and N type semiconductors are combined, the electrons close to the junction or boundary diffuse into the P-type region. Charge builds up upon the interface of the two materials, creating an electric field which opposes the flow of electrons. This region is known as the depletion zone [16, 17].

Valence electrons in the silicon semiconductor absorb photons (in the visible range), that have enough energy to excite electrons across the semiconductors bandgap. The region where this occurs is determined by the materials constructing the device. The intrinsic electric field separates the electron and its positively charged hole. Electrons flowing in the direction of the electrode to the N-type side flow through an external load to produce power [18].

2.2.2. Operation and Characteristics of PN Junctions under Solar Illumination

When solar radiation is absorbed by a pn-junction, electron-hole pairs are generated. If the radiation of the solar radiation is weakly absorbed by the material (long wavelength radiation) then the generation rate of electron-hole pairs will be uniform in the volume

of the solar cell. Under illumination, generation of carriers will occur in the space charge region [19]. If an electric field is applied across the junction, these carriers will be swept away by the electric field (electrons to the N-side and holes to the P-side). The electric field reduce the recombination effect. This causes a build-up of positive and negative charge causing a potential difference. The generation of this voltage is called the photovoltaic effect [20].

In a pn-junction, four types of the electrical currents are present under equilibrium; these are due to the movements of electrons, holes, caused by a drift and diffusion. When light shines on a pn-junction, large drift current results from minority electrons and holes. This is called light generated current I_L. The generated voltage forward biases the pn-junction and diffusion current flows in the opposite direction. But I_L is larger than this diffusion current, so the resultant current flows from N to P. This causes the I-V curve to shift downwards, as shown in Fig. 2 [19].

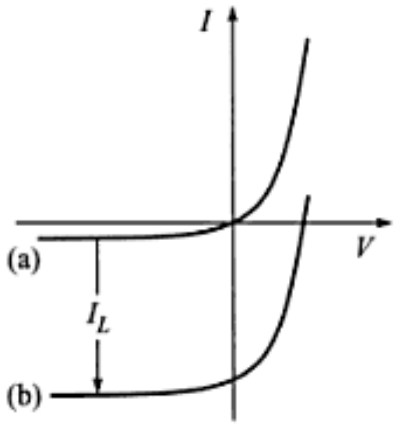

Figure 2. (a) Dark I-V curve and (b) its downward shifting when light shines on pn-junction [21].

When solar cells are characterised, four parameters are calculated from the I-V curve, namely: short circuit current (I_{SC} or J_{SC}), open circuit voltage (V_{OC}), Fill Factor and

Efficiency, as illustrated in Figure 3. The short circuit current (Jsc), is the maximum currents that flows in the solar cell when both terminals are shorted and it increases as the light intensity increases. The open circuit voltage (Voc) is the voltage between the terminals when no current is drawn. Two additional terms are shown in Figure 3 [22], I_{mp} and V_{mp} where I_{mp} is the current at a maximum power and Vmp is the voltage at a maximum power.

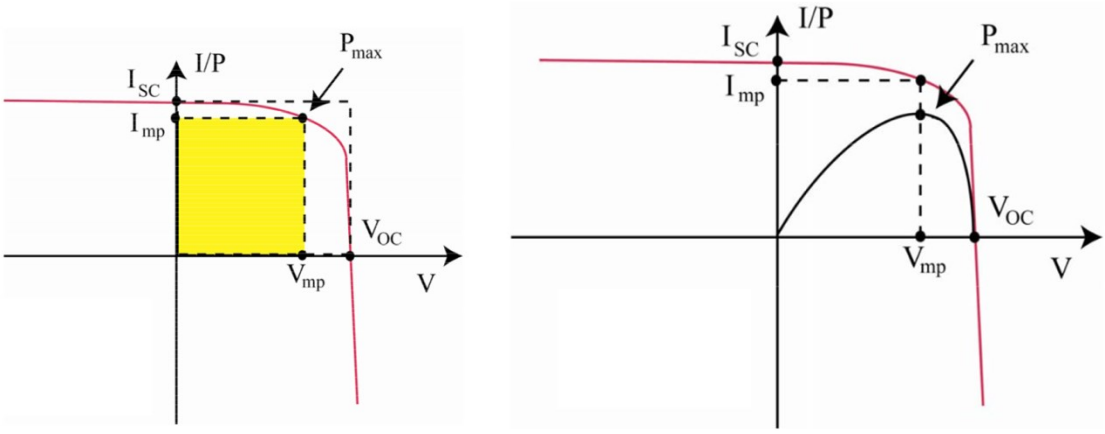

Figure 3. Short circuit current (I_{SC}), open circuit voltage (V_{OC}), Fill Factor (FF) and Efficiency (η) of a solar cell [22].

In order for a photon to be absorbed, the photon must have energy higher than the bandgap of the material in the solar cell. Therefore, the value of I_{SC} current depends on the bandgap of the cell, and the larger the bandgap, the smaller number of photons will be absorbed.

The power from a power source is P = IV. If one uses the current density J, the power density is expressed by Eq. 1:

$$P_d = JV \qquad \text{Eq. 1}$$

The maximum power density, P_{max}, occurs somewhere between V = 0 (short circuit) and $V = V_{oc}$ (open circuit) at a voltage V_m, as illustrated in Fig. 3. The corresponding current density is called J_m, and thus the maximum power density is $P_{d,m} = J_m V_m$.

When a photon of light is absorbed, the electron moves from the valence band to the conduction band, raising its potential energy by an amount equal to the bandgap of the material (E_g.) Ideally, if there are no potential drops across the metal contacts, then the maximum V_{oc} is equal to the bandgap voltage. If one takes into account the difference in potential level of the contacts, a more accurate estimation of the maximum Voc can be obtained. Fig. 4 shows how the Fermi levels influence the Voc:

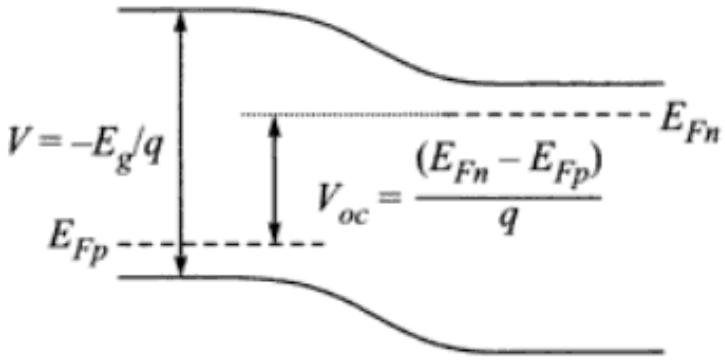

Figure 4. Energy band diagram of pn junction solar cell showing V_{oc} [23].

In Figure 4, E_{Fn} and E_{Fp} are the Fermi levels in the N-side and the P-side respectively [23]. In a band structure the Fermi level is a hypothetical energy level of an electron, with a corresponding probability of 50 %. The influence of the current due to illumination (I_L) and the recombination current (I_o) on the open circuit voltage is described by Eq. 2:

$$V_{OC} = \frac{kT}{q} ln\left(\frac{I_L}{I_o} + 1\right) \qquad \textit{Eq. 2.}$$

where k is Boltzman's constant, T is the temperature is degrees Kelvin and q is the charge in the electron. Fill factor is a measure of how 'ideal' the IV curve is – it is a measure of how much of area described by I_{SC} and V_{OC} is filled by the area described by I_{mp} and V_{mp}. FF is defined as the ratio between the maximum power and ideal power by Eq. 3:

$$FF = \frac{J_m V_m}{J_{sc} V_{oc}} \qquad Eq.\ 3$$

Ideally, the maximum FF is 1, which is not practically feasible. The shunt resistance (R_{sh}) or parallel resistance in a solar cell represents the losses or additional current paths due to manufacturing defects. The series resistance (resistances in series with the solar cell) can be broken into a number of series components, the contact resistance between the metal electrodes and the active layer, the resistance of the metal electrodes themselves and the resistance of the active layer itself. All these resistances are measurable and controllable when choosing the functional materials for photovoltaic devices.

The efficiency (η) of a solar cell is defined as the power output divided by the power input. If the incoming light has a power density P_{in}, the efficiency will be described by Eq. 4:

$$\eta = \frac{J_m V_m}{P_{in}} \qquad Eq.\ 4$$

Efficiency gives a measure of how much of the open circuit voltage and short circuit current is used at maximum power. Using FF, the efficiency can be expressed as Eq. 5:

$$\eta = \frac{J_{sc} V_{oc}\, FF}{P_{in}} \qquad Eq.\ 5$$

Efficiency is related to the bandgap of the active layer in the solar cells. Therefore, depending on the type of solar cell materials used, a maximum efficiency can be achieved. The bandgap for most organic solar cells is usually 2 eV or above. The maximum efficiency of the overall device can be increased with the use of multi-layer solar cells. For example, triple layer cells with concentrator optics are as high as 42.8% efficient [24]. For organic solar cells manufactured by Konarka, an OPV company based in Massachusetts, an efficiency of 8.3% wa quoted [25], with the current record value for organic devices being achieved by Mitsubishi chemical at 11.1% [26].

The input power (P_{in}) can be represented in terms of solar cell area (A_{sc}) and the input light (E) in W/m^2 in accordance to Eq. 6:

$$P_{in} = E\, A_{sc} \qquad Eq.\ 6$$

Importantly, solar cell efficiencies are measured under standard test conditions (STC), which imply a temperature of 25 °C, an irradiance of 1000 W/m^2 with an air mass 1.5 (AM 1.5) spectrum [27]. These conditions correspond to a clear day with sunlight incident upon a sun-facing 37°-tilted surface with the sun at an angle of 41.81° above the horizon [28]. This represents solar noon near the spring and autumn equinoxes in the continental United States with surface of the cell aimed directly at the sun. Under these test conditions, a solar cell of 20% efficiency with a 100 cm^2 surface area would produce 2.0 Watts of power.

However, the solar cell efficiency is affected by a range of factors, which can be examined by looking at all the losses in the conversion of the light from the sun to current and voltage generated in the solar cell. The operational limitations of traditional semiconductor solar cells are briefly discussed in the next section.

2.2.3. Limitations of Modern Semiconductor PV Devices and Need for New Materials

Understanding the efficiency limitations of solar cells is the most important task in their characterisation because it can lead directly to improvements in the cell process. Reduced efficiency of solar cells can be due to limitations of material properties or technological reasons, such as cell processing capabilities. Transmission losses occur due to low energy photons not being absorbed by the cell (typical 20% for single junction Si based cell) [29, 30]. Maximum efficiency of an ideal single-junction photovoltaic cell is limited to 33% (for 1 sun illumination) by intrinsic losses such as band edge thermalisation, radiative recombination, and inability to absorb below-bandgap photons. This intrinsic thermodynamic limit, named after Shockley and Queisser, can be exceeded by utilising low-energy photons either via their electronic up-conversion or via the thermophotovoltaic conversion process [31]. However, electronic up-conversion systems have extremely low efficiencies, and practical temperature considerations limit the operation of these converters to the narrow-gap PV cells [29].

The thermal losses exist due to excess energy photons, because photon with energy equal to the band gap of the material will be absorbed. For photons having energy higher than the bandgap, their excess energy will be released as heat. This can be as high as 30% [32].

Figure 5 [22] shows a simplified circuit model for a typical solar cell. It can be seen that a Fill Factor loss is caused by the parasitic series (R_s) and shunt resistance (R_{sh}) of the cell.

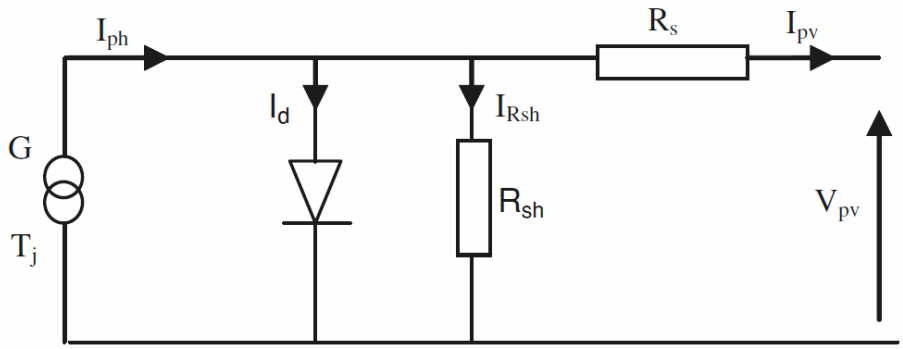

Figure 5. Simplified circuit model for a typical solar cell [22].

The next categories of losses are optical and electrical losses such as losses due to reflection, incomplete absorption, metal coverage and recombination losses [33, 34]. Reflection losses occur since some of the incident photons are reflected from the cell surface. This loss can be minimised by the use of anti-reflective coating [35-37]. Notably, recombination losses refer to the fact that not all electron-hole pairs contribute to the generated current and they can occur in the bulk or on the surface of the solar cell device [38-40].

Incomplete absorption is a function of solar cell thickness. Since most solar cells are becoming thinner and thinner, light trapping schemes can be used to enhance absorption. For example, the imprinting of random square based pyramidal textures with micrometric scale at the air/glass interface of thin film silicon solar cells was suggested as an efficient alternative to anti-reflective coatings to minimise reflection losses at the cell entrance [41].

To overcome the limitations in the performance of traditional solar cells due to constrains set by their functional materials properties, there is a need to develop new approaches and materials that would convert solar irradiation into electricity. For that,

organic solar sensitive materials are considered as a prime candidate. The next section briefly reviews the structure and operational principles of modern organic solar cells.

2.3. Basic Processes in Organic Solar Cells

2.3.1. Absorption of Photons and Generation of Charge Carriers in Organic Materials

Organic photovoltaics can be categorised by the types of Donor-Acceptor materials used to fabricate the device. The materials in OPV's are generally conjugated polymers or molecules (alternating single and double bonded carbon) and possess delocalised (not associated with single atom) electrons that can absorb photons. The molecular structure determines the electronic properties and depending on that structure, they can be classed as either electron donors or acceptors as shown below in Figure 6.

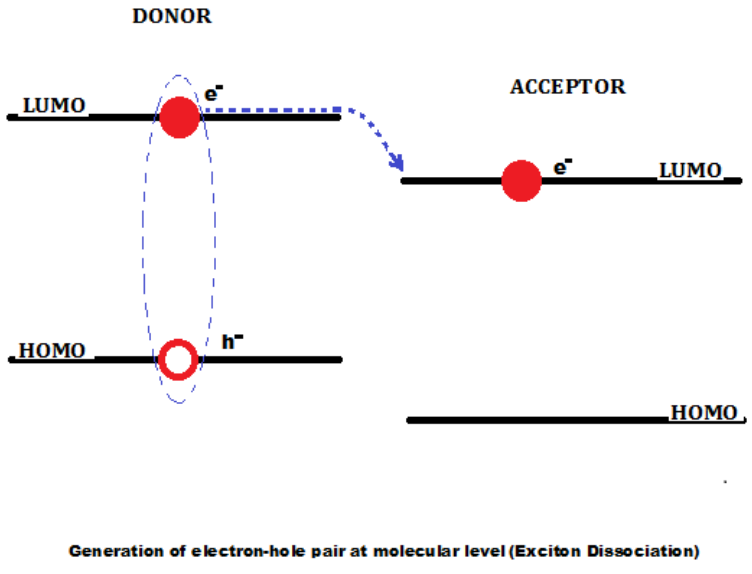

Figure 6. Charge carrier generation in organic photovoltaics [42].

In organic semiconductors the absorption of photons results in the formation of bound electron hole pairs, i.e. excitons, rather than free charges. The transfer of charges can be made possible at the interface between two materials providing that one material has the highest occupied molecular orbital (HOMO) and lowest unoccupied molecular orbital (LUMO) levels lower than the other. The one with the higher LUMO can accept an electron from the conduction band of the other and is therefore called electron acceptor (A). So, the other material is the electron donor (D) [42]. An organic photovoltaic cell works in a complementary fashion. Light is absorbed in either of two donor (D) or acceptor (A) layers, creating excitonic states which must diffuse to the D/A interface where differences in ionization potential and electron affinities of D and A cause these excited states to dissociate into free charge carriers (electrons and holes residing on molecular species). The combination of diffusion and migration of these charge carriers to the collection electrodes, and the harvesting of these charges by these electrodes, produces a current in the external circuit, and a specific voltage, the product of which is the power produced by the OPV.

Consequently, an electron acceptor can act as an electron donor for another electron acceptor which is weaker. An electron in HOMO absorbs a photon and is excited into LUMO and creates an exciton, a bound electron-hole pair. These excitons carry energy but no net charge and may diffuse to dissociation sites where their charges can be separated [43]. The separated charges then travel to the device electrodes, the holes travel to the anode and the electrons travel to the cathode. This produces a voltage and a current. A crucial step in the photovoltaic process is the conversion of excitons into charge carriers at a polymer–inorganic interface, i.e., at the interface between the active layer and the inorganic electrode. High quantum yield of charge carriers can be achieved if the excitons can travel far enough from their generation points to an

appropriate interface where they can dissociate, injecting electrons into the electrode [44]. The holes remaining in the polymer diffuse to the other electrode, completing the photovoltaic cycle. Some of the excitons reach relevant interfaces while many of them decay by emitting light, or exciting vibrations of the polymer molecules. Table 1 summarises the conversion steps of light photons into separated charges in an organic solar cell. In addition, the loss mechanism and the related electrical quantity used in the circuit model are shown.

Table 1. Light conversion steps and associated loss mechanisms.

Conversion step	Loss Mechanisms
Light adsorption, exciton creation	Reflection, transmission
Exciton diffusion	Recombination of excitons
Charge separation	Excitons transfer followed by their recombination; no charge separation followed by the recombination of excitons
Charge transport	Recombination of charges, limited mobility of charges
Charge collection	Recombination near electrodes, barriers at the electrodes

In most organic devices, only a small fraction of the incident light is absorbed. A bandgap of about 1.1 eV is required to absorb about 77% of solar radiation, while most polymers have a bandgap of more than 2 eV, and thus can only absorb about 30% of light. The absorbing layer is also quite thin in most photovoltaic devices, less than 100 nm [45].

The free charges must be allowed to reach the electrodes where they constitute the photocurrent from the device. The location of the dissociation site is important for the extracted photocurrent. Electrons and holes have different mobilities in the material.

Trapping into localised stated may occur and irrespective of whether the trapping is permanent or temporary, the efficiency of charge transport is diminished. As the risk for trapping increases with the distance travelled, a thin layer is better than a thick layer, but optical absorption, which is proportional to thickness, is simultaneously reduced. Recombination of free charge carriers into excitons, and between one trapped and one free carrier, is also another loss mechanism [46].

Even if an electron or a hole is present close to an electrode, whether they will pass into the outer circuit is not certain. The probability associated with all the barrier penetration mechanisms involved at the interfaces towards the metallic surfaces is a function of geometry, topology, and interface formation [47].

Initial organic solar cell structures used overlayed thin films of donor and acceptor materials, and the efficiency of the structures depended on the interface area and integrity. The interface area was then increased by including alternating layers, but a significant advancement was realised through the use of so-called "bulk heterojunction" structures, which exploited the fact that the structures could be deposited from binary solvent based mixtures and that the donor could be homogeneously dispersed in the acceptor matrix, or vice versa as shown in Figure 7, where red indicates the electron donor material and blue the electron acceptor material.

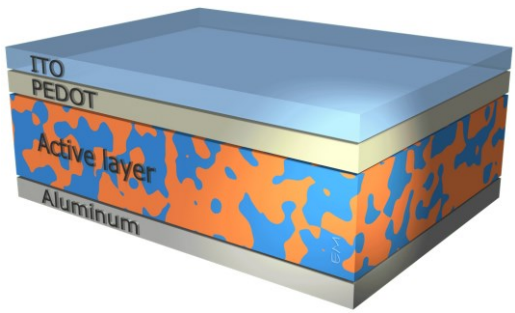

Figure 7. Donor-acceptor active layer (Bulk Heterojunction) concept [48].

2.3.2. Efficient Organic Solar Cell Structures

To obtain an efficient organic solar cell, all excitons created should form free charge carriers. However, during exciton transport luminescence or radiative recombination can occur [49, 50]. The exponential lifetime of an exciton (τ_{EX}) is determined by the reciprocal value of radiative and non-radiative decay rates. For an efficient solar cell, all excitons must reach the interface within τ_{EX} secs. The transport of the excitons occurs by diffusion and the distance an exciton is able to travel, L_{EX}, is determined by Eq. 7:

$$L_{EX} = \sqrt{D_{EX} \cdot \tau_{EX}} \qquad Eq.\ 7$$

where D_{EX} is the diffusion coefficient of the excitons. A typical time for τ_{EX} is in nanoseconds so the distance L_{EX} is less than 10 nm [51]. This means that only excitons formed very close to the interface will have a chance to separate. This limitation has stimulated the development of different types of solar cell structures.

2.4. Recent Advances in Polymer Solar Cells

Organic solar cells are of considerable importance for use as the next-generation renewable energy sources. In particular, low cost and high flexibility, key features that organic-based electronics can offer, make OSCs attractive candidates as cost-effective and flexible power sources based on roll-to-roll manufacturing and large-area processability on flexible substrates [52].

2.4.1. Alternatives to ITO

The ideal transparent conducting electrode should possess high transparency (>80%), low resistance (<100 Ω/m^2), and an appropriate work function (4.5–5.2 eV) [1]. The cost of the transparent conducting electrodes is also an important issue for considering their practical applications. Among key materials for OSCs, transparent Indium Tin Oxide (ITO) electrodes play an important role in the performance of OSCs, since the fill factor and short-circuit current density are critically dependent on the series resistance and optical transmittance of the transparent electrodes [53]. Although ITO dominates modern industry in terms of production of OPV, the scarcity and high cost of indium, which is the main element in the ITO electrode, coupled with the cost of the manufacturing process, and ion diffusion into polymer layers, are critical drawbacks of ITO-based OSCs. In particular, ITO cannot be used for flexible devices because it is mechanically rigid and brittle. Also, the energy involved in processing the ITO electrode accounts for 87% in roll-to-roll based OSC fabrication [54]. These issues drive the researchers and industry to seek possible alternative materials [6-8, 55-61].

To overcome the drawbacks of ITO electrodes, the use of indium-free transparent electrodes such as PEDOT:PSS, carbon nanotube (CNT) electrodes, graphene electrodes, and several indium-free oxide electrodes (Ga-ZnO, Al-ZnO, $ZnSnO_3$, Nb-TiO_2) has been the focus of recent research [52].

Graphene has wide potential applications in energy-related systems. In particular, transparent graphene electrodes fabricated by various methods have been investigated as a promising alternative to ITO electrodes due to their low resistance, high transparency, superior flexibility, and low cost [62-65]. The single atom thickness of Graphene, its high conductivity, optical transparency (97.7%), flexibility and low sheet resistivity

make this material an emerging adequate substitute for ITO, especially for ultra-thin or flexible photovoltaic devices [66, 67]. Also this material is in high demand for the touch screen display in today's modern tablet computers and smart phones, and is potentially suitable for flexible solar cells applications when portable solar cells will be integrated into these devices. Transparent graphene thin films can be prepared using a variety of techniques including micromechanical exfoliation, epitaxial growth and chemical vapour deposition [1].

Graphene materials are frequently blended with polymers to form composites, especially when fabricating flexible devices. Graphene/polymer composites have been explored as electrodes of super-capacitors or lithium ion batteries, counter electrodes of dye-sensitized solar cells, transparent conducting electrodes and active layers of organic solar cells, catalytic electrodes, and polymer electrolyte membranes of fuel cells [1]. Graphene/polymer composites can be synthesised by mixing, in situ polymerisation, and covalent modification [68-70].

Poly(3,4-ethylenedioxythiophene):poly(styrene sulfonate) (PEDOT:PSS) composite materials have attracted significant interest as a promising electrode material to substitute the ITO due to their inherent advantages such as high conductivity, high transparency in the visible range and long-term stability [52]. Various modifications of PEDOT:PSS to have more enhanced conductivity for their potential use as electrodes in ITO-free organic-based devices were produced and investigated, including the use of high-conductivity PEDOT:PSS, such as Clevios PH500, which resulted in fabrication of ITO-free OSCs with efficiencies comparable to traditional ITO-based OSCs [71].

To illustrate the typical structure of DSSC and a schematic diagram of the fabrication process steps, one may refer to Fig. 8 [1], which also depicts J-V characteristics of DSSC with various electrodes alternative to ITO.

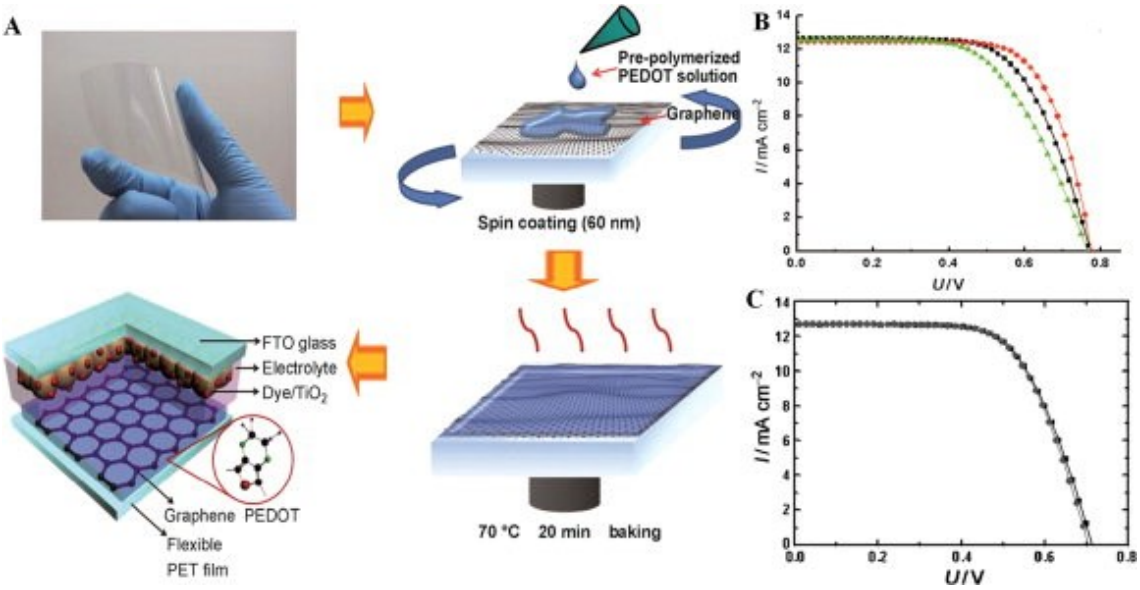

Figure 8. (A) Photograph of a graphene-coated PET substrate, and schematic diagram of the fabrication steps involved in preparing a DSSC with a graphene/PEDOT counter electrode on a PET substrate. (B) J–V characteristics of DSSCs using as counter electrode: graphene/PEDOT/PET (black), PEDOT/PET (green), and Pt/ITO/PET (red). (C) J–V characteristics of bended (•) and pristine (▪) DSSCs using PEDOT/graphene/PET as counter electrode [1].

2.4.2. Dye-Sensitised Solar Cells

Dye-Sensitised Solar Cells (DSSCs) have received great attention because of their low cost, convenient manufacturing processes, and comparable efficiencies to those of solid-state silicon solar cells [72]. In DSSCs, the dye, usually ruthenium bipyridyl, is excited by incident photons. Electrons of the dye are injected to the titania mesoporous nanocrystalline wide band gap semiconductor and transported through the nanoparticles network by trap mediated diffusion [73]. The dye is regenerated by popular

iodine/iodide redox couples in electrolyte. Increasing the efficiency of these cells is strongly related to the photon absorption, charge injection, charge transport, dye regeneration efficiencies, open circuit voltage, and fill factor of the cell. Although the efficiency of the DSSCs have reached so far 12% [74], it can be further improved by overcoming obstacles through (1) increasing cell stability by replacing the volatile electrolyte with nonvolatile or solid state electrolyte without affecting diffusion of ions, (2) increasing the absorption efficiency by engineering the dye molecule or increasing the thickness without increase in recombination or decrease in electron lifetime, and (3) increase in electron transport by introducing high mobility routes in semiconductor matrix or hindering the back reaction by utilizing suitable barrier layer [73].

Typical DSSC consist of a working electrode of mesoporous dye-sensitised titania nanocrystals coated on transparent conducting electrode, an electrolyte containing a redox pair (for example I_2/I_3^-), and a platinum-based counter electrode [1]. Ruthenium sensitiser-based DSSCs have a photon conversion efficiency reaching 11.9%, which gives an open circuit voltage (V_{oc}) of 965 mV, a short circuit current density (J_{sc}) of 17.3 mA cm^{-2}, and a fill factor (FF) of 0.71 under standard AM 1.5 sunlight at 995 W m^{-2} intensity [75].

However, the high cost of ruthenium-based sensitisers and platinum-based electrodes is still an obstacle to wide-scale commercial exploitation of DSSCs. Accordingly, it is important to develop new affordable dye molecules with high efficiency and long stability as well as non-noble metal-based electrodes. Enlarging the interfacial area of the dye with the electrolyte and accelerating electron transfer in the semiconductor layer to reduce the possibility of charge recombination are also important factors for improving the performance of DSSCs [1].

2.5. Novel P3HT:PCBM Films for Flexible Solar Cells

Conjugated polymer-based organic solar cells have received significant attention due to their potential for low-cost roll-to-roll manufacturing of large-area solar devices on flexible substrates, which open up a vast range of novel applications [76, 77]. Organic photovoltaics are expected to be a low cost, environmentally friendly energy solution with advantageous properties such as flexibility and light weight that enable their use in new applications, and considerable progress in power conversion efficiencies has brought this technology closer to commercialisation [1, 78, 79].

Among the available polymer solar cell systems, poly(3-hexylthiophene) (P3HT) and 1-(3-methoxycarbonyl)-propyl-1-phenyl-(6,6)C61 (PCBM) blends show efficiencies of up to 4–5% [71]. The Donor−Acceptor pair for P3HT and PCBM is shown in Fig. 9.

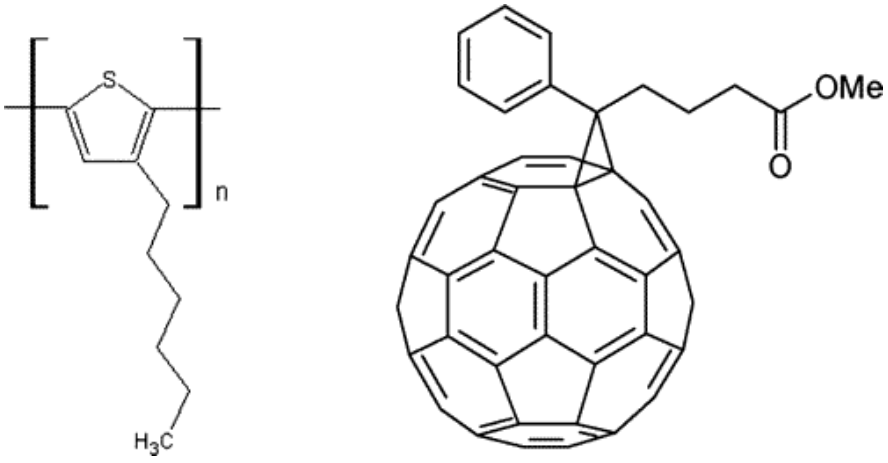

P3HT PCBM

Figure 9. Donor(left)−Acceptor(right) Pair for Polymer Solar Cells Containing Poly(3-hexylthiophene) P3HT (left) and [6,6]-Phenyl C61-Butyric Acid Methyl Ester PCBM (right) [5].

The investigation of the effects of a cell area on the cell performances in ITO-free organic solar cells based on poly(3-hexylthiophene) (P3HT) and 1-(3-methoxycarbonyl)-propyl-1-phenyl-(6,6)C61 (PCBM) was recently reported [52]. Highly conductive poly(3,4-ethylenedioxythiophene):poly(styrene sulfonate) (PEDOT:PSS) films were used as polymeric transparent anodes for cost-effective ITO-free OSCs. Importantly, it was found that with increasing cell area from 4.5 to 49.5 mm^2 [52], the device performance was continuously decreased mainly due to the decrease in the fill factor and the series resistance, suggesting that the sheet resistance of transparent electrodes is a dominant factor to limit cell efficiencies in practical large-area solar cells.

The Poly(phenylene-vinylenes) (PPV's) and P3HT organic polymers are electron rich materials that can be oxidized fairly readily, having high-energy HOMO levels, and are typically hole conducting materials. Organic materials with high electron affinity are much harder to find. Some of the few electron conducting materials are the C_{60} and derivatives alike. C_{60} is in itself a rather insoluble material, but a soluble PCBM derivative is commercially available. The active organic layer in organic solar cells is typically constructed from a mixture of polymer and PCBM that forms an interpenetrating network. PCBM forms crystallites in the active layer and control over size and morphology has significant influence on the efficiency of the device. It has been shown that crystallite size increases on heat treatment of a PCBM/P3HT device improves the efficiency dramatically [80, 81].

The continual developments in efficiency, cost, process, and stability makes polymer-based organic solar cells more attractive as a cost-effective solution to today's energy-shortage problems.

Having justified the need for developing both novel organic materials for photovoltaic applications and corresponding compatible processing technologies, the next Chapter 3 details the Experimental Procedure used in this work.

Although many third world countries struggle to produce enough energy with regard to electricity, many have an abundance of natural energy from the sun. Therefore this project is designed to explore whether operational devices can be made in a non specialised laboratory environment. Thin films were deposited from composite solutions and both were characterised by UV/vis absorption spectroscopy. This films and device structures were characterised by microwave spectroscopy and conductivity measurements. Thermal annealing was used in an attempt to improve the properties of the active layer. The degradation of the cell under solar exposure was also examined.

It is important to note that in this research thesis a layer of Indium oxide deposited as a thermally evaporated thin film was used as a possible replacement for Indium Tin Oxide (ITO) in the construction of the first layer of a prototype solar cell system and as a transparent electrode. The details of the deposition parameters are given in the Experimental Procedure section.

Chapter 3: Experimental Procedure

The following outlines the experimental methodology and techniques employed to build and test the prototype solar cell and study the active layer (P3HT:PCBM). The Q-sun solar simulator is introduced in this chapter. This is used for accelerated age testing via simulated solar sunlight (which will be demonstrated in chapter 4 Results, using 3 different techniques Optical, Electrical and Microwave spectroscopy). The UV-Vis spectrometer is also introduced and is used throughout this project to measure the optical characteristics via absorbance. Also the spin coating technique is used for depositing the thin film layers, active and buffer layers for studying the optical properties and building the prototype device. The screen printing technique is also described; this is used for developing the interdigitated electrode (IDE) sensor for studying the electrical properties of the active layer.

The development of the IDE sensor for the electrical measurements is discussed. Sample preparation of the glass substrates for the optical measurements is also discussed. The techniques used to build the prototype solar cell are also laid out in this chapter. Deposition of a transparent electrode using the Edwards Thermal Vacuum Evaporator is carried out and documented in Chapter 3.

The solution of the active layer was first characterised using UV-Vis Spectrometry. P3HT and PCBM (donor and acceptor material) were dissolved in dichlorobenzene and the absorbance of this solution was measured individually and combined at a ratio of 1:1 in glass cuvettes. The typical patterns will be demonstrated in the following chapter.

Thin films of approximately 100 nm ware deposited onto glass and flexible substrates by spin coating. The layer was also characterised using UV-Vis Spectroscopy. The absorbance was measured before and after annealing. UV-Vis spectrometry is also used to study the effects on the layer after solar exposure.

Electrodes were developed for building prototypes and also characterising the layers by measuring resistivity and impedance measurements in the microwave region. The first electrode was manufactured by Thermal vacuum evaporation. This was an attempt to replace the widely used ITO. Indium spheres (ballbearings) were evaporated onto a glass substrate to create the transparent electrode in solar cells. The next electrodes were developed to study the active layer were the interdigitated electrode (IDE).

3.1. Materials and Equipment Used

3.1.1. Q-Sun Xenon test chamber

The Q-Sun Neon arc chamber reproduces the damage caused by full-spectrum sunlight and rain. In a few days or weeks the Q-SUN tester can reproduce the damage that occurs over months or years outdoors. For exposing produced films to simulated solar light of various intensity, spectrum and duration, Q-Sun Xenon test chamber shown in Fig. 10 was used.

Figure 10. Q-Sun Xenon test chamber in FOCAS Research Institute, DIT.

3.1.2. UV-Vis

Optical absorption measurements were taken using Perkin Elmer Lambda 900 UV/VIS/NIR spectrophotometer before and after annealing and also before and after exposure of the samples to excessive simulated sun light to determine the durability of the layers. The measurements were taken using UV-Vis spectrophotometer in FOCAS Research Institute, DIT, as illustrated in Fig. 11. The Perkin Elmer Lambda 900 UV/VIS/NIR spectrometer is a double-beam, double monochromator ratio recording system with pre-aligned tungsten-halogen and deuterium lamps as sources. The wavelength is from 175 to 3300 nm with an accuracy of 0.08 nm in the UV-Visible region and 0.3nm in the NIR region guaranteed. It has a photometric range of +/-6 in absorbance mode.

Figure 11. Perkin Elmer Lambda 900 UV/VIS/NIR spectrophotometer for assessment of the optical properties.

3.2. Organic Materials Films Preparation

3.2.1. Materials Mixture and Curing

P3HT and PCBM materials were purchased from Ossila Chemicals and were mixed at a 1:1 ratio in dichlorobenzene, which resulted in solution with concentration of 20 mg/mL. The solution was mixed at 60 °C overnight.

The buffer layer was manufactured by spin-coating 0.5 ml of PEDOT on a glass substrate previously coated with Indium Oxide, at 5000 rpm for 45 secs to achieve approximately 40 nm thick layer.

The active layer was made of Poly (3-hexylthiophene) (P3HT) and Phenyl-C60 butyric acid methyl ester (PCBM) were mixed in at 1:1 ratio and dichlorobenzene and stirred at 60 °C overnight.

The back electrode from aluminium film was produced by deposition in thermal vacuum evaporation system or by sputtering at a vacuum of 10^{-6} torr with a current across the tungsten boat of ~ 1 A to achieve ~ 100 nm thick film.

3.2.2. Substrates

The glass substrates were cut into 1"x1" pieces, Ultrasonicated in deionised water, acetone and methanol to ensure adequate cleaning, so that there is no possible contaminant that can alter the performance of the resultant film. Substrates were then also UV-ozone treated for 11 mins before deposition of active functional layers.

3.2.3. Spin-coating

Spin-coating was used to deposit the thin film buffer and active layers on the substate, parameters such as spin speed, dwell time, acceleration time were optimised in order to achieve a certain thickness. The spin-coating process consists of four stages: deposition, spin up, spin off and evaporation and is schematically shown in Fig. 12 [82]. A typical process involves depositing a small volume of a fluid material onto the centre of a substrate and then spinning the substrate at high speed. Centripetal acceleration will cause most of the fluid to spread to and off the edge of the substrate, leaving a thin film of material on the surface.

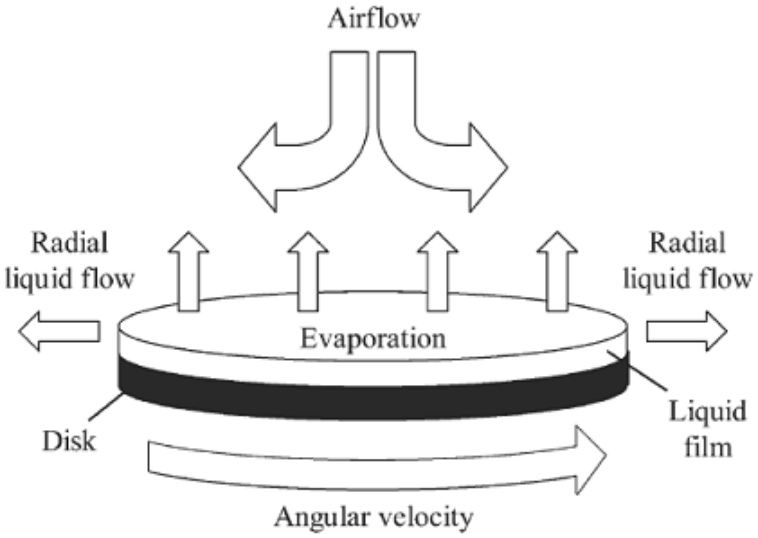

Figure 12. Illustration of the spin coating process [82].

The main advantage of the spin-coating process is that it can produce highly uniform films over a wide range, provided planar substrates are used. Furthermore, the process can be tightly controlled in order to obtain reproducible film thicknesses [83, 84]. Final film thickness and other properties will depend on the nature of the fluid material (viscosity, drying rate, percent solids, surface tension, etc.) and the parameters chosen for the spin process. Factors such as final rotation speed, acceleration, and fume exhaust affect the properties of the coated films. For example, by increasing the angular velocity, the film thickness is reduced.

An increased film thickness can be achieved by repeated spin-coating over previous layers, namely by adding the solution onto the centre of the substrate, while it is rotating at a high speed. A separate drying step is sometimes added after the high speed spin step to further dry the film without substantially thinning it. This can be advantageous for thick films since long drying times may be necessary to increase the physical stability of the film before handling [85, 86].

Interestingly, a two-step method combining electrodepositing and spin-coating for solar cell processing was recently reported [87]. It was used to prepare bilayer heterojunction organic solar cells by electrodepositing polythiophene (PTh) and then spin-coating chloroform solution of [6,6]-phenyl C61-butyric acid methyl ester (PCBM) onto the PTh layer. The influence of film thickness on performance of bilayer solar cells was investigated, and the optimised solar cell showed power conversion efficiency of 0.1% under the illumination of AM 1.5 (100 mW cm^{-2}) simulated solar light [87].

In this work, the G3 P-8 series of spin coater (Specialty Coating System (SCS)) was used for the thin film deposition, as presented in Fig. 13.

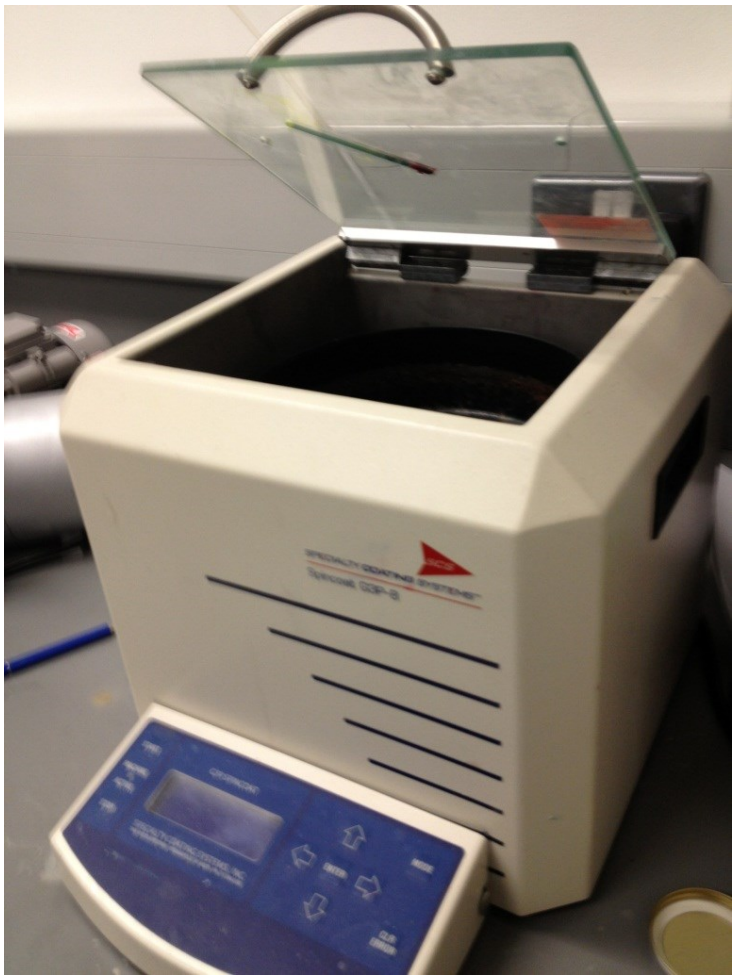

Figure 13. SCS G3p–8 spin-coater.

3.3. Electrodes Design and Manufacture

3.3.1. Electrodes Pattern Design

Structures with interdigitated electrodes (IDE) are commonly used for chemical and physical sensing applications [88-90], particularly for gas sensing [91] in a vast range of industrial and biomedical applications [92-95]; in testing food quality [96], for measurement of fluid mixtures [97], as lumped elements for integrated circuits and as IDE sensors arrays for bacteria detection [98]. Thus, highly selective molecularly imprinted polymers layer combined with IDE were used as sensors to study volatiles, such as pinene, 7-terpinene and terpinolene, as these are the chemical markers that indicate different stages of fruit maturity [96]. Interestingly, the Irish colleagues have recently reported on the development of a sensor fabricated by the inkjet-printed deposition of polyaniline nanoparticles onto a screen-printed silver interdigitated electrode, which was designed for the detection of ammonia in simulated human breath samples [95].

IDE layout is among the most commonly used periodic electrode structures due to the ease of fabrication, flexibility in design, cost effectiveness, no moving parts, fewer packaging constraints [99, 100] and one-sided access to the sensing layer [86], which is particularly important for studying the properties of materials for solar cells. The IDE electrodes structure employed in this work is shown in Fig. 14 (a), where W is finger width, G is the electrode gap and L is the length of the finger, whereas Fig. 14 (b) specifies the dimensions of a single electrodes pattern in mm.

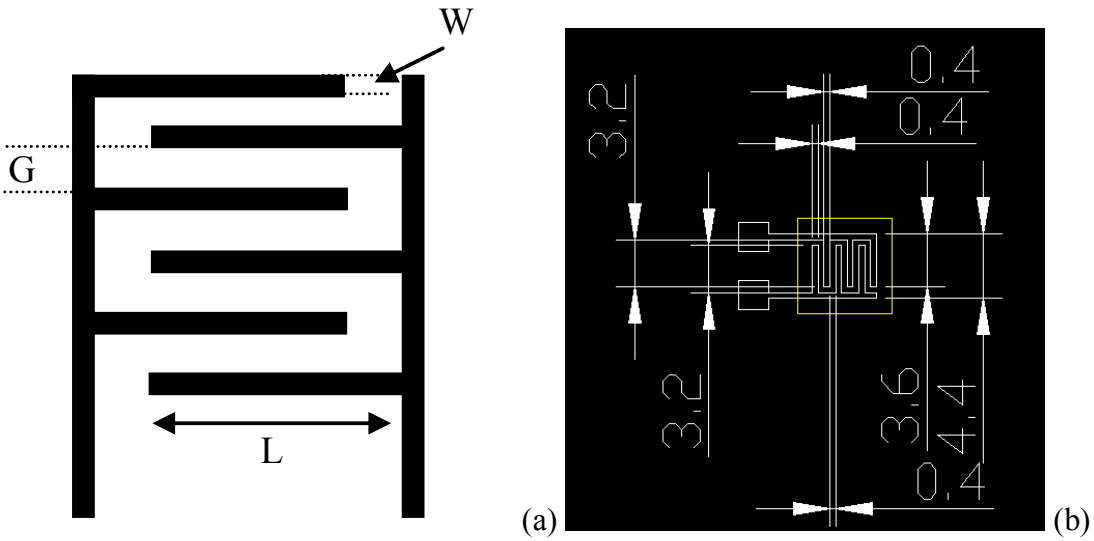

Figure 14. a) Layout of an interdigitated electrodes pair; b) Dimensions of a single electrodes pair pattern in mm.

Specifically for this work, a pair of the interdigitated electrodes with the dimensions as described above was used and a number of devices were printed and tested to ensure the repeatability and reproducibility of the results. The photo of the actual typical bare thick film silver electrodes pair printed on Alumina substrate used for the electrical measurements of the films properties is illustrated in Fig. 15.

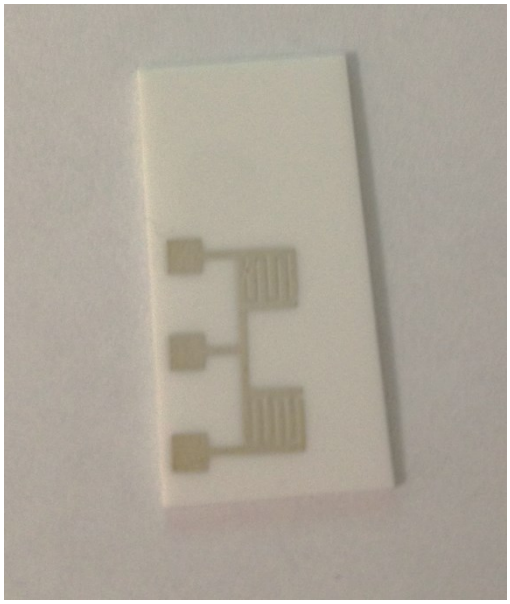

Figure 15. Photo of the bare thick film silver electrodes pair printed on Alumina substrate used for the electrical measurements of the films properties.

3.3.2. Screen-Printing Technique

The fabrication of thick film structures for sensors and semiconductor devices can be achieved using a number of approaches with screen-printing being the most popular. This is due to the fact that this technique is cost-effective, robust and versatile, giving the opportunity to produce complex structures with a range of materials, from metals to polymers, printed on virtually any substrate. In this work, the screen-printing technique was used for the manufacture of silver electrodes for the electrical characterisation of the polymer films, to reveal whether there are any measurable changes in the resistance of the structures cause by the influence of artificial solar light.

Thick-film technology remains popular manufacturing method for many years and its main application is in the production of hybrid microelectronic circuits for use in telephones, automotive electronics, missile guidance systems, and recently for various sensors, including gas sensors, pressure, humidity, radiation and for biomedical

applications [21, 85, 86, 101-105]. The main attraction of thick-film technology is its versatility, high productivity, reliability and reproducibility, and cost-effectiveness even at small or medium scale production. For highly specialised application, thick film technology offers the manufacture of devices that are robust, can be miniaturised, can be integrated onto the same substrate as the electronics [86] and the printed pattern can act as an active component. The films produced using this technology typically measure 10 – 200 μm, and can be deposited on virtually any suitably prepared substrate by a number of approaches, including doctor blading [106], screen printing [86], spin coating [106, 107], dip coating [108] and thermal spraying .

The major steps in the production of thick-film silver electrodes via screen-printing are outlined below, as this is the approach that was taken in this thesis, where printed metal patterns were used as electrodes for electrical characterisation of composite films deposited over them.

The three key processes involved in film fabrication are printing, drying and firing. Screen-printing machines consist of five basic components [86]:

- a system that moves the substrate into the correct position;
- a vacuum, applied to the underside of the substrate to hold it in position during the printing process;
- a screen mounting;
- an alignment system for adjusting the screen relative to the substrate;
- and a system for applying ink and moving a squeegee across a substrate.

Modern screen-printing technological process normally automatically forces an ink or paste through a stainless steel mesh, using a squeegee onto the substrate below it, as schematically shown in Fig. 16 [86].

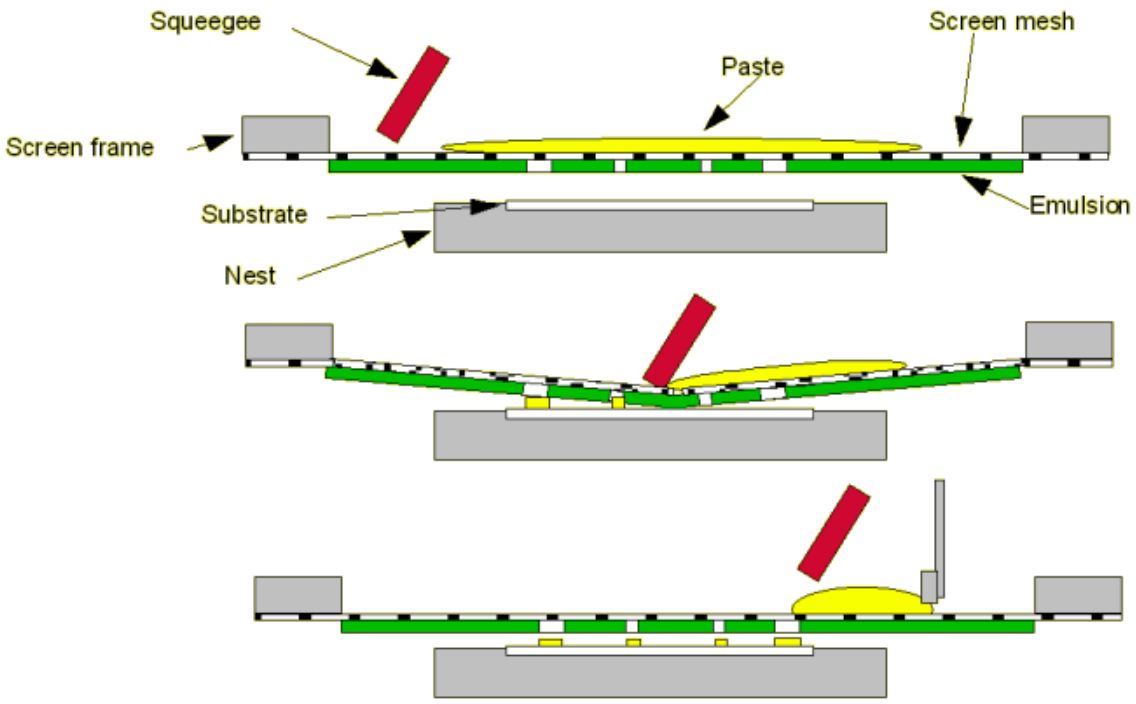

Figure 16. The screen printing process [86].

The substrate acts as a physical support for the thick film and the base for electrical interconnect patterns, which in this work were integrated, i.e. the electrodes were screen-printed over the properly cleaned 96 % alumina with 4 % glass substrates. Importantly, the choice of the substrate, in addition to its basic function of structural support, was dictated by the following considerations: mechanical strength, smoothness of surface texture to promote good film adhesion, chemical and physical compatibility with the fired thick film, high electrical insulation resistance to prevent electrical leakage currents between closely spaced conductor lines, low thermal expansion coefficient to prevent thermal mismatch, high thermal stability to prevent decomposition during processing and not least the desire of cost-effectiveness.

The quality of the printed layer is largely affected by the choice of mask [109-111]. Elements such as the material used, the type of coating, the accuracy of the pattern, the alignment of the pattern to the mesh, the frame type and method of mounting and

supporting the frame for printing are important. Polyester mesh was used in this work and the semi-automatic screen printer model was DEK 1022, as shown in the photo in Fig. 17.

Figure 17. DEK 1022 semi-automatic screen printer.

Three different approaches are used in order to form the stencil of the image to be printed onto the substrate; plastic sheets, metal masks and photo-emulsions. The latter is most popular for thick-film applications and generally uses a water-soluble polymer, which becomes insoluble when exposed to UV light [112].

There are three types of thick film pastes, which are used to form conductors, resistors or dielectrics [86]. The paste can be cermet or polymer in nature, but the main requirement is that it must be able to flow through the screen and retain its intended shape on the substrate beneath. This depends largely on the pastes flow properties, viscosity and particles size in particular. Cermet pastes have a functional ingredient, solvent, temporary binder and permanent binder and require firing at high temperatures.

For polymer pastes, there is no temporary binder and pastes are dried at temperatures in the region of 120 ^{o}C – 250 ^{o}C.

The properties of the squeegee can have a large influence on the quality of the printed layers. The main purpose of the squeegee is to bring the screen into contact with the substrate, push the paste through the stencil to the substrate, to shear the paste level with the top of the screen in order to obtain uniform thickness and to control the rate at which the screen peels away from the substrate.

One of the most commonly used squeegees is the flat or 'trailing edge' type. Its flat edge is preferable for classic screen printing as it is flexible and exerts uniform pressure on the screen. This classic squeegee type was used throughout this work to print the thick film electrodes.

After the screen-printing, the substrates were left to stand in air for 5 minutes to allow the silver paste to settle. To remove the organic solvents from the printed layer, so that it can take its final form and be immune to smudging, the substrates with printed silver electrodes were then placed in a conventional oven at temperature of 100 ^{o}C for 1 hour. Drying also improves adhesions of the printed layers to the substrate.

The term "firing" refers to a high temperature cycle, the purpose of which is to remove the temporary or organic binder from the film, sinter the permanent or inorganic binder, and to develop the electrical properties of the paste, while ensuring the film's adequate adherence to the substrate. To achieve these aims, temperatures of up to 1000 ^{o}C are commonly used and the firing stage is performed in a moving belt furnace. Throughput speed, peak firing temperature and the total firing time are variable parameters which affect the final properties of the film. However, for this work low-temperature silver

paste was used and the firing step was not necessary. This fact reduces the cost of manufacturing without compromising the quality of the final device.

3.4. Testing the Optical Properties of the Films

3.4.1. Samples Preparation on Glass Slides

To reveal the effect of the simulated solar irradiation on the optical properties of organic composite films and to trace the pattern of the changes, the films were deposited on transparent glass slides and the optical spectra were measured before and after each exposure to solar light. For that, 3 x 1 inch glass slides where first scribed with a manual glass cutting tool and split into three equal 1 $inch^2$ substrates by means of placing uniform pressure on either end at different levels. The slides were initially washed in soapy water followed by ultrasonication in deionised water. The samples were then scrubbed with lint free wipes with acetone, ethanol and methanol respectively.

3.5. Organic Solar Cell Prototype Structure Design and Manufacturing Procedure

The properties of the materials which form the active layers of the organic solar cells are of fundamental importance and in this work the focus is on studying the electrical, optical and dielectric properties of PCBM:P3HT films. However, the performance of the film when incorporated in the complete organic based solar cell structure could be hindered by many parameters, including the design of the system, thickness of the layers, choice of contacts materials and so forth. Therefore, an attempt was made to construct a prototype solar cell device with new design. Notably, these prototype cells were not built inside a nitrogen-containing glove box, but in an open air, which one may

argue could compromise the reliability and the repeatability of the devices. However, these were found acceptable for devices kept at constant environmental conditions and not exposed to extreme temperature variations or other physical or chemical factors. Therefore, this section reports on the manufacture procedure and layout considerations for prototype solar cells, with corresponding results given in Chapter 4, Section 4.5.

3.5.1. Deposition of Transparent Indium Oxide using Thermal Vacuum Evaporation

The Edwards 306A coating system was used in this research work to evaporate Indium spheres in order to achieve transparent conductive electrodes based on Indium Oxide thin films, as a cost-effective alternative to traditional approach [113-115]. Notably, the melting point of Indium is 157 °C and the glass substrate normally can withstand at least 300 °C temperature. Therefore, thermal vacuum evaporation method was chosen as the most suitable approach for the manufacture of novel solar cell prototype.

The vacuum evaporation technique is most suitable for deposition of the materials that are difficult to evaporate in air [116]. The method is clean and allows a better contact between the layer of deposited material and the surface upon which it has been deposited. In addition, because evaporation beams travel in straight lines, very precise patterns may be produced. In general, thermal vacuum deposition produces films with structural defects, such as grain boundaries or lattice imperfections [117, 118]. Other frequently observed defects include dislocation loops, stacking-fault tetrahedral, and small triangular defects; all of these are generally attributed to vacancy collapse [119]. Controlling the deposition conditions such as pressure, deposition rate, substrate temperature and surface nature can alter the intensity of film defects. Typical thermal vacuum deposition system, and one that is available in FOCAS Research Institute of Dublin Institute of Technology, is shown in Fig. 18.

Figure 18. Typical thermal vacuum deposition system. The photo is taken in the laboratory of the FOCAS Institute, Dublin Institute of Technology.

The settings for the evaporation procedure vary depending on the type of the material being deposited and desired film properties, such as thickness and conductivity. The mean free path for air at 298 K is approximately 45 cm and 4500 cm at pressures of 10^{-4} and 10^{-6} torr respectively. Therefore, pressures lower than 10^{-5} torr are necessary to ensure a straight-line path for most of the evaporated species and for substrate-to-source distance of approximately 10 cm to 50 cm in a vacuum chamber [85, 119]. In this work, Edwards E306A vacuum thermal coating system, the schematics of the main components of which are illustrated in Figure 19, was used and it satisfied all the necessary criteria to ensure uniform film deposition. The coating unit is equipped with a 550 watt rotary pump and an E040 diffusion pump capable of achieving a vacuum of $5x10^{-7}$ mbar.

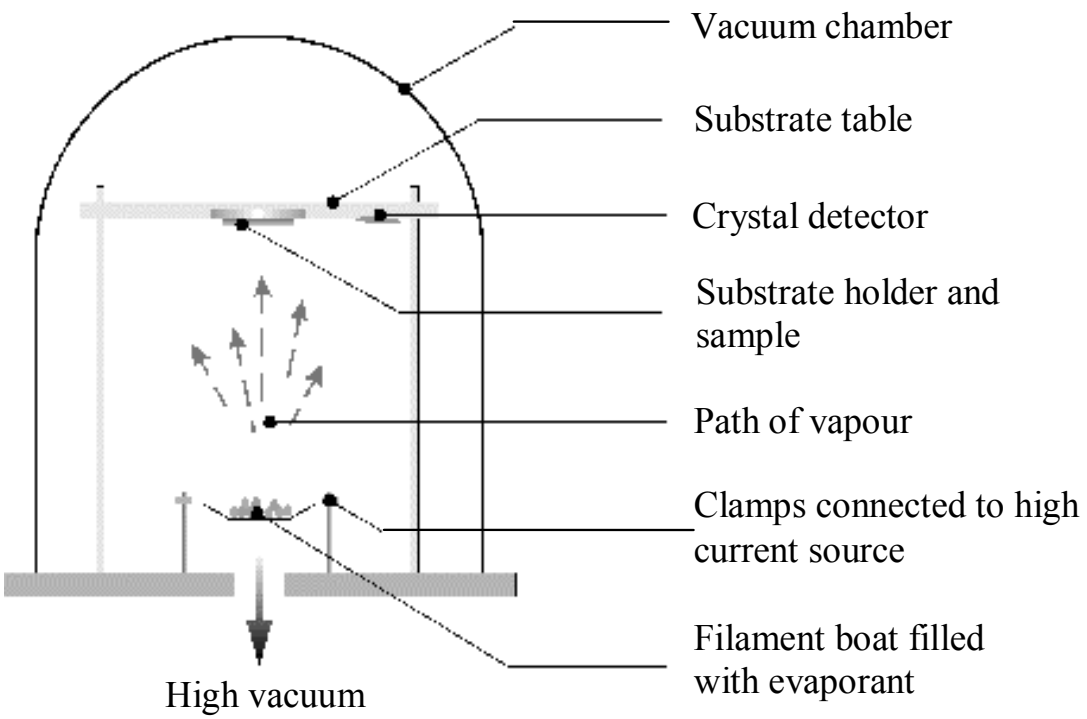

Figure 19. Edwards E306A vacuum thermal coating system.

The substrates with appropriate masks are placed above and at some distance from the material being evaporated. This process leaves a thin, uniform film of the deposited material on all parts of the substrates exposed by the open portions of the mask. Figure 20 pictures a bespoke mask used for evaporating Indium Oxide pattern in Edwards 306E system. This mask was designed and constructed with a view to maximise the electric charge collection by the electrodes as a result of solar irradiation induced changes in the properties of organic film. The resultant pattern achieved after the thermal deposition process is shown in Figure 21. Notably, due to transparent nature of Indium Oxide film, this image shows the pattern deposited with Al material, specifically to illustrate the layout.

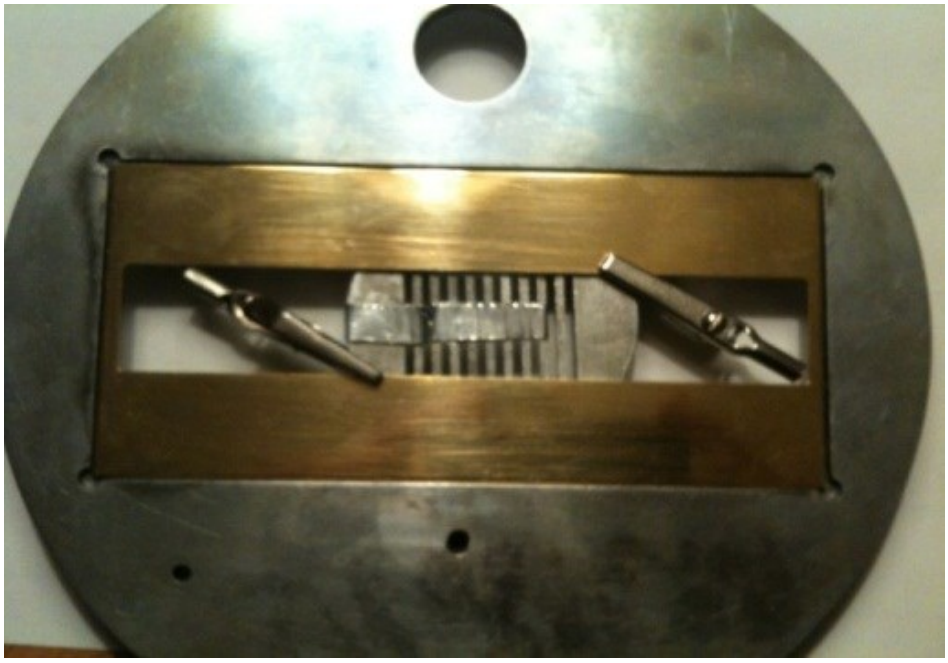

Figure 20. Bespoke mask used for evaporating Indium Oxide pattern in Edwards 306E system.

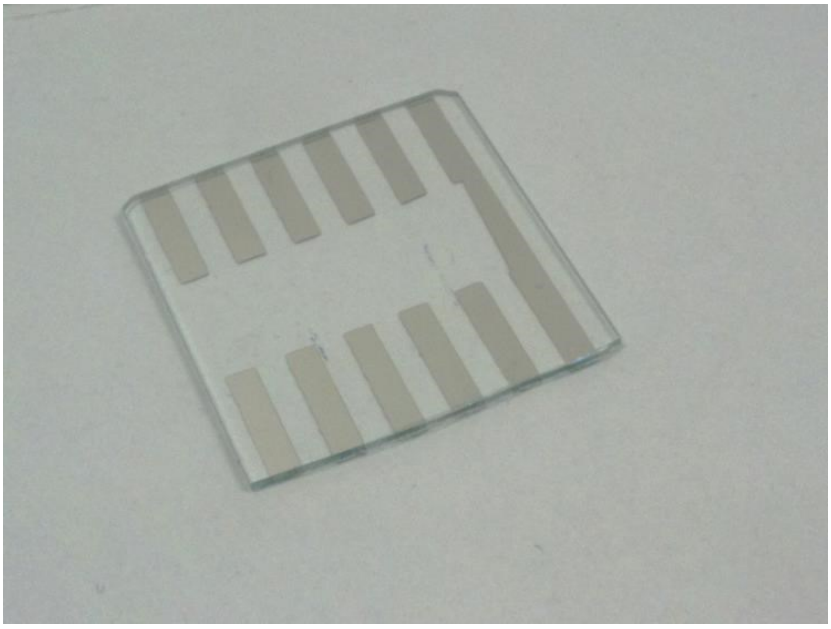

Figure 21. Evaporated Al illustrating the pattern for the transparent layer.

The thermal vacuum deposition system also contains an Edwards FTM5 quartz crystal to monitor the rate of film deposition and to measure the film thickness. The mass deposited on the quartz crystal during the evaporation alters its natural frequency of

vibration. This frequency change can be recorded on the meter of the film thickness monitor connected to the quartz crystal. According to the recommended settings, the following values were used: density 7.3 and acoustic impedance (Z) 10.49.

Approximately 0.05 g of Indium spheres measuring 1 mm in diameter and with 99.99% purity, purchased from Johnson Matthey Ltd, was loaded into a molybdenum boat. The choice of boat material was dictated by the fact, apart from the high melting point, that it does not react with indium and is easy to bend to make custom boats. Prior to deposition, the boats were thoroughly cleaned in Methanol, IPA and deionised water to remove any possible contaminant that can affect the purity of the deposition process.

When the required vacuum level is achieved, in this work it was 10^{-4} mBar to 10^{-3}mBar, the 10-30 A current is passed through the boat with the material in it until the content of the boat begins to melt, which then evaporates and condenses onto the substrate above it. The Penning gauge provided the feedback in order to achieve the required vacuum pressure. Specifically, the best conditions that allowed repeated deposition of this films with reproducible properties, were when the chamber was pumped down to a pressure of $3 \cdot 10^{-4}$ mbar and a maximum current was passed across the molybdenum boat of 30 A. The substrate temperature was controlled using a radiant heater at approximately 300 ^{o}C. Under these conditions the films' deposition rate was 0.028 nm/sec and the resultant achieved thickness of Indium oxide layer was 55 nm.

After deposition, the samples were allowed to cool for 1 hour to reduce the possibility of the cracks and structural defects caused by the rapid change in the temperature, which is particularly vital for solar cells [120-122].

Sheet conductance of the layer was measured using a power supply and a bench top work meter, as shown in Fig. 22. An 8 V input from the power supply returned ~9 mA

output sheet conductance for the 55 nm layer and ~7 mA for the 29 nm layer. Sheet resistivity measurements were performed on a Jandal four point probe, the photo of which is provided in Fig. 23. The resistivity of the film was measured and found to be ~40 Ω/sq for 55 nm layer and ~32Ω/sq for 29 nm layer.

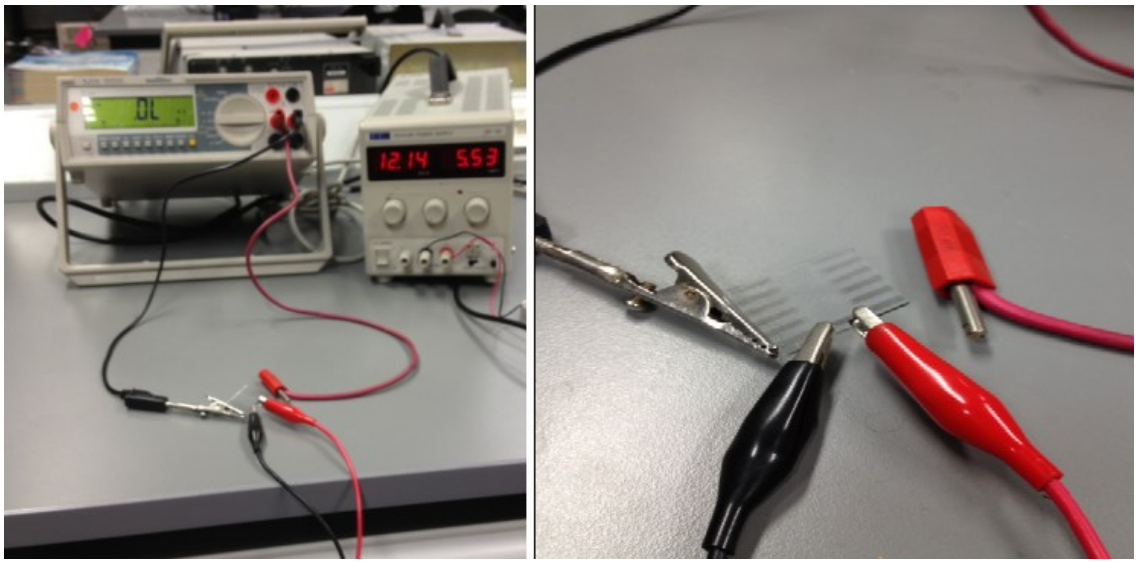

Figure 22. Experimental set-up for measuring sheet conductance of the deposited films.

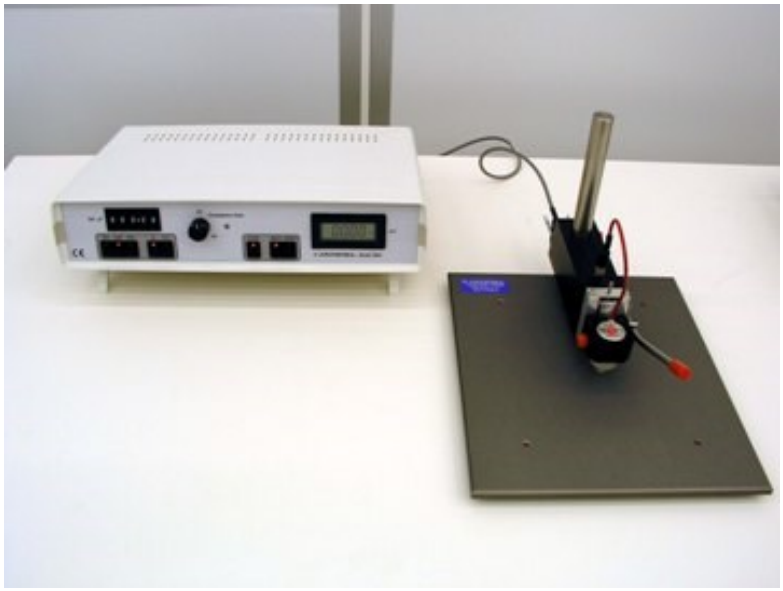

Figure 23. Jandal four point probe.

3.5.2. Bespoke Solar Cell Structure

Two different substrates were used to manufacture the bespoke solar cell, glass and flexible PET with ITO (by Sigma Aldrich) already printed. The bespoke solar cell on glass substrate was manufactured by consequent deposition of the thin film layers using various masks with different patterns and appropriate functional materials, as well as by spin-coating of organic solar light sensitive mixture. Figure 24 illustrates the layout of the novel bespoke OPV device, whereas Figure 25 (a) shows the final manufactured prototype structure, Figure 25 (b) focusing on the electrical contacts.

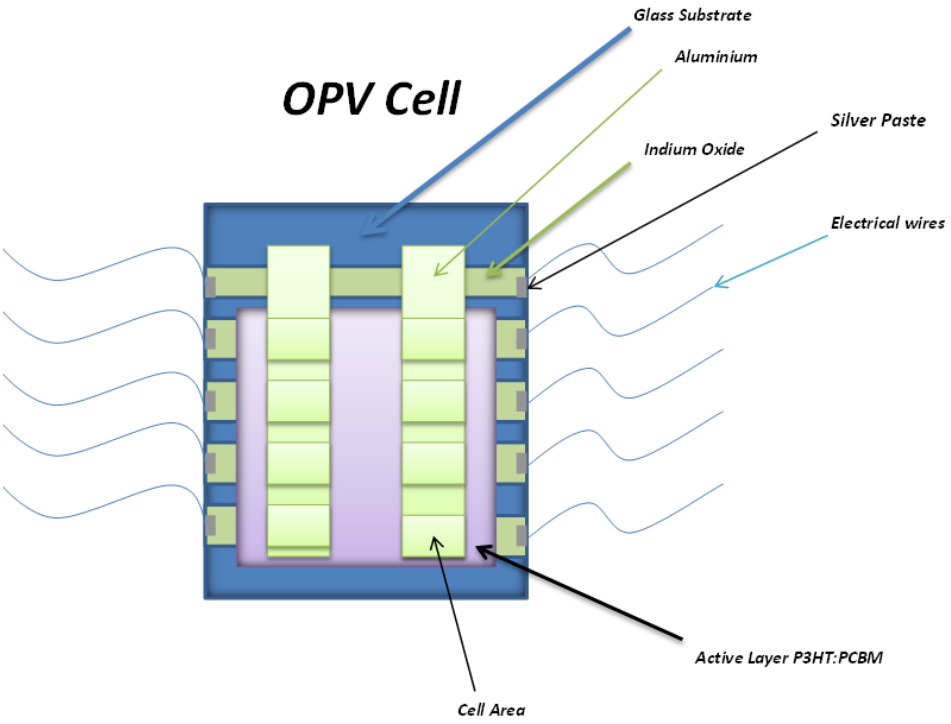

Figure 24. Bespoke OPV Cell Layout.

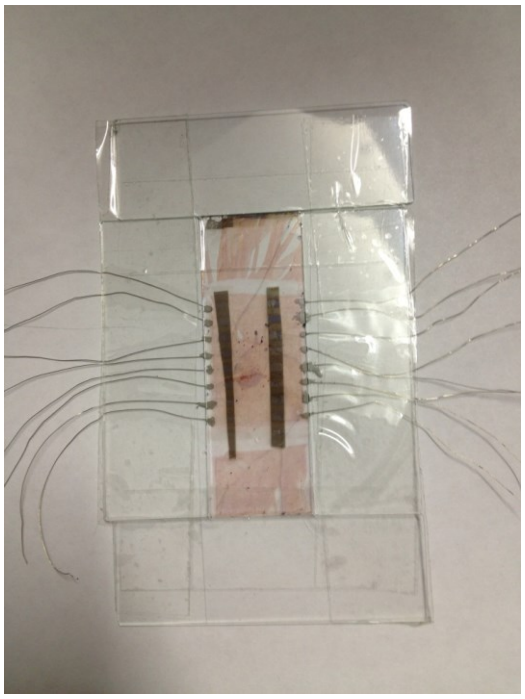
(a)

(b)

Figure 25. (a) final manufactured prototype structure; (b) close-up view of the electrical connections.

Table 2 below summarises each layer material and deposition parameters, as well as final layer thickness.

Table 2. Summary of the solar cell structure and manufacturing process.

Table of Layers	Method	Thickness
Glass Substrate/flexible substrate	Cut and clean DI water, acetone, methanol	
IO(Indium Oxide) on glass/ ITO already on flexible	Thermal evaporate, below 1e-6torr	55nm
PEDOT:PSS	Spin coat, anneal 120°C, 10 mins	0.5ml 5000rpm 45sec ~40nm
P3HT:PCBM (Poly3hexylthiophene:Phenyl C60 Butyric Acid methyl Esther)	Spin coat, anneal 150°C 10mins	0.5ml 1500rpm 45sec ~80-100nm
Al (on glass substrate) Silver paste (on flexible substrate)	Current 1A/s, sputter, 1e-06 torr Hand printed, oven bake, 90°C, 8 mins	100nm ~200um

To clarify, a mask for the deposition of the conductive Indium Oxide (and Aluminium) layers was first custom-made. Then the active material was prepared in the manner described in Section 3.2.1. Briefly, P3HT and PCBM materials purchased from Ossila Chemicals were mixed at a 1:1 ratio in dichlorobenzene, with resultant concentration of 20 mg/mL. The solution was mixed at 60 °C overnight. The glass substrates are cut into 1"x1" pieces, ultrasonicated in deionised water, acetone and methanol to ensure adequate cleaning, so that there is no possible contaminants that can alter the performance of the resultant film. The glass substrates were then also UV-ozone treated for 11 mins before deposition of active functional layers. Afterwards, Indium Oxide was thermally evaporated through the patterned mask in order to coat the substrate with the transparent conductive layer. The next layer is the buffer layer, for which purpose 0.5 ml of PEDOT was deposited on a glass substrate previously coated with Indium Oxide, and it was done by spin coating at 5000 rpm for 45 secs to achieve approximately 40 nm thick layer.

The next layer was the active layer and for that Poly (3-hexylthiophene) (P3HT) and Phenyl-C60 butyric acid methyl ester (PCBM) were mixed in at 1:1 ratio and dichlorobenzene and stirred at 60 °C overnight. And finally, the back electrode from aluminium film was produced by deposition in thermal vacuum evaporation system or by sputtering at a vacuum of 10^{-6} torr with a current across the tungsten boat of ~ 1 A to achieve ~ 100 nm thick film.

Figure 26 illustrates the set-up for testing the electrical properties of manufactured layers.

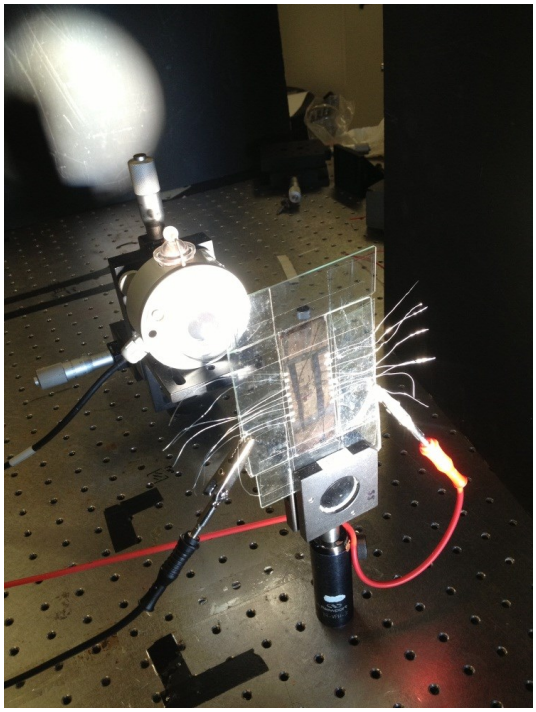

Figure 26. Testing the electrical properties of the glass substrate cell.

For the flexible PET with coated ITO, the procedure for deposition of PEDOT:PSS and P3HT:PCBM is the same as for the glass substrate. Silver paste was chosen as the top electrode, it was hand printed and then baked in an oven at 90°C for 8 minutes.

Chapter 4: Results and Discussion

In this chapter, the results of the films will be discussed with particular attention using the Microwave spectroscopy technique. The theory, equipment, experimental setup and results are all demonstrated. In greater detail, the active layer is examined before and after exposure to the simulated sun. The peaks are observed in the layer as the exposure increases, frequency and amplitude shifts can also be observed.

Optical properties versus Electrical results are also demonstrated. The effects of thermal annealing on the active layer are also demonstrated. The final prototype testing results are carried out discussed in this chapter. In summary, the optical, electrical and microwave characteristics of the active layer along with the final test results for the prototype, have been studied and presented in this chapter also, beginning with a topographical capture using AFM Microscopy.

4.1. Structural Characterisation by AFM

An Atomic Force Microscope (AFM) was used to confirm the thickness levels of the manufactured layers. AFM, a form of Scanning Probe Microscopy, is a high-resolution imaging technique that can resolve features as small as an atomic lattice in the real space. It allows to observe and manipulate at the molecular and atomic level. The atomic resolution of samples is attained in AFM by monitoring small forces applied over a surface using a sharp probe mounted on a flexible cantilever, which acts as a spring [123]. The basic components of an atomic force microscope include a piezoelectric scanner, flexible cantilever containing a sharp probe, laser, photodiode

detector, and feedback electronics. AFM is based on a principle whereby the movements of a flexible cantilever containing an atomically sharp probe are monitored by changes in laser deflection off a reflective surface on the backside of the cantilever.

The Asylum MFP-3D BIO AFM available in FOCAS, as shown in Figure 27, is a high-performance AFM designed specifically for biological applications, and it was used to capture the topographic image of the spin coated layer. It is a versatile AFM that combines molecular resolution imaging and pico Newton force-based measurements on an inverted optical microscope. Combined with its ultra-low noise performance and unprecedented precision and accuracy, the MFP-3D-BIO has already raised the bar for AFM instrumentation in bioscience and now its capabilities are used to test the properties of the materials for the next-generation flexible solar cells.

Figure 27. MFP-3D-BIO AFM in FOCAS Research Institute, DIT.

In this work, the Asylum MFP-3D BIO AFM was used to capture the topographic image of the spin coated layer, as shown in Figure 28. According to the measurements, the topographical profile has the approximate thickness of the layer as 80 nm (edge) and 170 nm (scratch in the centre).

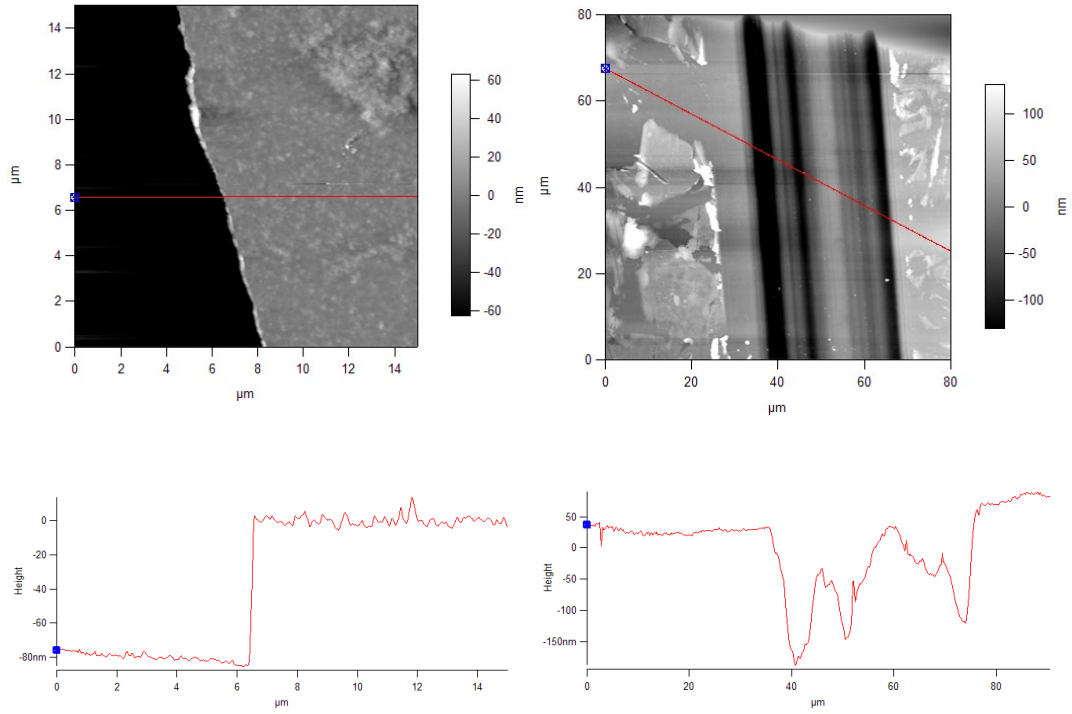

Figure 28. AFM topographic image of the spin coated layer. (left) edge of a spin coated film (right) a scratch in the spin coated film.

4.2. Microwave Spectroscopy of P3HT:PCBM films

4.2.1. Brief review of microwave spectroscopy

4.2.1.1. Electromagnetic waves

An Electromagnetic (EM) wave, also known as Transverse Electromagnetic (TEM) wave, travels through vacuum in form of energy at the speed of light [124]. Its two main components (i.e. electric (E) and magnetic (H) field) oscillate in phase perpendicular (Transverse) to each other and perpendicular to the direction of travel (propagation). EM waves travel in a harmonic wave pattern which occur at equal intervals in time (cycle). The wavelength λ of the EM waves can be described as the distance from any point on one cycle to the same position on the next cycle or wave EM wave with a wavelength λ has a frequency f that travels in vacuum or air (relative permittivity = 1) at the speed of light c according to Eq. 8.

$$\lambda = \frac{c}{f} \qquad \textit{Eq. 8}$$

The permittivity of a material derives from its chemical state and structure; molecular composition and formation; and atomic valance. The permittivity is a measure of various polarisation phenomena that occur at different frequency ranges of oscillating electric fields. Dipolar polarisation is induced in molecules with an inherent dipole moment (orientation polarisation) [125]. An external electric field causes such molecules to rotate over a time period proportional to dipole moment and local viscosity. Dipole moment describes the separation of positive and negative charges on a molecule yielding the overall polarity.

When electromagnetic waves propagate in a medium with relative permittivity (ε_r) or relative permeability (μ_r) more than 1, Eq. 9 is modified to the following form :

$$\lambda = \frac{c}{\sqrt{\varepsilon_r \mu_r} f} \qquad \textit{Eq. 9}$$

EM waves can be classified depending on their wavelengths or frequencies, as for example is shown in Table 3.

Table 3. Electromagnetic spectrum bands wavelengths, frequencies and energy

Region	Wavelength (cm)	Frequency (Hz)	Energy (eV)
Radio	>10	$<3 \times 10^{9}$	$<10^{-5}$
Microwave	10 – 0.01	$3x10^{9} – 3x10^{12}$	$10^{-5} – 0.01$
Infrared	$0.01 – 7x10^{-5}$	$3x10^{12} – 4.3x10^{14}$	0.01 – 2
Visible	$7x10^{-5} – 4x10^{-5}$	$4.3x10^{14} – 7.5x10^{14}$	2 – 3
Ultraviolet	$4x10^{-5} – 10^{-7}$	$7.5x10^{14} – 3x10^{17}$	$3 – 10^{3}$
X-Rays	$10^{-7} – 10^{-9}$	$3x10^{17} – 3x10^{19}$	$10^{3} – 10^{5}$
Gamma rays	$<10^{-9}$	$>3x10^{19}$	$>10^{5}$

The microwave frequency band is part of the electromagnetic wave spectrum, which is referred to as "…alternating current signals with frequencies between 300 MHz and 300 GHz, with corresponding electrical wavelength between 1 m and 1 mm, respectively" [126]. At microwave frequencies, standard circuit theory cannot be used

because of the high frequency and short wavelength [127]. The short wavelengths involved mean that the propagation time for electrical effects from one point in a circuit to another is comparable with the period of the oscillating currents and charges in the system. As a result, conventional low-frequency circuit analysis based on Kirchhoff's laws and voltage-current concepts no longer suffices for an adequate description of the electrical phenomena taking place.

Dielectric spectroscopy characterises the dielectric properties of a material under test with an oscillating source as a function of frequency. It is based upon the interaction of an externally applied oscillating electric field with the electric dipole relaxation moment of the tested material expressed in terms of real and imaginary permittivity. A wide variety of techniques have been developed that are based upon measuring the capacitance and conductance of the materials as a function of frequency. The resulting dielectric spectra are interpreted to analyse and differentiate different substances. The technique uses only a small amount of power in the microwave region (~ 1 mW) and therefore it is non-destructive and non-ionising.

4.2.1.2. Applications of electromagnetic wave sensing in GHz frequency range

Electromagnetic wave sensing in the GHz frequency range, or microwave sensing, is a novel but rapidly developing technology which has been successfully used as a sensing method for various industrial applications including monitoring the water quality [128-130], solution concentrations [131-133], fluid level measurements [134], material moisture content [135, 136], for continuous process monitoring of biogas plants [137], for the determination of moisture content in soil [138], for military applications such as verification of an activated carbon residual life [139] and in the healthcare industry, for

example for real-time monitoring of glucose in diabetic patients [140, 141] and for non-invasive monitoring of bodily fluids [142].

Microwaves are largely used for material characterisation since they easily propagate through low-loss dielectrics and the amplitude of the electromagnetic wave reflected by or transmitted through a material obstacle strongly depends on the dielectric properties of the material itself [143]. Distortion of the signal when in contact with the media, such as polymer film in this work, appears in the form of broadening or compression of the pulse and reaches its maximum at the vicinity of resonant absorption lines [144].

Microwave sensors in the form of a cavity resonator for accurate measurements of both organic (sugar, alcohol) and inorganic (NaCl, $KMnO_4$) water solution concentrations have been reported [131]. Notably, the sensitivity of the sensor in determination of NaCl was 0.4 dB/(mg/ml) within 0-1 % concentration range. The sensor was able to detect the concentrations of other water solutions, but its sensitivities are strongly dependent on the type of tested chemical ingredient.

Notably, the use of microwave irradiation was reported for synthesis of polymer photovoltaic cells [145]. However, no records have been found to date that claim the use of electromagnetic waves in microwave the region for actual organic material properties characterisation for PV applications. It is strongly believed that the proposed approach is novel and has a potential for routine applications along with the electrical and optical studies to provide for better understanding of the complex phenomena that solar irradiation causes in the properties of organic materials.

Many different microwave or radio frequency structures, such as coaxial probes, closed or open resonators, antennas and transmission lines, have been employed to assess the

dielectric properties of material, specifically to measure the permittivity [146]. These are briefly described in the next section.

4.2.1.3. Transmission Lines

Transmission lines are used to transfer high frequency EM waves (radio waves and microwaves) from the source to the destination. The wave that emerges from the source is called the incident wave. When it propagates through the transmission line, it will face some impedance which can be determined from the line physical characteristics (i.e characteristics impedance Z_0). Some of the fundamental types of transmission lines are:

- Waveguide
- Resonant Cavity
- Coaxial cable
- Microstrip.

Rectangular and circular waveguides can be constructed from conductive materials such as aluminium or copper. These types of transmission lines can work efficiently at high frequency due to low attenuation and losses. Another variation of waveguides is called waveguide coplanar [147]. The drawbacks for these waveguides include them being heavy and inflexible to bend. When an EM wave propagates within the waveguide, it forms different E and M field configurations; these configurations are called “modes” and are depending on the shape and size of the waveguide. Two main types of these modes can be exist, transverse electric (TE) and transverse magnetic (TM) modes. The difference between the two types is defined by the component of the wave which is transverse to the direction of the signal propagation from one end to another where TE modes only have a magnetic field component and no electric field component in the

direction of propagation and TM modes only have an electric field component with no magnetic field component in the direction of propagation.

Microwave resonators [148] can be constructed from closed sections of rectangular or circular waveguides. When both ends of the waveguide are shortened, a cavity is formed. According to Bansal [149], cavities use the constructive and destructive interferences of multiply reflected waves to cause resonance – for that reason, cavities are also called resonators. In resonance, the system tends to oscillate at greater amplitude at some frequencies known as resonance frequencies. Each resonance frequency has its own "mode". Depending on the shape and size of the cavity, different mode is generated.

To elaborate further, at certain excitation frequencies, standing waves will form within a cavity, and in microwave engineering these are referred to as modes, and can be illustrated in terms of the direction and/or intensity of the microwave electric or magnetic field components. Pozar [150] defines Eq. 10 as a method for determining the frequency at which such modes will occur:

$$f_{nml} = \frac{c}{2\pi\sqrt{\mu_r \varepsilon_r}} \left[\left(\frac{p_{nm}}{a} \right)^2 + \left(\frac{l\pi}{d} \right)^2 \right]^{1/2} \qquad \textit{Eq. 10}$$

where c is the speed of light, p_{nm} is the m^{th} root of the Bessel function of the n^{th} order for TM (transverse magnetic) modes or the m^{th} root of the first derivative of the Bessel function of the n^{th} order for TE (transverse electric) modes, a is the radius of the cavity, d is the depth of the cavity and l is its length.

Each mode will generate a resonant peak. Since, according to Eq. 10, all electromagnetic modes have the same dependence upon $\sqrt{\varepsilon_r}$, when the cavity is excited by an appropriate range of frequencies and the resulting spectrum is captured, the resonant peaks corresponding to these modes will shift to lower frequencies as ε_r is increased. Therefore, if exposure to sun light causes a change in dielectric properties exhibited by the material, one would expect to see the resonant peaks measured in the reflected or transmitted spectrum also shift.

When designing a microwave cavity, several parameters have to be considered, including construction material, energy coupling mechanisms, resonance frequency and quality factor, as well as scattering parameters. Metals with high electrical conductivity are usually used to confine the EM waves within the cavity so minimum or zero electric power loss is achieved. There are two methods for coupling the EM waves to the cavity, magnetic flux linkage or electrical field antenna coupling [127]. The first method however is normally used for high power applications where a lower loss transmission line (i.e. cylindrical or rectangular waveguides) is required to avoid energy losses [151].

The cavity can be coupled using either a monopole antenna where the centre conductor of a coaxial cable is extended into the cavity or by using a loop antenna in which the surface area of the loop is placed perpendicular to the magnetic field (H) lines on the inner surface of the cavity as illustrated in Figure 29 [152].

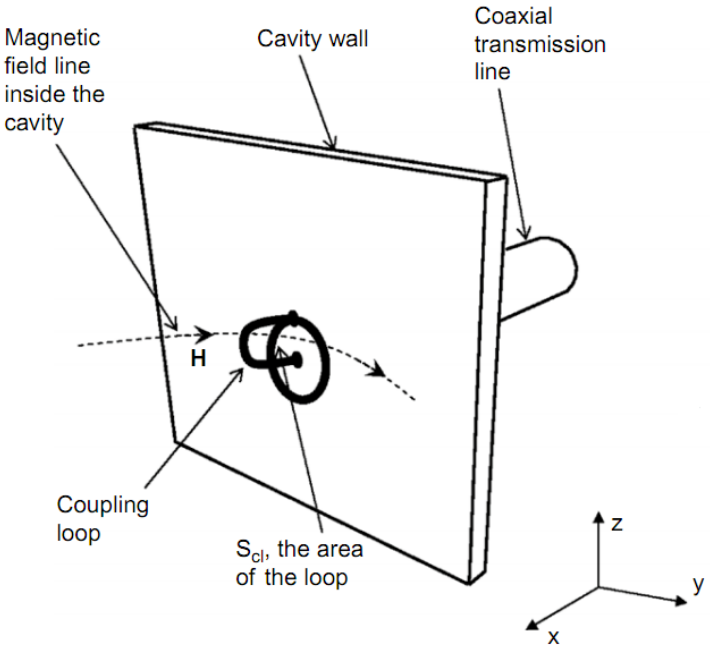

Figure 29. Loop antenna coupling method [152].

The main difference between the two antennas is the mode of interest to be excited in which the monopole antenna placed on the wall of the cavity where there is a perpendicular Electric field (Vertical Magnetic field). This field's configuration occurs in TE modes while the loop antenna placed on the wall of the cavity where there is a perpendicular Magnetic field (vertical electric field) and this configuration occurs in TM modes.

The quality factor (Q) [153] is the measure of efficiency with which the energy storing element can store maximum energy and is defined as in Eq. 11. The quality factor for ideal cavity resonator is infinite, due to the perfect conductor walls, thus, resulting in zero energy dissipation, but when the cavity is loaded (material or shape perturbation), the quality factor will be decreased (insertion loss) depending on the characteristics of the load. Furthermore, different cavity modes can have different quality factors

depending on the position of the loaded material in the cavity and its interaction with the EM wave.

$$Q = 2\pi \frac{Maximum\ energy\ stored\ in\ one\ cycle}{Energy\ dissipated\ per\ cycle} \qquad Eq.\ 11$$

4.2.1.4. Scattering Parameters

Scattering parameters, or S-parameters, quantify how EM waves behave in a closed N-port resonator [154]. As EM waves are launched from the input port, some of their energy will be received on other ports, some will be reflected back. S-parameters can be expressed using power values, i.e. Magnitude (dB) and angle *f* (Hz). An N-port device has N^2 S-parameters; for example, a two-port device has four S-parameters. The numbering convention for S-parameters is that the first number following the "S" is the port where the signal emerges, and the second number is the port where the signal is applied. For example, a cavity with two ports has four S-parameters as shown in Figure 30:

S_{21} – refers to the signal that is transmitted from port 1 and received on port 2.

S_{12} – refers to the signal that is transmitted from port 2 and received on port 1.

S_{11} – refers to the signal that is transmitted from port 1 and received on port 1 (reflected).

S_{22} – refers to the signal that is transmitted from port 2 and received on port 2 (reflected).

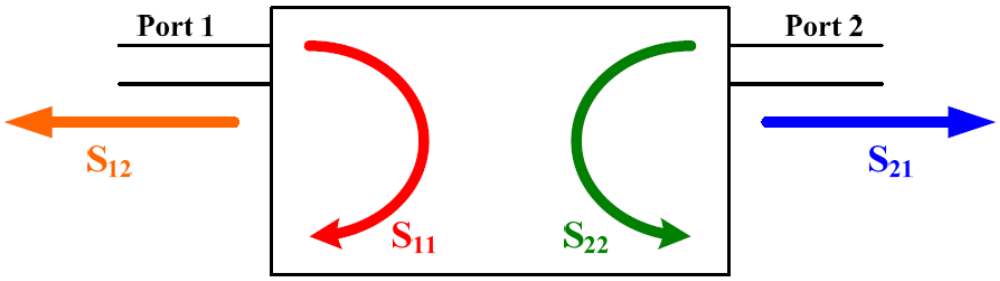

Figure 30. Block diagram of S-parameters for two ports cavity.

The S-parameters, S_{11} and S_{21} are determined by measuring the magnitude and phase of the incident, the reflected and the transmitted voltage signals when the output is terminated in a perfect Z_o (a load that equals the characteristic impedance of the test system) [155].

Notably, microwave resonators can be used in different application such as filters [156, 157], oscillators [158], material sensing [159-162] and tuned amplifiers [163]. The previous applications would use small transmitted power ≤ 10mW, while cavities and waveguides can also be used in high power applications such as material heating [164], plasma generation [165] and microwave-assisted synthesis of organic materials for PV applications [145].

The coaxial cable, as shown in Figure 31, consists of two conductor wires. The outer wire is in a form of a shield around the inner conductor. They are separated by a high permittivity semiconductor layer which minimises the external radiation interference [166]. The most common use for this type of transmission line is the TV cable which carries the signal from the antenna to the TV set. Coaxial cable connectors are designed to maintain the shielding that the coaxial design offers. Many types are available such as

N-Type and Sub-Miniature version A (SMA) Connectors [167], as illustrated in Figure 32.

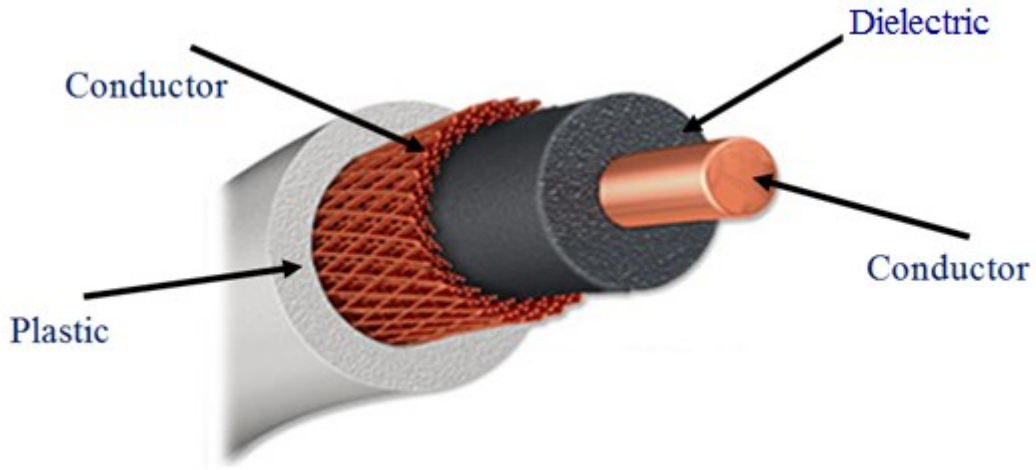

Figure 31. Coaxial cable.

Figure 32. N-Type and SMA coaxial cable connectors.

The microstrip [168] is the most popular type of planner transmission line (Figure 33) [169], it can be fabricated using the Printed Circuit Board (PCB) method where a thin conductor is printed to act as the inner wire of the coaxial cable but flattened, the ground plane will do the same job as the outer shield of the coaxial cable. This configuration is useful when other RF components are needed to be connected to

transmission line as shown in Figure 34 [170]. The drawback for it is that it suffers from radiation loss.

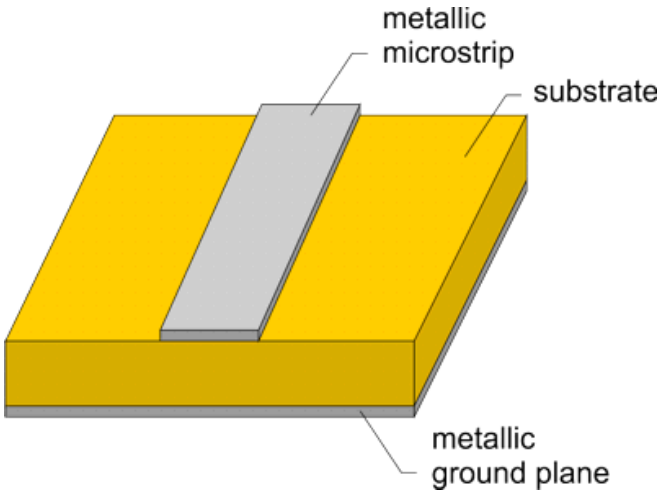

Figure 33. Typical microstrip transmission line [169].

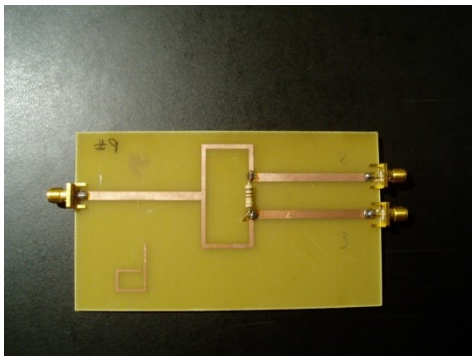

Figure 34. PCB with microstrip transmission line connected to resistor [170].

Notably, among the above-described methods, transmission line is the most studied structure for high frequency measurements, including the characterization of low-k dielectric thin film.

However, the microwave planar printed patterns for various sensing applications are increasingly used due to their versatility, flat profile and low weight. Their design can be tailored to suit particular applications, coupled with reliability and cost-efficiency.

They are easily manufactured using common methods for printed circuit board production, and their impedance can be matched to the input line by altering the micro-strip line feed configuration.

The patch antenna represents the frequency-selective element of a phase shift transistor oscillator. The active integrated antenna frequency of operation is determined by both the patch geometry and the electrical loads connected at the two microstrip ends [171]. A convenient termination is normally represented by two open-ended stubs whose electrical length is $\lambda/4$ at the patch resonant frequency, where λ is a complete wavelength.

For example, a coaxial-fed patch antenna suitable for non-destructive porosity measurements in low-loss dielectric materials has been reported [172]. The variation of the patch resonant frequency when it is put on the surface of the material under test was used to estimate the dielectric permittivity at 2.4 GHz ISM (Industrial Scientific and Medical) frequency bands. The estimated porosity was in good agreement with that obtained by the conventional mechanical measurements, and the mean percent error was less than 13.5%.

The performance of a microstrip resonator depends on its electromagnetic field distribution, resonant frequency and quality factor Q. Since the emergence of microstrip technology as a dominant architecture, varying types of microstrip resonators have been developed to suit the needs of different microwave circuits [135].

To clarify the principle behind testing material properties with electromagnetic waves used in this work, it is worth mentioning that microwave sensors in the form of planar printed patterns operate based upon the fact that an object under test, e.g. a film sensitive to sun light, when placed into the vicinity or in direct contact with a

microwave sensor, interacts with the electromagnetic waves in a unique manner, which can be specifically correlated with the properties of this material. In particular, the sensing is based on interaction of propagating or resonating modes with the solution under test. Due to this interaction, the permittivity of the material changes and it manifests itself as a frequency change, attenuation, reflection of the signal or a phase shift. In the microwave region up to frequencies of about 100 GHz, the complex dielectric spectrum of, for example, water can be well represented by a Debye type relaxation function [173]. A Debye dielectric is the representative linear dispersive medium and is often used to model electromagnetic wave interaction with water based substances including biological material [174]. It should be noted, nevertheless, that water is a complex media which changes its structure depending on the structure of the material in contact with it. This fact was experimentally and theoretically confirmed in [175], where the dielectric properties of water bound to soil were investigated. The current understanding suggests that the closer the water layer is to the particle the more distorted is its structure compared to the structure of free water.

By considering how reflected (S_{11}) microwave signals vary at discrete frequency intervals, the change in the signal can be linked to the composition of the object under test. These signals vary depending upon properties of the material / film presented to the sensing structure, such as conductivity and permittivity [176]. Conductivity is a measure of a material's ability to conduct an electric current. Permittivity is a measure of how an electric field is affected by a dielectric medium, which is determined by the ability of a material to polarise in response to the field, and reduce the total electric field inside the material. Therefore, permittivity (ε_r), as defined in Eq. 12, relates to a material's ability to transmit an electric field and is a complex value which varies with

changing frequency, and accounts for both the energy stored by a material (ε') as well as any losses of energy (ε'') which might occur:

$$\varepsilon_r = \varepsilon' + j\varepsilon'' \qquad \textit{Eq. 12}$$

Notably, ε' and ε'' represent respectively real and imaginary parts of the complex permittivity value (ε_r), which depends on frequency. This frequency dependence is specific for each material and therefore can be used as an indicator of its properties [133]. As a material in close proximity of EM field changes its state or properties, it is likely that its permittivity will change leading to a change in sensor response if the material is the target of EM radiation. By measuring this response over a range of frequencies, one can characterise materials in order to infer their properties.

In order to get maximum sensitivity of the microwave sensor, the material under test must be positioned near to the field maximum. However, other resonant modes could also provide useful information and in some cases, as the research reported in this paper shows, depending on IDE sensor configuration, low-order resonant modes could be more sensitive to the minute variations in dielectric properties of the material under test.

4.2.2. Experimental setup for microwave spectroscopy measurements

The design of any microwave sensor is the key parameter that regulates its performance. Sensors with the IDE structure shown in Figure 35, operating at microwave frequencies were chosen for their versatile design that combines ease of manufacturing with the desired functionality. Silver was used as the conductive metal material for the both bottom layer, which acted as a ground plane, and the IDE pattern on the top layer to maintain chemical neutrality when the device is placed in contact with water. The thickness of the Ag layers was 35 μm and the width of each line on top pattern is 2 mm.

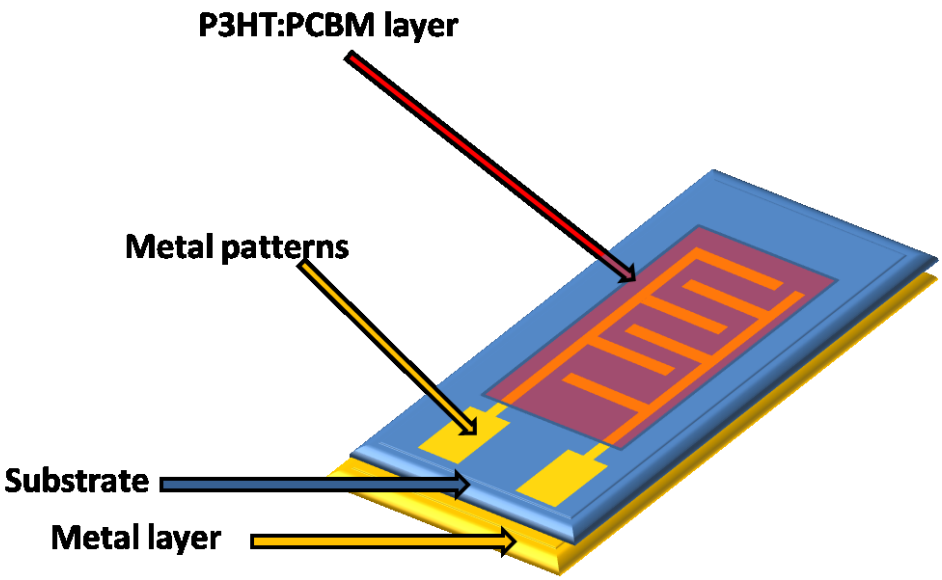

Figure 35. Electromagnetic wave sensor with printed metal pattern and light-sensitive P3HT:PCBM layer.

Figore 36 displays optical images of the manufactured prototype microwave sensor on DuPont™ Pyralux® AP Polyimide Flexible Laminate substrate with 50.8 µm thickness, which is bent to illustrate its flexibility. The thin flexible substrate provides not only structural benefit for a wide range of applications, but also plays a pivotal role in controlling the strength of a microwave signal fed into the sensor. Thicker substrates are prone to the following effect: as the substrate thickness increases, surface waves are introduced which are not usually desirable because this results in a lower electric field density [177]. The surface waves travel within the substrate and they are scattered at bends and surface discontinuities and affect the printed metal pattern and its polarisation characteristics [178].

Figure 36. Optical image of the 3 pair IDE microwave sensor, which is bent to illustrate the flexibility of the polymer substrate [177].

Each sensing method has its limitations, and in the case of the planar type electromagnetic wave sensors, the properties of the materials used for the substrate and as ground and top metal layers play pivotal role, along with the structure of the device itself, in determining the boundaries of sensitivity to the sensing method. Therefore, to ensure that the changes in the dielectric properties of P3HT:PCBM films are only due to their exposure to the simulated sun irradiation, alternative EM sensor was used in parallel, namely, having identical layout to one depicted in Figure 35, but with Rogers® material used as a substrate and Cu metal for both bottom and top antenna patterns. This EM device without SMA is illustrated in Figure 37.

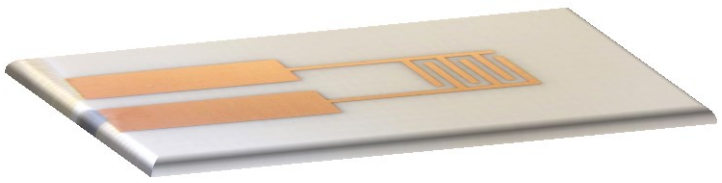

Figure 37. Optical image of a EM wave sensor head constructed on Rogers® substrate and having Cu metal patterns.

A distinct feature of IDE type sensors is their superior sensitivity to change close to the sensor surface, with this sensitivity decaying rapidly with distance away from the surface. Reported simulations of the 3D IDE sensor structure, created using the Ansoft High Frequency Structural Simulator (HFSS) finite element modelling software (see Figure 38), demonstrate this feature [177]. This model, whose performance has been verified against real-world measurements, is constructed such that the sensor is placed inside a suitably sized air box - the outer faces of this box are assigned as radiation boundaries. Adaptive meshing is used for the simulation, with approx. 25,000 tetrahedra being required for a converged solution. Notably, the electric field intensity (shown in V/m) falls rapidly as one moves away from the electrodes. This is advantageous as it reduces significantly the chance of undesirable factors influencing sensor response.

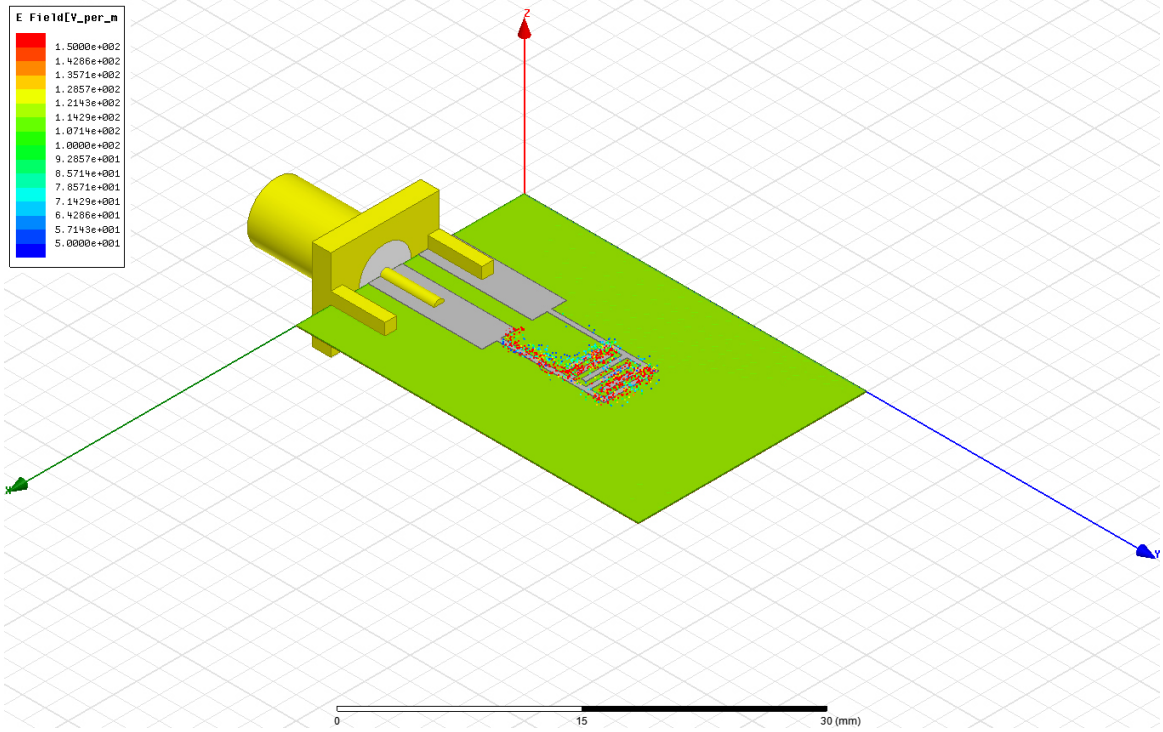

Figure 38. HFSS model of EM wave sensor field [177].

A vector network analyser (VNA) is used to generate high frequency signals and measure the parameters of electrical network, typically the S-parameters. VNAs contain both a source and multiple receivers, and generally display amplitude ratios and phase information (frequency or power sweeps). In this work, the electromagnetic wave sensors with light-sensitive coatings on top of the metal pattern were each attached to a Rohde and Schwarz ZVA24 vector network analyser via a coaxial cable.

SMA type connectors were used as they are very common, popular and readily available for work of this nature. The sensor and associated equipment were all specified for 50 Ω impedance. Thus, depending on the size of the pattern or substrate, the connector dimensions may vary [179]. Molex edge mount connectors were used in this work. This SMA type was chosen as it is designed to excite a printed IDE sensor horizontally to maximise the available signal.

The VNA used for the purposes of data acquisition from the sensors, with this unit being appropriately calibrated according to manufacturer specifications, is shown in Figure 39. The data (60,000 points for each measurement) was captured in the frequency range of 1-15 GHz for the reflected (S_{11}) signals. All the measurements were performed at constant temperature of 18 °C. Each sample was measured for at least 7-9 times and the results were repeatable with less than 5% deviation and reproducible. Notably, average sensor responses are depicted in the graphs shown in following section.

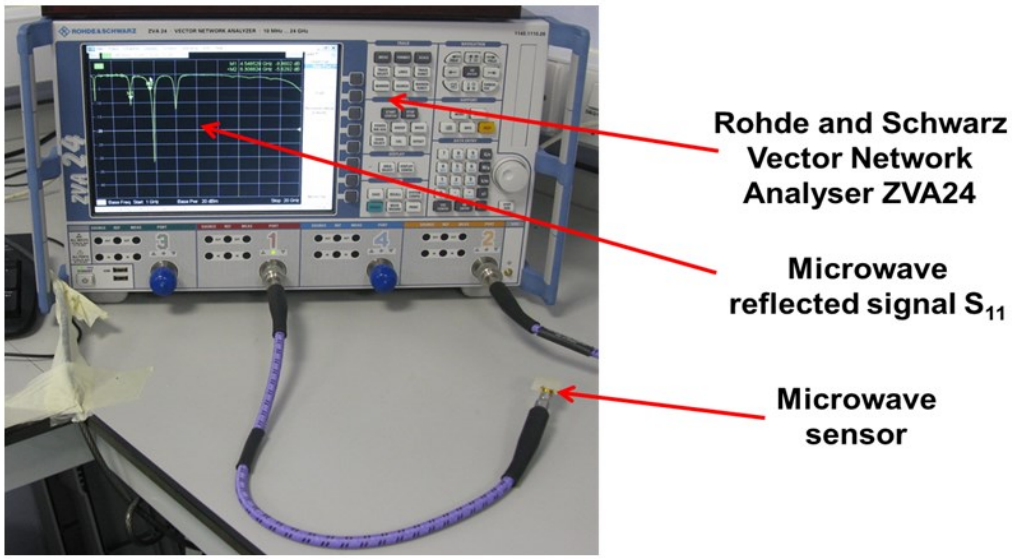

Figure 39. Measurement setup showing VNA and a microwave sensor connected via coaxial cable [177].

4.2.3. Films reproducibility verification by microwave measurements

Throughout the experimental work, all samples, i.e. deposited films, were produced in at least triplicate to ensure that the devices are reproducible, and also each measurement was performed numerous times, the number depending on the nature of measurement, to ensure repeatability of the results. In all the experiments, the environmental conditions were maintained at a constant temperature and humidity level, to eliminate their effect on the properties of the P3HT:PCBM samples.

Despite taking special care to thoroughly follow the experimental procedures when depositing the films and using optical inspection of the devices to confirm the absence of the defects in their structure, it is more reassuring to perform additional non-destructive measurements of the films properties. One such method to confirm the reproducibility of the devices employed in this work is measuring their electromagnetic wave spectra to assess that the dielectric properties are identical, or at least that the

possible variations in their properties are negligible and for laboratory type prototype can be acceptable as negligible. Thus, by recording the EM spectra in 0.01-15 GHz frequency interval for a number of samples and contrasting them with each other, one may reveal the presence of the defects in their structure. For example, Fig. 40 illustrates the typical S_{11} signal distribution of the microwave sensor on Rogers® substrate with Cu pattern in 0.01-15 GHz range when in contact with two P3HT:PCBM films samples.

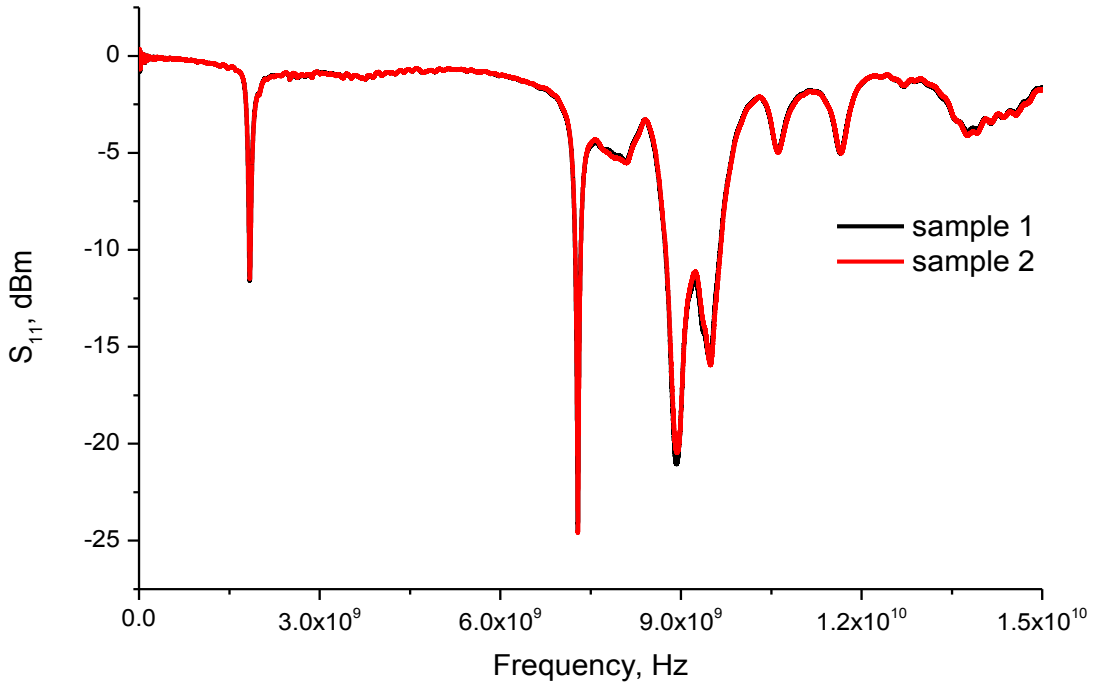

Figure 40. S_{11} signal distribution of the microwave sensor on Rogers substrate with Cu pattern in 0.01-15 GHz range when in contact with two P3HT:PCBM samples.

The measurements revealed that S_{11} signal distribution for the two P3HT:PCBM samples is almost identical throughout the whole measurement range, which confirms the reproducibility of the films. Importantly, each spectrum was recorded with the accuracy of 60,000 points per measurement range, providing superior resolution. The next section examines the effect of the solar irradiation on the microwave spectra of these samples.

4.2.4. Solar Exposure Effects on a microwave sensor with a flexible polymer substrate and Ag pattern

Once the reproducibility of the samples was confirmed, the electromagnetic wave sensors were used to reveal if there are any changes in dielectric properties of the P3HT:PCBM films caused by their exposure to simulated solar light in the Q-Sun Xe-1 Xenon Test Chamber, which was briefly described in Section 3.1.1. Since all other experimental parameters, including temperature and humidity were kept constant during all the measurements, any changes in the films' properties can only be attributed to the effect of the solar irradiation.

For the measurements of the P3HT:PCBM films' dielectric properties, electromagnetic wave spectra were recorded for the films deposited over EM sensors on flexible substrate with Ag antenna patterns. Full EM spectra in 0.01-15 GHz range for bare sensors and for as-deposited, and exposed to sun light for 1 hour and 20 hours P3HT:PCBM films are shown in Figure 41. It is clearly seen that the sensor can distinguish the presence of a thin P3HT:PCBM layer, as the spectra for the film and the air alone are different even to the eye.

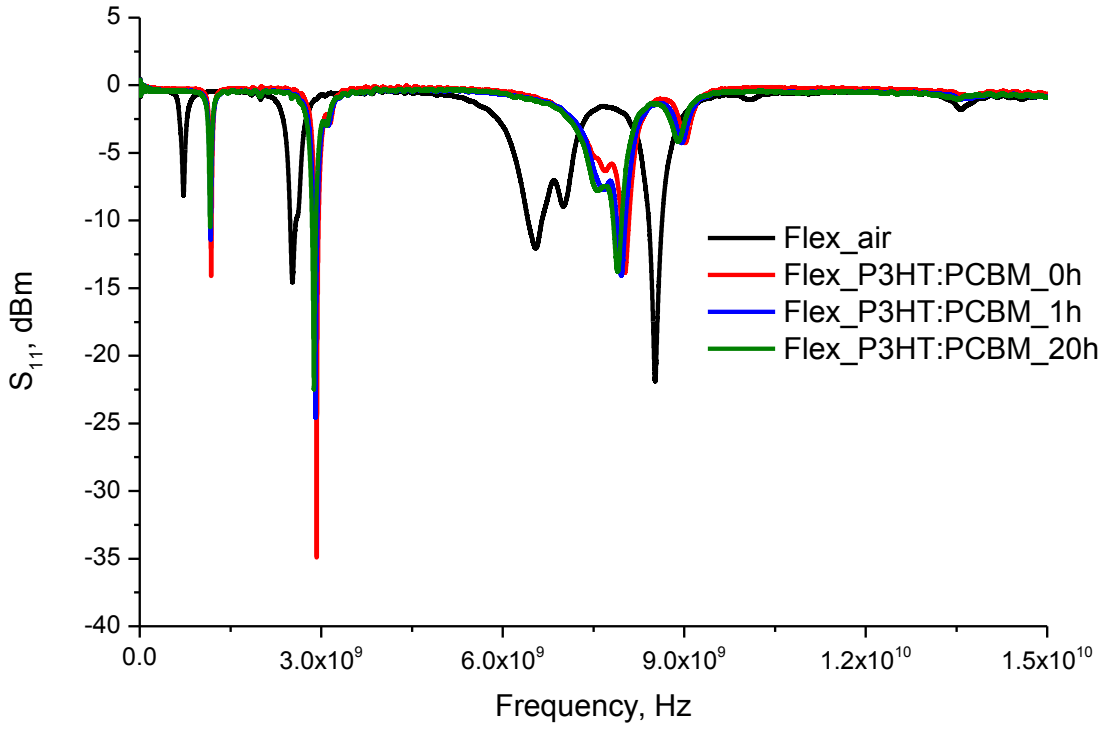

Figure 41. S_{11} signal distribution of the microwave sensor on flexible substrate with Ag pattern in 0.01-15 GHz frequency range when in contact with air and P3HT:PCBM films irradiated for 0, 1 and 20 hours.

However, it is of paramount importance for this research to reveal if there are any changes in the material properties caused by the exposure to the sun light, and for that a closer look at various parts of the microwave spectra were taken, focusing on the resonant peaks where the changes are the most pronounced. Thus, Figure 42 depicts S_{11} signal distribution of the microwave sensor on flexible substrate with Ag pattern in 0.6-1.4 GHz frequency range when in contact with air and P3HT:PCBM films, as-deposited and irradiated for 1 and 20 hours. The first resonant peak occurring just below 1.2 GHz experienced a shift in the resonant frequency towards lower values with the increased duration of the exposure to sun light, while at the same time the module of the amplitude of this peak decreased.

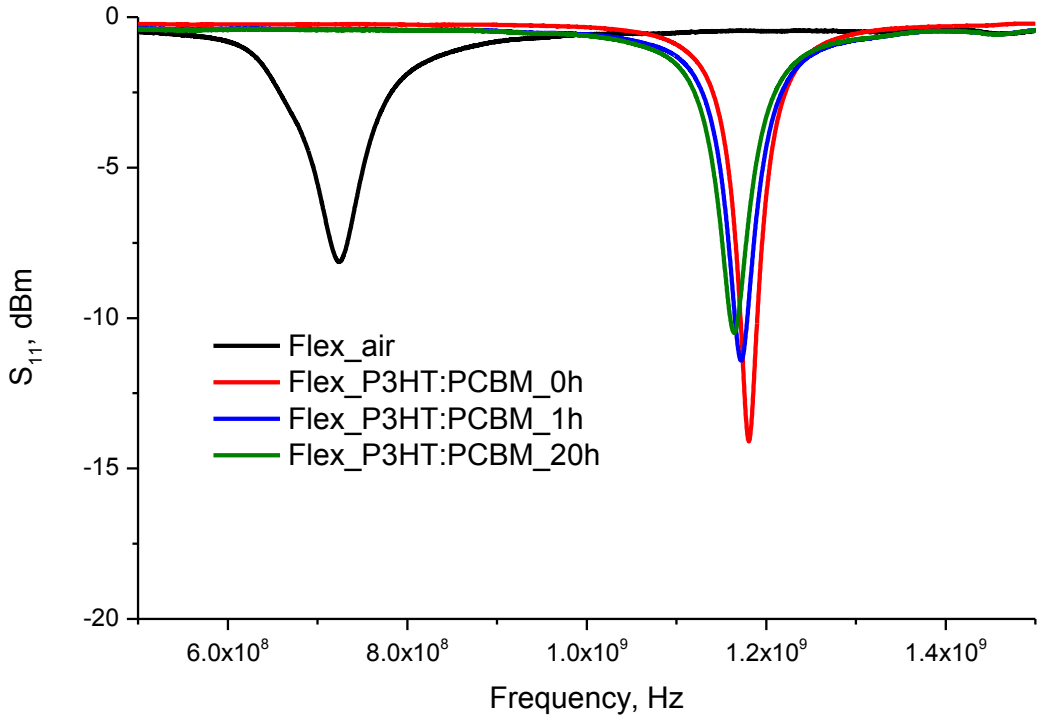

Figure 42. S_{11} signal distribution of the microwave sensor on flexible substrate with Ag pattern in 0.6-1.4 GHz frequency range when in contact with air and P3HT:PCBM films irradiated for 0, 1 and 20 hours.

Similar behaviour can be seen for the second resonant peak, which occurred in the region of 2.8-3.0 GHz and is shown in Figure 43. As with the first resonant peak, the exposure to the sun light for 1 and 20 hours has caused a shift in the resonant frequency from 2.921 GHz for as-deposited P3HT:PCBM film to 2.903 GHz and 2.887 GHz when exposed to 1 h and 20 h respectively. The amplitude of the peak has also experienced a change, in line with the behaviour of the first resonant peak.

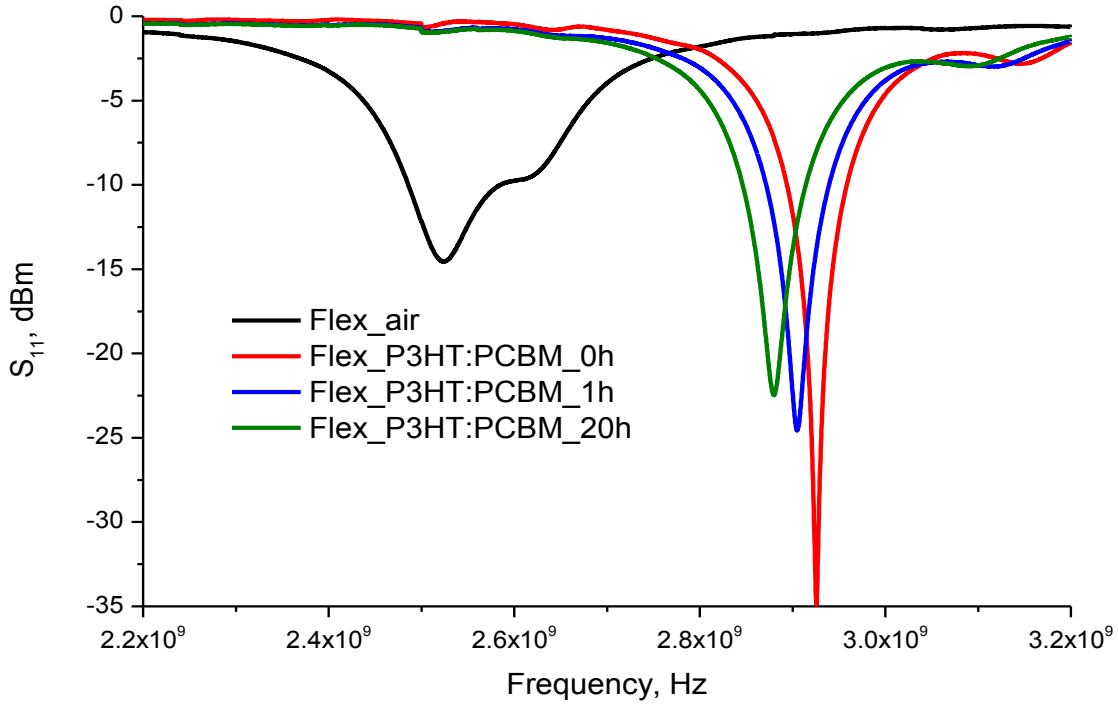

Figure 43. S_{11} signal distribution of the microwave sensor on flexible substrate with Ag pattern in 2.2-3.2 GHz frequency range when in contact with air and P3HT:PCBM films irradiated for 0, 1 and 20 hours.

However, the changes in the amplitude of the S_{11} signal in the subsequent third, fourth and fifth resonant peaks in the frequency range of 7.0-9.5 GHz were almost negligible, or within the experimental uncertainty, whereas the shift to the lower frequencies took place with increased exposure to sun light, following a trend set by the first and second resonant peaks. S_{11} signal distribution of the microwave sensor on flexible substrate with Ag pattern in 6.0-10.0 GHz frequency range when in contact with air and P3HT:PCBM films irradiated for 0, 1 and 20 hours is depicted in Figure 44.

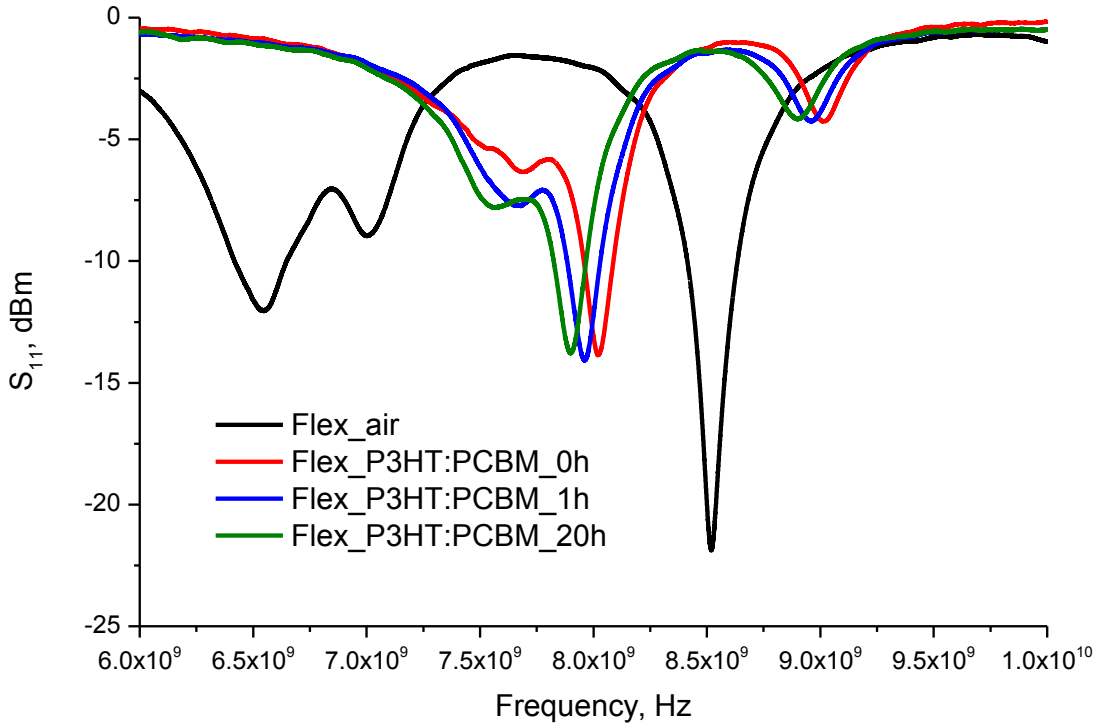

Figure 44. S_{11} signal distribution of the microwave sensor on flexible substrate with Ag pattern in 6.0-10.0 GHz frequency range when in contact with air and P3HT:PCBM films irradiated for 0, 1 and 20 hours.

The experiments using EM sensors on flexible substrates with P3HT:PCBM films deposited over them revealed that exposure to Q-Sun light clearly resulted in a change in the dielectric properties of the films, causing both shift in the position of all the resonant peaks and changes in their amplitudes, which were especially evident for the first and second resonant peaks.

4.2.5. Solar Exposure Effects on a Microwave sensor with a Rogers substrate and a Cu pattern

To confirm that the observed behaviour trend described in Section 4.2.3 is indeed the property of the produced P3HT:PCBM films and not effected principally by the design

and the materials of the EM sensor, the following section describes the results of the studies of the films deposited on sensors with Rogers substrate, which had Cu metal for the purpose of back layer and front antenna pattern. The measurements were perform in a similar fashion, with films being exposed to simulated sun light for 1 hour and 20 hours and their properties were recorded at 0.01-15 GHz frequency range, while all other environmental parameters were kept constant. This is to ensure that any changes in the material's dielectric properties are only connected with the influence of solar irradiation. Moreover, as in previous case, it was proven that time alone, i.e. 20 hours, does not cause measurable changes in the material properties that can be recorded with this electromagnetic wave sensing method. This fact was confirmed by repeatedly measuring as-deposited P3HT:PCBM films over a period of time comparable with the time it took to achieve equivalent of 20 hours solar exposure. However, this is only valid when the films were kept in air-tight container at constant environmental conditions, as exposure to elevated temperatures, humidity or any physical or chemical substances, including gases, could lead to deterioration of the material properties to a degree that they would not be suitable for PV purposes. However, it is beyond the scope of this work to investigate the range of operational parameters that are suitable for reliable long-term operation of P3HT:PCBM films for conversion of the solar energy into electricity. The aim is to prove the concept that this novel material composition, deposited using the procedure described in Section 3.2.3, is a suitable candidate for cost-effective organic solar cells.

Accordingly, Figure 45 depicts S_{11} signal distribution of the electromagnetic wave sensor on Rogers substrate with Cu pattern in 0.01-15.0 GHz frequency range when in contact with air and P3HT:PCBM films irradiated for 0, 1 and 20 hours. The change in the dielectric properties of the film as a result of the solar irradiation influence is clearly

visible in the whole measurement spectra range. However, the changes in the electromagnetic wave spectra distribution are more pronounced at or near the resonant peak regions. Thus, Figure 46 focuses more closely on 6.5-8.5 GHz frequency region, which contains third and fourth resonant peaks. Interestingly, the third resonant peak frequency changes with the exposure time, shifting towards lower frequencies as the time progresses. For as-deposited P3HT:PCBM film the third peak frequency was recorded at 7.41 GHz, and it has decreased to 7.29 GHz after 1 hour irradiation exposure and further to 7.21 GHz after 20 hours of exposure. Regarding the peak amplitude values, they remained reasonably stable after the initial 1 hour irradiation.

Contrary to this behaviour, the forth resonant peak amplitude has experienced dramatic changes in its module values, i.e. from -11 dBm for as-deposited films to -31 dBm after 20 hours of simulated sun light exposure. At the same time, a gradual shift towards the lower frequencies can be noticed at this forth resonant peak, caused by the increase in the exposure time. Although this trend is in line with behaviour of the third resonant peak, the changes are ten-fold smaller, i.e. the reduction is at the range of MHz, rather than GHz.

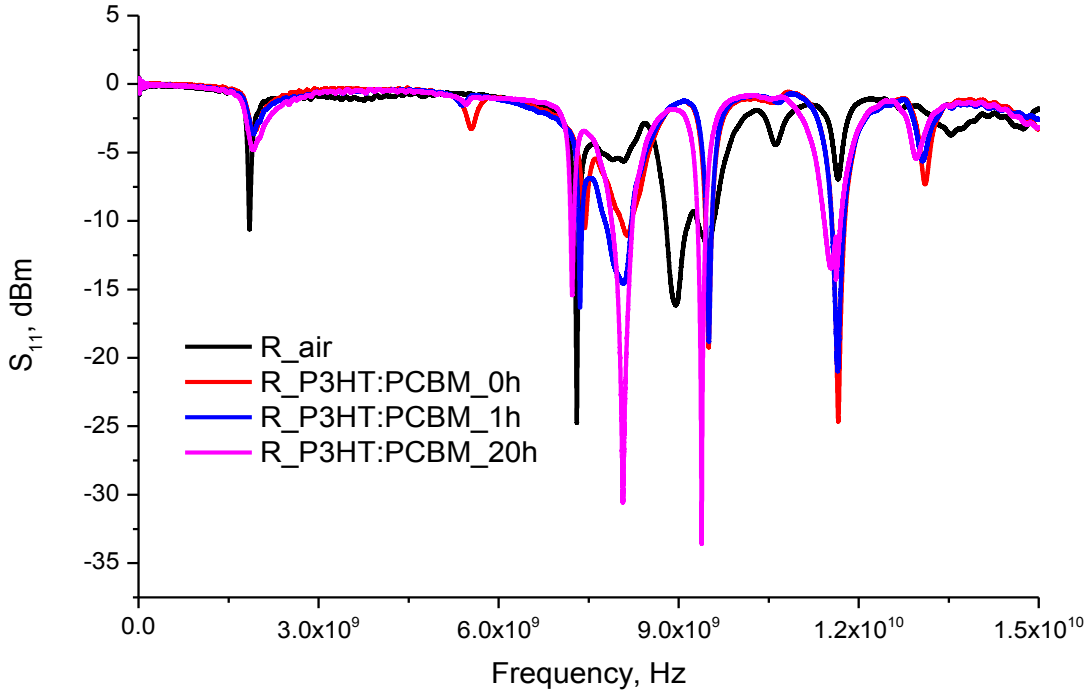

Figure 45. S_{11} signal distribution of the electromagnetic wave sensor on Rogers substrate with Cu pattern in 0.01-15.0 GHz frequency range when in contact with air and P3HT:PCBM films irradiated for 0, 1 and 20 hours.

Notably, with both types of the electromagnetic sensors used, all the results reported above show clear considerable change in the dielectric properties of deposited P3HT:PCBM films caused by the exposure to solar irradiation. Both signal amplitude changes and resonant peaks frequency shifts were recorded, and since all other experimental parameters and environmental conditions were kept constant, it is reasonable to conclude that the proposed methods of microwave spectroscopy is a reliable tool to trace the changes in the properties of the materials caused by the simulated Q-Sun irradiation.

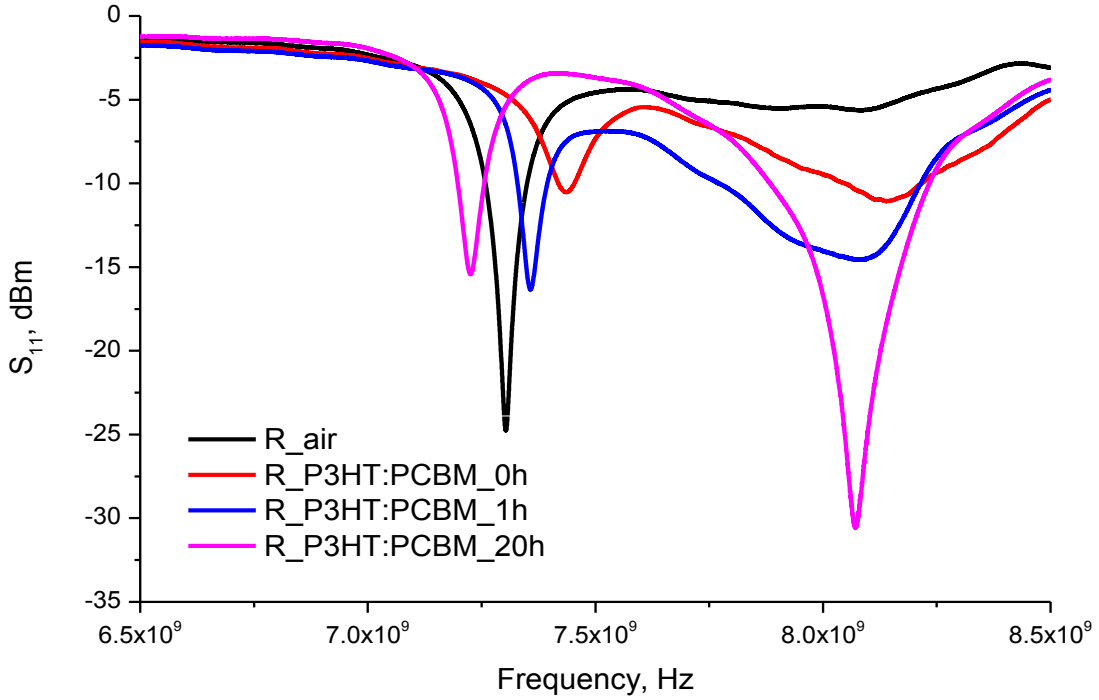

Figure 46. S_{11} signal distribution of the microwave sensor on Rogers substrate with Cu pattern in 6.5-8.5 GHz frequency range when in contact with air and P3HT:PCBM films irradiated for 0, 1 and 20 hours.

The next section focuses on the investigation of the changes in the optical properties of the P3HT:PCBM films under the influence of sun light, in an attempt to reveal the correlation between the properties and the exposure effects. Once it is achieved, it would assist in predicting the behaviour of complex composite organic films for PV purposes and accordingly could suggest new materials compositions to achieve the desired solar cells performance in various conditions.

4.3. Optical Properties of P3HT:PCBM

4.3.1. Optical Properties of P3HT:PCBM Solutions

The absorption spectra measurements of the raw solutions were taken using the Perkin Elmer Lambda 900 UV/VIS/NIR spectrophotometer. To begin, the background correction was set by inserting a blank cuvette and running the spectrometer. Regio-regular P3HT was used as a light absorbing and electron donating material, while a soluble C_{60} derivative, PCBM was used as the acceptor material. The optical absorption spectra of these solutions were recorded on numerous occasions to ensure validity of the results. Three solution samples: PCBM, P3HT and PCBM:P3HT were prepared and inserted in glass cuvettes. For the PCBM sample, 10 mg of acceptor fullerene PCBM was dissolved in 1 ml dichlorobenzene. In P3HT sample, 10 mg of donor polymer P3HT was dissolved in 1 ml of dichlorobenzene, and for PCBM:P3HT solutions these were mixed at a ratio of 1:1 volume. The samples were combined by pumping forward and back through a syringe into a test tube with approximately 8 to 10 repetitions. Figure 47 illustrates the spectra for PCBM, P3HT and PCBM:P3HT solutions.

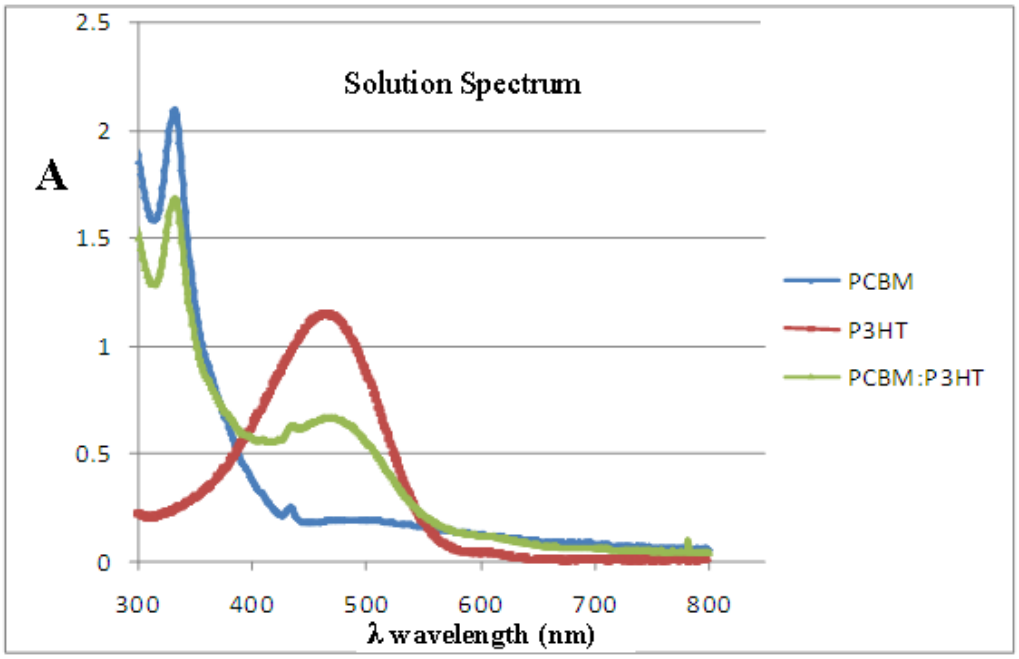

Figure 47. Illustration of the spectra for PCBM, P3HT and PCBM:P3HT solutions.

Observing from the higher wavelength the PCBM solution, these spectra show optical absorbance gradually increasing as the wavelength decreases. In molecular C_{60} in toluene solution, a similar sharp peak is observed at ~410 nm, and this derives from transitions between molecular orbitals. A similar peak is observed at approximately ~420 nm in this experiment in dichlorobenzene solution. The C_{60} Fullerene solution also illustrates a typical finger print peak at approximately ~330 nm. In the spectral range between 350 nm and 198 nm, three absorption peaks are distinct, at 328 nm, 256 nm and 211 nm. Peaks at 430 nm to 350 nm region can be explained by electronic transitions that demonstrate some vibrational structure [180-182].

In this work, P3HT with a LUMO level of 3.1 eV was used, and its absorption spectrum in dichlorobenzene was demonstrated. This illustrates the typical peak absorption wave band for P3HT at about 420 nm to 600 nm.

4.3.2. The effect of Annealing on the Optical Properties of P3HT:PCBM Films

This section reports on the effect of the annealing on the optical properties of P3HT:PCBM films. Three thin film samples of P3HT:PCBM were prepared by spin coating onto 1 inch glass substrates. The substrates were cleaned with acetone and ultra-sonicated in de-ionised water for 15 minutes, then wiped with ethanol and methanol with lint free wipes respectively. Again, 10 mg of P3HT and PCBM was dissolved in 1 ml of solvent 1,2dichlorobenzene. The solution was spin coated on the glass substrates for 45 seconds at 1500 rpm in order to achieve an approximately 80 – 100 nm thick layer. To confirm the individual characteristics and layer thickness, AFM was used, as described earlier in Section 4.1. The solutions were then mixed at a ratio of 1:1 and also spin coated on the glass substrates. Sample 1 was annealed at 90 °C for 10 minutes, sample 2 and 3 were both dried naturally at room temperature and the absorption spectra of these samples were then recorded.

For the P3HT:PCBM films fabricated from 1,2 dichlorobenzene solvent, Figure 48 shows the UV spectra for a 1:1 ratio blend thin films of three samples. It is clear that annealing has affectively increased the absorption spectra of the films and therefore this manufacturing step was used during the fabrication of the organic solar cell prototype device. The λ-*max* is 558 nm showing a red-shift and clear shoulders appear at 525 nm and 610 nm. These shoulders are explained by the high degree of ordering in P3HT [183]. The peak in the absorption may be attributed to an interchain interaction among P3HT chains. UV-Vis absorption bands were observed at 335, 565 and 615 nm. The peaks below the 350 nm range are directly associated to the added PCBM fullerene. The peaks above this range are the P3HT characteristic peaks in the absorption wavelength of 450 – 650 nm.

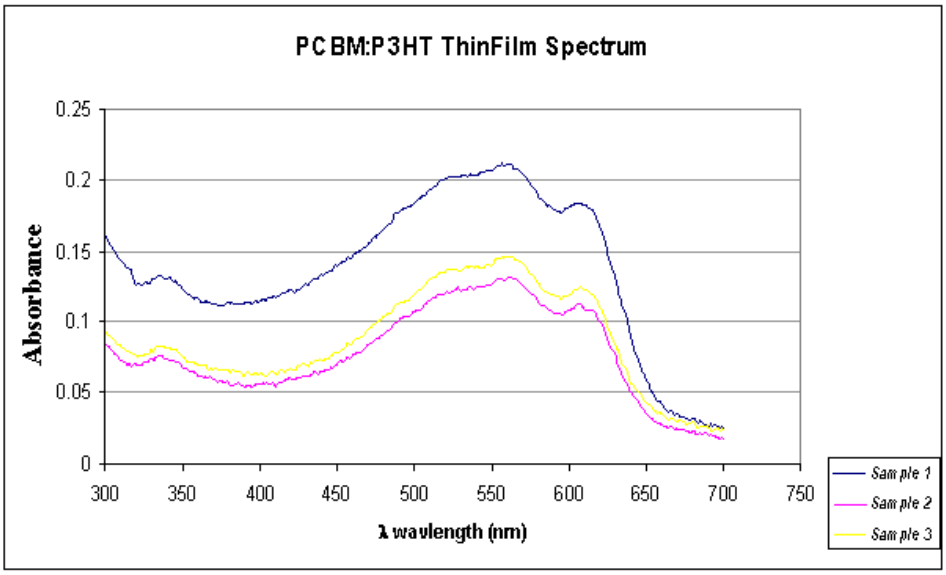

Figure 48. UV-Vis absorption of P3HT:PCBM thin films spin coated from 1,2 dichlorobenzene (1:1) annealed and dried naturally.

4.3.3. The effect of Q-sun Exposure on the Optical Properties of P3HT:PCBM Films

Table 4 details the Q-Sun Xenon Test Chamber Settings used for the exposure of manufactured organic films to simulated solar irradiation, with the view to trace the illumination – induced changes in the properties of these films.

Table 4. Q-Sun Xenon Test Chamber Settings

	Irradiance		°C	Step Time	Test Time		Total Time (Hours Elapsed)
Actual:	0.6		30	16:51	8245	20473.1	10429
Set:	0.6	340	30	50:00:00	2000		20473.1
	W/m2	@nm		Hours:Min	Hours	kJ/m2	kJ/m2 Elapsed

Figure 49 contains a series of screen-shot images from the UV-Vis Spectrometer that trace the changes in the optical absorption spectra after 0, 10 min, 20 min, 40 min and 30 hours of irradiation.

It can clearly be seen that, as result of exposure to simulated sunlight, the optical absorption, across the spectral range is diminished. Figure 49 shows for example the absorbance at 500nm as a function of exposure time. Such a "bleaching" of the absorbance in the visible region is typical of photooxidation of the π-electron system, reducing the molecular conjugation [184].

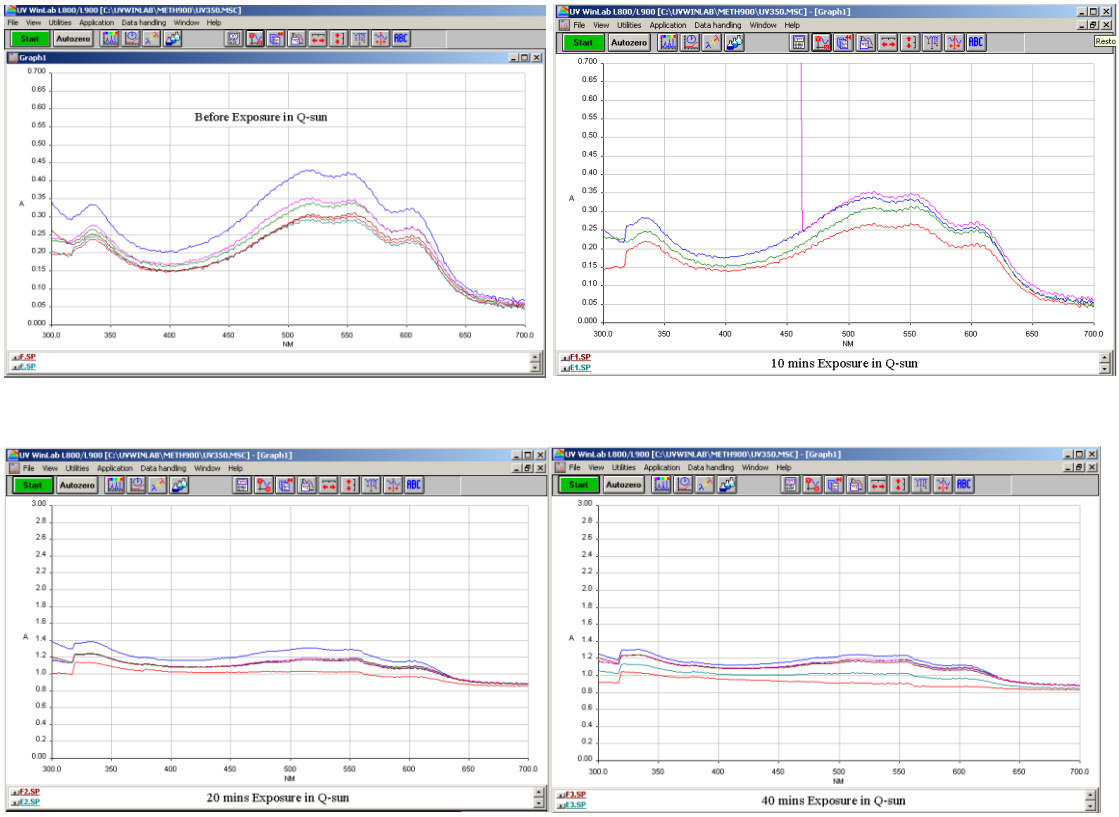

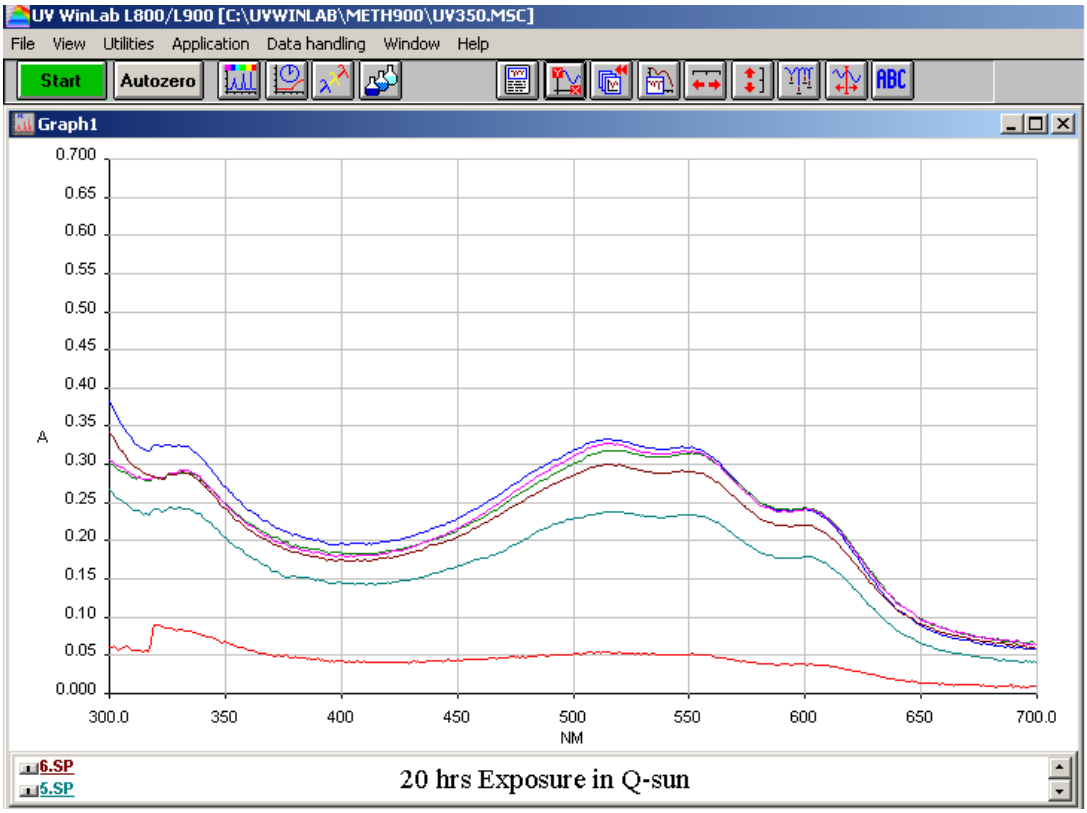

Figure 49. Screen-shot images that trace the changes in the optical absorption spectra after 0, 10 min, 20 min, 40 min and 20 hours of irradiation.

4.4. Electrical Properties of P3HT:PCBM Films

This experiment was done in parallel with the absorption experiment described above. In order to measure the optical and electrical measurements, both the glass samples (for optical) and samples with screen-printed IDE electrodes (for electrical measurements) were prepared simultaneously from the same solutions and their exposure to solar irradiation was carried out together. Spin coating, annealing and Q-sun exposure times were all kept identical for comparison purposes.

Four IDE samples were prepared by spin coating with the same spin parameters, with the active layer from P3HT:PCBM solution. The samples were then annealed in an oven

at 90°C for 10 mins. Figure 50 illustrates 2 IDE structures screen printed on a ceramic substrate (as originally shown in figure 13) with the spin coated active layer. Each IDE structure has 2 contacts which are called measurement point 1 (MP.1) and measurement point 2 (MP.2). The resistance of the active layer is measured across these contacts, before and after exposure to the simulated solar irradiance in the Q-sun. The results were recorded before exposure and after 10 min, 20 min, 40 min and 20 hours. These results are tabulated in Table 5 for MP.1 and Table 6 for MP.2. Notably, after 0 to 40 min exposure, all samples showed a decrease in resistance, and for all plots except Sample 4 MP.1, the resistance increases with the increase from 40 to 1200 mins exposure.

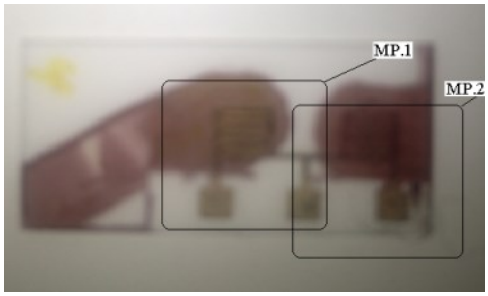

Figure 50. Measurement points for the electrical characterisation of the films.

Table 5. Electrical properties measurements for the four samples at MP.1.

	Sample 1	Sample 2	Sample 3	Sample 4
1	28.4	39.5	32.3	39.5
10	21.5	30.6	30.4	37.5
20	17.8	23.2	19.1	36.6
40	12.4	17.1	14.5	35.5
1200	36.2	42	49.2	30.2

1200

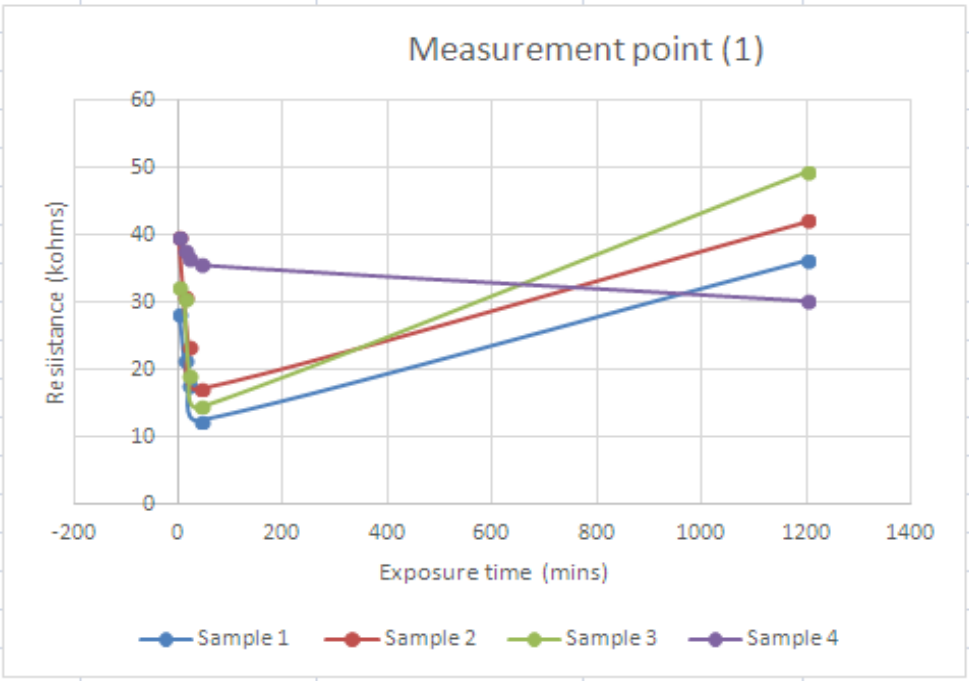

Figure 51. Dependence of the resistance on exposure time for the four samples at MP.1.

Table 6. Electrical properties measurements for the four samples at MP.2.

	Sample 1	Sample 2	Sample 3	Sample 4
0	34.9	17.9	43.6	19.9
10	24.7	15.9	25.1	17.6
20	23.7	14.8	21.8	13.8
40	20.4	10.1	17.2	10.37
1200	44.6	20	37.3	29.9

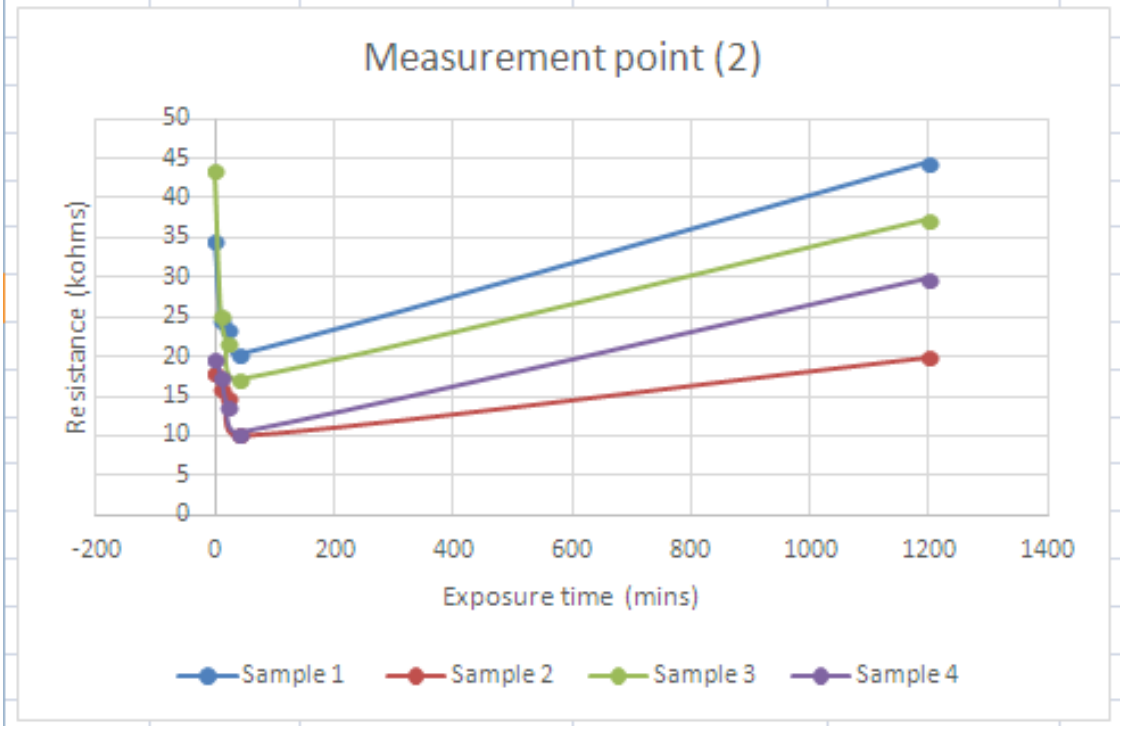

Figure 52. Dependence of the resistance on exposure time for the four samples at MP.2.

Analysing together the changes in the dielectric, optical and the electrical properties of the manufacture organic thin films, one may firmly conclude that there exists a strong correlation between these changes, and the results showed a certain repeatable trend. In the next section, a flexible organic solar cell device was designed, constructed and tested.

4.5. Flexible Solar Cell Prototype Testing

The aim of this research was to build a novel cost-effective organic solar cell structure suitable for the next-generation flexible applications with enhanced solar irradiation conversion efficiency. This section summarises the testing results. Figure 53 illustrates the experimental setup for the flexible solar cell prototype characterisation. On the left side of Figure 53, the solar cell is illuminated by the Fostec lamp. Behind the solar cell is a pyranometer which measures the light intensity. Figure 54 shows the pyranometer from Kipp & Zonen in more detail On the right hand side of Figure 53, the Keithley voltage source meter is illustrated and connected to a PC running a LabView program. This program records the currents through the solar cell for each voltage input and plots the I-V and Power-V characteristics for the solar cell.

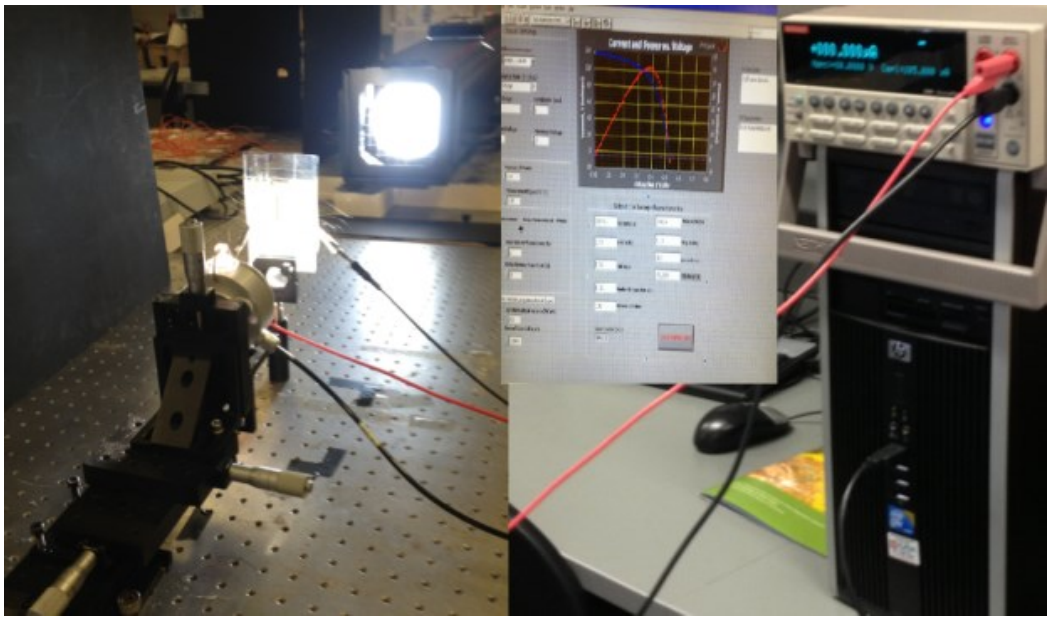

Figure 53. Experimental setup for solar cell prototype characterisation.

Figure 54. Pyranometer from Kipp & Zonen, for measuring the simulated solar irradiance/light intensity.

Figure 55 displays the graphical interface for testing the electrical properties of the constructed solar cell prototype. This figure illustrates the current and power vs voltage curves for a commercially available solar cell. Figure 56 illustrates the current-voltage characteristics and the power versus voltage characteristic of the flexible solar cell.

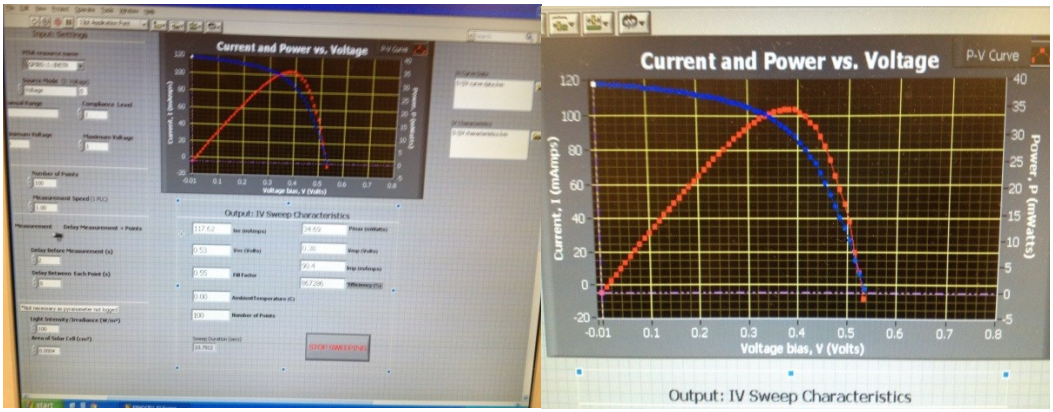

Figure 55. Graphical interface illustrating the electrical properties of a commercially available solar cell.

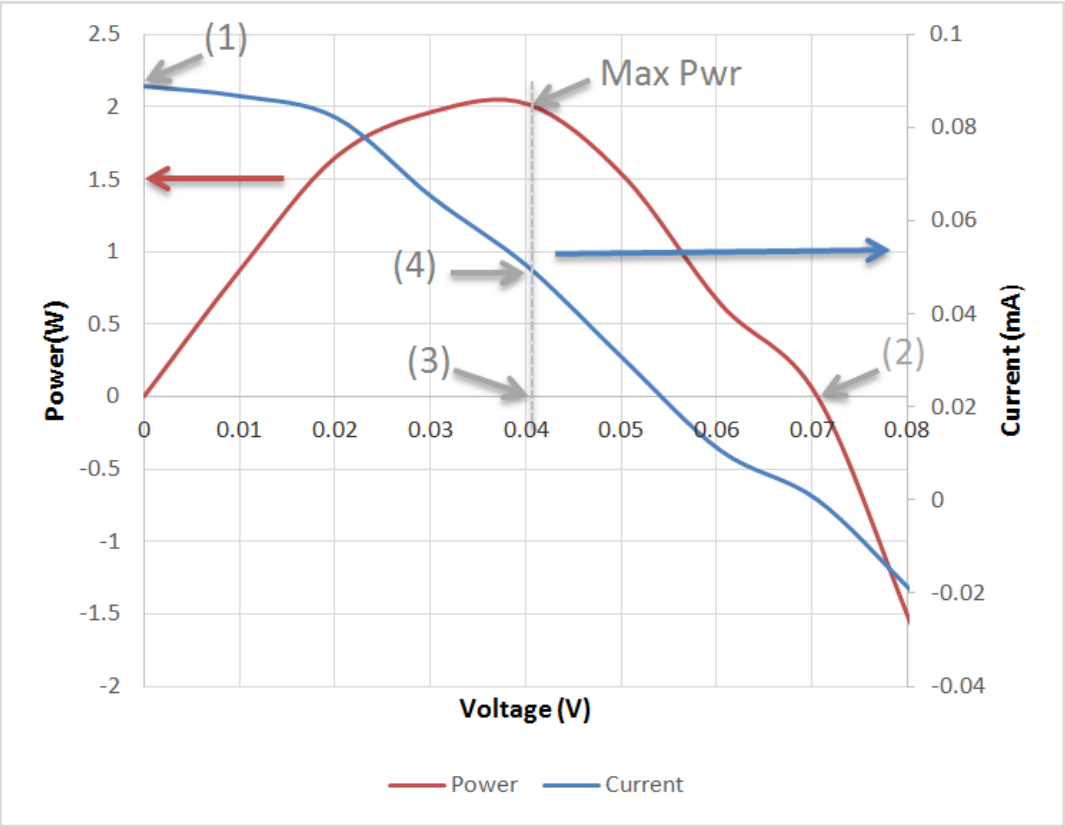

Figure 56. (a) Current-voltage characteristics of the prototype solar cell and (b) the dependence of power on voltage.

From Figure 56, it can be observed the short circuit current (J_{sc}) is 88.9 µA (1), while the open circuit voltage (V_{oc}) is 71 mV (2). Maximum power V_m occurs at a voltage of 40.326 mV (3) and the corresponding current at this voltage is ~50 µA (4). From these values, the fill factor (FF) can be concluded using Eq. 3 to be 0.3238. Fill factors above 0.7 are expected for more ideal cells. The losses in fill factor could be due to high series resistance in the contacts and low shunt resistance in the cell. In Figure 56, the current begins to drop quite quickly after a voltage of 20 mV. If the series resistance is low (more desirable), then the voltage at which the current starts to drop would be much higher, and much closer to the open circuit voltage.

The calculated efficiency is 0.499%. These results indicate high power loss and can be attributed to shunt resistance in the cell, i.e. an alternative path in the cell for current to flow. This is more than likely caused by manufacturing flaws/problems rather than the actual cell design. In addition, high shunt resistance causes a loss in voltage produced by the cell, as is the case in this cell. An open circuit voltage of 71 mV is achieved in this cell, when a value of greater than 400 mV would be expected for a well manufactured cell.

Chapter 5: Summary, Conclusion and Future Work

This research thesis reported on the experimental work conducted is in the area of renewable energy production, in particular in the design, manufacture and characterisation of advanced cost-effective printed solar cells based on the organic materials. It was shown that organic photovoltaic devices offer several advantages over expensive silicon solar cells, including deposition of ultra-thin films by spin-coating, printing and spray-coating. This in turn provides for the exciting possibility to make lightweight, flexible solar cells for a broad range of existing and emerging applications for security, military and medicine.

In Chapter 1, the research area is presented and the need for developing new materials and manufacturing techniques for sustainable solar cells is justified. Chapter 2 reviewed the traditional pn-junction solar cells and the factors that limit their performance. The state-of-the-art organic solar cell is also discussed.

Chapter 3 presented the experimental procedure used in this body of work, including the materials and equipment utilised, electrodes design methods and parameters, the preparation methods for the organic films, and the test setups for the electrical and optical properties characterisation.

In Chapter 4, the results of the optical and electrical tests are presented, with specific emphasis on the novel approach used to characterise the dielectric properties of the materials, microwave spectroscopy. The fundamental principles of operation and design

of the sensors are comprehensively discussed. The dielectric properties of the P3HT:PCBM films using microwave spectroscopy were presented. Two types of EM waves sensors were fabricated, one on a Rogers substrate with Cu patterns and a second on a flexible substrate with Ag patterns. Both of these EM sensors demonstrated shifts in resonant peak frequencies and amplitude during exposure to solar irradiation. During these experiments, all other experimental parameters and environmental conditions were kept constant. Therefore, it was reasonable to conclude that the proposed methods of microwave spectroscopy is a reliable tool to trace the changes in the properties of the materials caused by the simulated Q-Sun irradiation.

The optical properties of the P3HT:PCBM films displayed a decrease in absorbance up to 40 mins solar simulator irradiation and then an increase in absorbance from 40 min to 20 hrs.

The electrical properties of P3HT:PCBM films showed a resistance decrease as the films were illuminated by an AM1.5 solar simulator from 0 to 40 min, and a subsequent increase in resistance up to 20 hrs.

To finish, a bespoke solar cell on flexible PET was constructed and tested. It exhibited a fill factor and an efficiency of 0.3238 and 0.49% respectively. It should be remembered these P3HT:PCBM films were fabricated in open air in order to mimic a mass-production environment. As a consequence, problems occur in the manufacturing process thus degrading the solar cell performance. Various past published work on organic solar cells are manufactured in nitrogen glove boxes to guarantee reproducible and optimal results. Solving the problems pertaining to open air fabrication is crucial step in the production of mass produced rigid and flexible polymer solar cells.

References

[1] Y. Sun and G. Shi, "Graphene/polymer composites for energy applications," *Journal of Polymer Science, Part B: Polymer Physics,* vol. 51, pp. 231-253, 2013.

[2] Z. Abdin, M. A. Alim, R. Saidur, M. R. Islam, W. Rashmi, S. Mekhilef, and A. Wadi, "Solar energy harvesting with the application of nanotechnology," *Renewable and Sustainable Energy Reviews,* vol. 26, pp. 837-852, 2013.

[3] T. D. Nielsen, C. Cruickshank, S. Foged, J. Thorsen, and F. C. Krebs, "Business, market and intellectual property analysis of polymer solar cells," *Solar Energy Materials and Solar Cells,* vol. 94, pp. 1553-1571, 2010.

[4] F. C. Krebs, S. A. Gevorgyan, B. Gholamkhass *et al*, "A round robin study of flexible large-area roll-to-roll processed polymer solar cell modules," *Solar Energy Materials and Solar Cells,* vol. 93, pp. 1968-1977, 2009.

[5] E. Klimov, W. Li, X. Yang, G. G. Hoffmann, and J. Loos, "Scanning Near-Field and Confocal Raman Microscopic Investigation of P3HT−PCBM Systems for Solar Cell Applications," *Macromolecules,* vol. 39, pp. 4493-4496, 2006.

[6] B. Arredondo, C. De Dios, R. Vergaz, A. R. Criado, B. Romero, B. Zimmermann, and U. Wurfel, "Performance of ITO-free inverted organic bulk heterojunction photodetectors: Comparison with standard device architecture," *Organic Electronics: physics, materials, applications,* vol. 14, pp. 2484-2490, 2013.

[7] M. A. Rahman, A. Rahim, M. Maniruzzaman, K. Yang, C. Lee, H. Nam, H. Soh, and J. Lee, "ITO-free low-cost organic solar cells with highly conductive

poly(3,4 ethylenedioxythiophene): P-toluene sulfonate anodes," *Solar Energy Materials and Solar Cells,* vol. 95, pp. 3573-3578, 2011.

[8] W. Yu, F. Meng, Y. Wang, P. Xu, and L. Shen, "ITO-free polymer solar cells with Ag/WO3 semi-transparent electrodes," in *2012 International Symposium on Photonics and Optoelectronics, SOPO 2012,* Shanghai, China, IEEE Photonics Society; IEEE Wuhan Section; Optics Photonics Society of Singapore; Wuhan University; Beijing Jiaotong University.

[9] D. Angmo, T. T. Larsen-Olsen, M. Jrgensen, R. R. Sndergaard, and F. C. Krebs, "Roll-to-roll inkjet printing and photonic sintering of electrodes for ITO free polymer solar cell modules and facile product integration," *Advanced Energy Materials,* vol. 3, pp. 172-175, 2013.

[10] J. Bergqvist, C. Lindqvist, O. Backe, Z. Ma, Z. Tang, W. Tress, S. Gustafsson, E. Wang, E. Olsson, M. R. Andersson, O. Inganas, and C. Muller, "Sub-glass transition annealing enhances polymer solar cell performance," *Journal of Materials Chemistry A,* vol. 2, pp. 6146-6152, 2014.

[11] Y. A. M. Ismail, T. Soga, and T. Jimbo, "The contribution of coumarin 6 in light harvesting and photocurrent of P3HT:PCBM bulk heterojunction solar cell," *Solar Energy Materials and Solar Cells,* vol. 94, pp. 1406-1411, 2010.

[12] M. G. Sousa, A. F. Da Cunha, P. A. Fernandes, J. P. Teixeira, R. A. Sousa, and J. P. Leitao, "Effect of rapid thermal processing conditions on the properties of Cu 2ZnSnS4 thin films and solar cell performance," *Solar Energy Materials and Solar Cells,* vol. 126, pp. 101-106, 2014.

[13] C.-T. Wu, H.-P. Kuo, H.-A. Tsai, and W.-C. Pan, "Rapid dye-sensitized solar cell working electrode preparation using far infrared rapid thermal annealing," *Applied Energy,* vol. 100, pp. 138-143, 2012.

[14] J. Yang and T.-Q. Nguyen, "Effects of thin film processing on pentacene/C60 bilayer solar cell performance," *Organic Electronics: physics, materials, applications,* vol. 8, pp. 566-574, 2007.

[15] C. Sirisamphanwong and C. Sirisamphanwong, "The Effect of Photon Flux Density and Module Temperature on Power Output of Photovoltaic Array," *Energy Procedia,* vol. 34, pp. 430-438, 2013.

[16] J. K. Rath, "Thin-Film Silicon Solar Cells," in *Advanced Silicon Materials for Photovoltaic Applications*, ed: John Wiley & Sons, Ltd, 2012, pp. 311-353.

[17] B. Sopori, "Thin-Film Silicon Solar Cells," in *Handbook of Photovoltaic Science and Engineering*, ed: John Wiley & Sons, Ltd, 2005, pp. 307-357.

[18] A. Kitai, "The PN junction Diode," in *Principles of Solar Cells, LEDs and Diodes: The role of the PN junction*, ed: John Wiley & Sons, Ltd, 2011, pp. 69-122.

[19] J. J. Loferski, "Photovoltaic Devices," in *digital Encyclopedia of Applied Physics*, ed: WILEY-VCH Verlag GmbH & Co KGaA, 2003.

[20] J. Toušek, "Photovoltaic Effect in Heterojunctions with Recombination in the Space Charge Region," *physica status solidi (a),* vol. 137, pp. 277-285, 1993.

[21] D. Vincenzi, M. A. Butturi, V. Guidi, M. C. Carotta, G. Martinelli, V. Guarnieri, S. Brida, B. Margesin, F. Giacomozzi, M. Zen, G. U. Pignatel, A. A. Vasiliev, and A. V. Pisliakov, "Development of a low-power thick-film gas sensor deposited by screen-printing technique onto a micromachined hotplate," *Sensors and Actuators, B: Chemical,* vol. 77, pp. 95-99, 2001.

[22] D. Rekioua and E. Matagne, "Modeling of Solar Irradiance and Cells," in *Optimization of Photovoltaic Power Systems*, ed: Springer London, 2012, pp. 31-87.

[23] S. M. Sze and K. K. Ng, "Physics and Properties of Semiconductors—A Review," in *Physics of Semiconductor Devices*, ed: John Wiley & Sons, Inc., 2006, pp. 5-75.

[24] S. Tsuda, T. Matsuyama, M. Kameda, K. Wakisaka, S. Nakano, M. Ohnishi, and Y. Kuwano, "Development of New Technologies for High-Efficiency A-Si Solar Cells," in *Clean and Safe Energy Forever*, T. Horigome, K. Kimura, T. Takakura, T. Nishino, and I. Fujii, Eds., ed Oxford: Pergamon, 1990, pp. 142-146.

[25] "Konarka-Power-Plastic-achieves-8.3%-efficiency-certification-from-NREL," *Renewable Energy World,* 29 Nov 2010 2010.

[26] T. Nozawa, "Mitsubishi Chemical Claims Efficiency Record for Organic Thin-film PV Cell," 1 Jun 2012 2012.

[27] C. A. Gueymard, D. Myers, and K. Emery, "Proposed reference irradiance spectra for solar energy systems testing," *Solar Energy,* vol. 73, pp. 443-467, 2002.

[28] W. Durisch, J. Urban, and G. Smestad, "Characterisation of solar cells and modules under actual operating conditions," *Renewable Energy,* vol. 8, pp. 359-366, 1996.

[29] S. V. Boriskina and G. Chen, "Exceeding the solar cell Shockley–Queisser limit via thermal up-conversion of low-energy photons," *Optics Communications,* vol. 314, pp. 71-78, 2014.

[30] C. Strümpel, M. McCann, G. Beaucarne, V. Arkhipov, A. Slaoui, V. Švrček, C. del Cañizo, and I. Tobias, "Modifying the solar spectrum to enhance silicon solar cell efficiency—An overview of available materials," *Solar Energy Materials and Solar Cells,* vol. 91, pp. 238-249, 2007.

[31] W. Shockley and H. J. Queisser, "Detailed Balance Limit of Efficiency of p-n Junction Solar Cells," *Journal of Applied Physics,* vol. 32, pp. 510-519, 1961.

[32] N. Robertson, "Organic Photovoltaics. Mechanisms, Materials, and Devices. Herausgegeben von Sam-Shajing Sun und Niyazi S. Sariciftci," *Angewandte Chemie,* vol. 118, pp. 7479-7479, 2006.

[33] J. Szlufcik, G. Agostinelli, F. Duerinckx, E. V. Kerschaver, and G. Beaucarne, "IIb-2 - Low cost industrial technologies of crystalline silicon solar cells," in *Solar Cells*, T. Markvart and L. Castañer, Eds., ed Oxford: Elsevier Science, 2005, pp. 89-120.

[34] H. Wirth, "Chapter Three - Crystalline Silicon PV Module Technology," in *Semiconductors and Semimetals*. vol. Volume 89, P. W. Gerhard and R. W. Eicke, Eds., ed: Elsevier, 2013, pp. 135-197.

[35] A. Alemu, A. Freundlich, N. Badi, C. Boney, and A. Bensaoula, "Low temperature deposited boron nitride thin films for a robust anti-reflection coating of solar cells," *Solar Energy Materials and Solar Cells,* vol. 94, pp. 921-923, 2010.

[36] H. Cui, S. Pillai, P. Campbell, and M. Green, "A novel silver nanoparticle assisted texture as broadband antireflection coating for solar cell applications," *Solar Energy Materials and Solar Cells,* vol. 109, pp. 233-239, 2013.

[37] D. Zhang, I. A. Digdaya, R. Santbergen, R. A. C. M. M. van Swaaij, P. Bronsveld, M. Zeman, J. A. M. van Roosmalen, and A. W. Weeber, "Design and fabrication of a SiOx/ITO double-layer anti-reflective coating for heterojunction silicon solar cells," *Solar Energy Materials and Solar Cells,* vol. 117, pp. 132-138, 2013.

[38] R. Hoenig, A. Kalio, J. Sigwarth, F. Clement, M. Glatthaar, J. Wilde, and D. Biro, "Impact of screen printing silver paste components on the space charge region recombination losses of industrial silicon solar cells," *Solar Energy Materials and Solar Cells,* vol. 106, pp. 7-10, 2012.

[39] L. A. Kosyachenko, X. Mathew, V. Y. Roshko, and E. V. Grushko, "Optical absorptivity and recombination losses: The limitations imposed by the thickness of absorber layer in CdS/CdTe solar cells," *Solar Energy Materials and Solar Cells,* vol. 114, pp. 179-185, 2013.

[40] A. Shah, "Chapter IC-1 - Thin-Film Silicon Solar Cells," in *Practical Handbook of Photovoltaics (Second Edition)*, A. McEvoy, T. Markvart, and L. Castañer, Eds., ed Boston: Academic Press, 2012, pp. 209-281.

[41] J. Escarré, K. Söderström, M. Despeisse, S. Nicolay, C. Battaglia, G. Bugnon, L. Ding, F. Meillaud, F.-J. Haug, and C. Ballif, "Geometric light trapping for high efficiency thin film silicon solar cells," *Solar Energy Materials and Solar Cells,* vol. 98, pp. 185-190, 2012.

[42] H. Derouiche and V. Djara, "Impact of the energy difference in LUMO and HOMO of the bulk heterojunctions components on the efficiency of organic solar cells," *Solar Energy Materials and Solar Cells,* vol. 91, pp. 1163-1167, 2007.

[43] S.-S. Sun, "Design of a block copolymer solar cell," *Solar Energy Materials and Solar Cells,* vol. 79, pp. 257-264, 2003.

[44] K. Kawata, V. M. Burlakov, M. J. Carey, H. E. Assender, G. A. D. Briggs, A. Ruseckas, and I. D. W. Samuel, "Description of exciton transport in a TiO2/MEH–PPV heterojunction photovoltaic material," *Solar Energy Materials and Solar Cells,* vol. 87, pp. 715-724, 2005.

[45] L. Shi, Z. Zhou, and B. Tang, "Optimization of Si solar cells with full band optical absorption increased in all polarizations using plasmonic backcontact grating," *Optik - International Journal for Light and Electron Optics,* vol. 125, pp. 789-794, 2014.

[46] C. M. Proctor, M. Kuik, and T.-Q. Nguyen, "Charge carrier recombination in organic solar cells," *Progress in Polymer Science,* vol. 38, pp. 1941-1960, 2013.

[47] J. Gaume, C. Taviot-Gueho, S. Cros, A. Rivaton, S. Thérias, and J.-L. Gardette, "Optimization of PVA clay nanocomposite for ultra-barrier multilayer encapsulation of organic solar cells," *Solar Energy Materials and Solar Cells,* vol. 99, pp. 240-249, 2012.

[48] "http://www.nanochemistry.it/download/BHJ_0203t.gif."

[49] C.-H. Chia, W.-C. Fan, Y.-C. Lin, and W.-C. Chou, "Radiative recombination of indirect exciton in type-II ZnSeTe/ZnSe multiple quantum wells," *Journal of Luminescence,* vol. 131, pp. 956-959, 2011.

[50] J.-C. Wang, Y.-T. Liang, F.-C. Cheng, C.-H. Fang, H.-I. Chen, C.-Y. Tsai, J.-A. Jiang, and T.-E. Nee, "Enhancement of exciton radiative recombination for In-doped ZnO nanowires with aluminum cylindrical micropillars," *Journal of Luminescence,* vol. 136, pp. 11-16, 2013.

[51] J. J. M. Halls, K. Pichler, R. H. Friend, S. C. Moratti, and A. B. Holmes, "Exciton dissociation at a poly(p-phenylenevinylene)/C60 heterojunction," *Synthetic Metals,* vol. 77, pp. 277-280, 1996.

[52] J. S. Yeo, J. M. Yun, S. S. Kim, D. Y. Kim, J. Kim, and S. I. Na, "Variations of cell performance in ITO-free organic solar cells with increasing cell areas," *Semiconductor Science and Technology,* vol. 26, 2011.

[53] Y.-Y. Choi, S. J. Kang, H.-K. Kim, W. M. Choi, and S.-I. Na, "Multilayer graphene films as transparent electrodes for organic photovoltaic devices," *Solar Energy Materials and Solar Cells,* vol. 96, pp. 281-285, 2012.

[54] N. Espinosa, R. García-Valverde, A. Urbina, and F. C. Krebs, "A life cycle analysis of polymer solar cell modules prepared using roll-to-roll methods under ambient conditions," *Solar Energy Materials and Solar Cells,* vol. 95, pp. 1293-1302, 2011.

[55] J. Ajuria, I. Ugarte, W. Cambarau, I. Etxebarria, R. Tena-Zaera, and R. Pacios, "Insights on the working principles of flexible and efficient ITO-free organic solar cells based on solution processed Ag nanowire electrodes," *Solar Energy Materials and Solar Cells,* vol. 102, pp. 148-152, 2012.

[56] F. Guo, X. Zhu, K. Forberich, J. Krantz, T. Stubhan, M. Salinas, M. Halik, S. Spallek, B. Butz, E. Spiecker, T. Ameri, N. Li, P. Kubis, D. M. Guldi, G. J. Matt, and C. J. Brabec, "ITO-free and fully solution-processed semitransparent organic solar cells with high fill factors," *Advanced Energy Materials,* vol. 3, pp. 1062-1067, 2013.

[57] Y.-C. Huang, F.-H. Hsu, H.-C. Cha, C.-M. Chuang, C.-S. Tsao, and C.-Y. Chen, "High-performance ITO-free spray-processed polymer solar cells with incorporating ink-jet printed grid," *Organic Electronics: physics, materials, applications,* vol. 14, pp. 2809-2817, 2013.

[58] Y. Li, L. Mao, Y. Gao, P. Zhang, C. Li, C. Ma, Y. Tu, Z. Cui, and L. Chen, "ITO-free photovoltaic cell utilizing a high-resolution silver grid current collecting layer," *Solar Energy Materials and Solar Cells,* vol. 113, pp. 85-89, 2013.

[59] R. R. Sondergaard, M. Hosel, M. Jrgensen, and F. C. Krebs, "Fast printing of thin, large area, ITO free electrochromics on flexible barrier foil," *Journal of Polymer Science, Part B: Polymer Physics,* vol. 51, pp. 132-136, 2013.

[60] S. Wilken, D. Scheunemann, V. Wilkens, J. Parisi, and H. Borchert, "Improvement of ITO-free inverted polymer-based solar cells by using colloidal zinc oxide nanocrystals as electron-selective buffer layer," *Organic Electronics: physics, materials, applications,* vol. 13, pp. 2386-2394, 2012.

[61] W. Yu, L. Shen, F. Meng, Y. Long, S. Ruan, and W. Chen, "Effects of the optical microcavity on the performance of ITO-free polymer solar cells with WO3/Ag/WO3 transparent electrode," *Solar Energy Materials and Solar Cells,* vol. 100, pp. 226-230, 2012.

[62] D. S. Hecht and R. B. Kaner, "Solution-processed transparent electrodes," *MRS Bulletin,* vol. 36, pp. 749-755, 2011.

[63] K. Ueno, "Solution processed graphene transparent conductive film," 2012, pp. 49-52.

[64] Y. Wu, X. Zhang, J. Jie, C. Xie, B. Sun, Y. Wang, and P. Gao, "Graphene transparent conductive electrodes for highly efficient silicon nanostructures-based hybrid heterojunction solar cells," *Journal of Physical Chemistry C,* vol. 117, pp. 11968-11976, 2013.

[65] Q. Zhang, X. Wan, F. Xing, L. Huang, G. Long, N. Yi, W. Ni, Z. Liu, J. Tian, and Y. Chen, "Solution-processable graphene mesh transparent electrodes for organic solar cells," *Nano Research,* vol. 6, pp. 478-484, 2013.

[66] D. Angmo and F. C. Krebs, "Flexible ITO-free polymer solar cells," *Journal of Applied Polymer Science,* vol. 129, pp. 1-14, 2013.

[67] Y.-Y. Choi, S. J. Kang, H.-K. Kim, W. M. Choi, and S.-I. Na, "Multilayer graphene films as transparent electrodes for organic photovoltaic devices," *Solar Energy Materials and Solar Cells,* vol. 96, pp. 281-285, 2012.

[68] M. B. Avinash, K. S. Subrahmanyam, Y. Sundarayya, and T. Govindaraju, "Covalent modification and exfoliation of graphene oxide using ferrocene," *Nanoscale,* vol. 2, pp. 1762-1766, 2010.

[69] T. D. Dao, H.-I. Lee, H. M. Jeong, and B. K. Kim, "Direct covalent modification of thermally exfoliated graphene forming functionalized graphene stably dispersible in water and poly(vinyl alcohol)," *Colloid and Polymer Science,* vol. 291, pp. 2365-2374, 2013.

[70] G. Wei, M. Yan, R. Dong, D. Wang, X. Zhou, J. Chen, and J. Hao, "Covalent modification of reduced graphene oxide by means of diazonium chemistry and use as a drug-delivery system," *Chemistry - A European Journal,* vol. 18, pp. 14708-14716, 2012.

[71] S.-I. Na, B.-K. Yu, S.-S. Kim, D. Vak, T.-S. Kim, J.-S. Yeo, and D.-Y. Kim, "Fully spray-coated ITO-free organic solar cells for low-cost power generation," *Solar Energy Materials and Solar Cells,* vol. 94, pp. 1333-1337, 2010.

[72] T. V. Arjunan and T. S. Senthil, "Review: Dye sensitised solar cells," *Materials Technology,* vol. 28, pp. 9-14, 2013.

[73] M. R. Golobostanfard and H. Abdizadeh, "Hierarchical porous titania/carbon nanotube nanocomposite photoanode synthesized by controlled phase separation for dye sensitized solar cell," *Solar Energy Materials and Solar Cells,* vol. 120, Part A, pp. 295-302, 2014.

[74] A. Yella, H. W. Lee, H. N. Tsao, C. Yi, A. K. Chandiran, M. K. Nazeeruddin, E. W. G. Diau, C. Y. Yeh, S. M. Zakeeruddin, and M. Grätzel, "Porphyrin-

sensitized solar cells with cobalt (II/III)-based redox electrolyte exceed 12 percent efficiency," *Science,* vol. 334, pp. 629-634, 2011.

[75] A. Yella, H.-W. Lee, H. N. Tsao, C. Yi, A. K. Chandiran, M. K. Nazeeruddin, E. W.-G. Diau, C.-Y. Yeh, S. M. Zakeeruddin, and M. Grätzel, "Porphyrin-Sensitized Solar Cells with Cobalt (II/III)–Based Redox Electrolyte Exceed 12 Percent Efficiency," *Science,* vol. 334, pp. 629-634, November 4, 2011 2011.

[76] Y. Chuo, B. Omrane, C. Landrock, J. Aristizabal, D. Hohertz, S. V. Grayli, and B. Kaminska, "Powering the future: Organic solar cells with polymer energy storage," *IEEE Design and Test of Computers,* vol. 28, pp. 32-40, 2011.

[77] D. F. Zeigler, K.-S. Chen, H.-L. Yip, Y. Zhang, and A. K. Y. Jen, "Tunable light-harvesting polymers containing embedded dipolar chromophores for polymer solar cell applications," *Journal of Polymer Science, Part A: Polymer Chemistry,* vol. 50, pp. 1362-1373, 2012.

[78] A. Anctil, C. W. Babbitt, R. P. Raffaelle, and B. J. Landi, "Cumulative energy demand for small molecule and polymer photovoltaics," *Progress in Photovoltaics: Research and Applications,* vol. 21, pp. 1541-1554, 2013.

[79] A. B. Kaul, "Nano-enabled green technologies for electronics and energy applications," in *Nanotechnology 2012: Bio Sensors, Instruments, Medical, Environment and Energy - 2012 NSTI Nanotechnology Conference and Expo, NSTI-Nanotech 2012, June 18, 2012 - June 21, 2012*, Santa Clara, CA, United states, 2012, pp. 716-719.

[80] M. T. Khan, R. Bhargav, A. Kaur, S. K. Dhawan, and S. Chand, "Effect of cadmium sulphide quantum dot processing and post thermal annealing on P3HT/PCBM photovoltaic device," *Thin Solid Films,* vol. 519, pp. 1007-1011, 2010.

[81] S.-O. Kim, D. Sung Chung, H. Cha, J. Wan Jang, Y.-H. Kim, J.-W. Kang, Y.-S. Jeong, C. E. Park, and S.-K. Kwon, "Thermally stable organic bulk heterojunction photovoltaic cells incorporating an amorphous fullerene derivative as an electron acceptor," *Solar Energy Materials and Solar Cells,* vol. 95, pp. 432-439, 2011.

[82] K. Norrman, A. Ghanbari-Siahkali, and N. B. Larsen, "6 Studies of spin-coated polymer films," *Annual Reports Section "C" (Physical Chemistry),* vol. 101, pp. 174-201, 2005.

[83] S. Choi, B.-Y. Park, and H.-K. Jung, "Growth and characterization of sol-gel prepared Gd2O3 films as gate insulators for Zn-Sn-O thin film transistors," *Thin Solid Films,* vol. 535, pp. 291-295, 2013.

[84] R. Meier, M. A. Ruderer, A. Diethert, G. Kaune, V. Korstgens, S. V. Roth, and P. Muller-Buschbaum, "Influence of film thickness on the phase separation mechanism in ultrathin conducting polymer blend films," *Journal of Physical Chemistry B,* vol. 115, pp. 2899-2909, 2011.

[85] K. Arshak and O. Korostynska, *Advanced materials and techniques for radiation dosimetry*: Artech House, 2006.

[86] D. Morris, K. Arshak, A. A., and K. O., "Metal Oxide Nanostructures for Advanced Pressure Sensing Applications," in *Metal Oxide Nanostructures and Their Applications*, A. Umar and Y.-B. Hahn, Eds., ed: American Scientific Publishers, 2010, pp. 281-381.

[87] W. Yu, B. Xu, Q. Dong, Y. Zhou, J. Zhang, W. Tian, and B. Yang, "A two-step method combining electrodepositing and spin-coating for solar cell processing," *Journal of Solid State Electrochemistry,* vol. 14, pp. 1051-1056, 2010.

[88] M. Kitsara, D. Goustouridis, S. Chatzandroulis, M. Chatzichristidi, I. Raptis, T. Ganetsos, R. Igreja, and C. J. Dias, "Single chip interdigitated electrode capacitive chemical sensor arrays," *Sensors and Actuators, B: Chemical,* vol. 127, pp. 186-192, 2007.

[89] D. M. Snyder and P. Vadgama, "Impedance resonance: A novel technique for signal acquisition from interdigitated electrodes (IDE) in sensor applications," *IEEE Sensors Journal,* vol. 9, pp. 143-145, 2009.

[90] E. Valera, O. Casais, M. Vetter, and A. Rodriguez, "-Porous Silicon (PS) gas sensor based on interdigitated -electrodes (IDE's)," in *2007 Spanish Conference on Electron Devices, SCED, January 31, 2007 - February 2, 2007*, Madrid, Spain, 2007, pp. 197-200.

[91] K. Arshak and I. Gaidan, "Development of a novel gas sensor based on oxide thick films," in *EMRS 2004, Symposium D: Functional Oxides for Advanced Semiconductor Technologies*, 2005, pp. 44-49.

[92] D. T. Nguyen, M. T. Nguyen, G. T. Ho, T. N. Nguyen, S. Reisberg, B. Piro, and M. C. Pham, "Design of interpenetrated network MWCNT/poly(1,5-DAN) on interdigital electrode: Toward NO2 gas sensing," *Talanta,* vol. 115, pp. 713-717, 2013.

[93] M. Babaei and N. Alizadeh, "Methanol selective gas sensor based on nano-structured conducting polypyrrole prepared by electrochemically on interdigital electrodes for biodiesel analysis," *Sensors and Actuators, B: Chemical,* vol. 183, pp. 617-626, 2013.

[94] P. Teerapanich, M. T. Z. Myint, C. M. Joseph, G. L. Hornyak, and J. Dutta, "Development and improvement of carbon nanotube-based ammonia gas sensors

using ink-jet printed interdigitated electrodes," *IEEE Transactions on Nanotechnology,* vol. 12, pp. 255-262, 2013.

[95] T. Hibbard, K. Crowley, and A. J. Killard, "Direct measurement of ammonia in simulated human breath using an inkjet-printed polyaniline nanoparticle sensor," *Analytica Chimica Acta,* vol. 779, pp. 56-63, 2013.

[96] H. F. Hawari, N. M. Samsudin, A. Y. M. Shakaff, Y. Wahab, U. Hashim, A. Zakaria, S. A. Ghani, and M. N. Ahmad, "Highly selective molecular imprinted polymer (MIP) based sensor array using interdigitated electrode (IDE) platform for detection of mango ripeness," *Sensors and Actuators, B: Chemical,* vol. 187, pp. 434-444, 2013.

[97] T. Hofmann, K. Schroeder, J. Zacheja, and J. Binder, "Fluid characterization using sensor elements based on interdigitated electrodes," *Sensors and Actuators, B: Chemical,* vol. B37, pp. 37-42, 1996.

[98] X. Tang, D. Flandre, J.-P. Raskin, Y. Nizet, L. Moreno-Hagelsieb, R. Pampin, and L. A. Francis, "A new interdigitated array microelectrode-oxide-silicon sensor with label-free, high sensitivity and specificity for fast bacteria detection," *Sensors and Actuators, B: Chemical,* vol. 156, pp. 578-587, 2011.

[99] K.-L. Chen, S. Wang, J. C. Salvia, R. Melamud, R. T. Howe, and T. W. Kenny, "Wafer-level epitaxial silicon packaging for out-of-plane RF MEMS resonators with integrated actuation electrodes," *IEEE Transactions on Components, Packaging and Manufacturing Technology,* vol. 1, pp. 310-317, 2011.

[100] G. Mottet, J. Villemejane, L. M. Mir, and B. L. Pioufle, "A technique to design complex 3D lab on a chip involving multilayered fluidics, embedded thick electrodes and hard packaging - Application to dielectrophoresis and

electroporation of cells," *Journal of Micromechanics and Microengineering,* vol. 20, 2010.

[101] A. Crew, D. Lonsdale, N. Byrd, R. Pittson, and J. P. Hart, "A screen-printed, amperometric biosensor array incorporated into a novel automated system for the simultaneous determination of organophosphate pesticides," *Biosensors and Bioelectronics,* vol. 26, pp. 2847-2851, 2011.

[102] K. Arshak and O. Korostynska, "Thin- and thick-film real-time gamma radiation detectors," *IEEE Sensors Journal,* vol. 5, pp. 574-580, 2005.

[103] N.-J. Choi, H.-K. Lee, S. E. Moon, W. S. Yang, and J. Kim, "Volatile organic compound gas sensor based on aluminum-doped zinc oxide with nanoparticle," *Journal of Nanoscience and Nanotechnology,* vol. 13, pp. 5481-5484, 2013.

[104] M. Choudhary, N. K. Singh, V. N. Mishra, and R. Dwivedi, "Selective detection of hydrogen sulfide using copper oxide-doped tin oxide based thick film sensor array," *Materials Chemistry and Physics,* vol. 142, pp. 370-380, 2013.

[105] S. E. Moon, H. K. Lee, N. J. Choi, J. Lee, C. A. Choi, W. S. Yang, J. Kim, J. J. Jong, and D. J. Yoo, "Low power consumption micro C2H5OH gas sensor based on micro-heater and screen printing technique," *Sensors and Actuators, B: Chemical,* vol. 187, pp. 598-603, 2013.

[106] A. J. M. Frood, S. P. Beeby, M. J. Tudor, and N. M. White, "Photoresist patterned thick-film piezoelectric elements on silicon," *Journal of Electroceramics,* vol. 19, pp. 327-331, 2007.

[107] P. M. Faia, C. S. Furtado, and A. J. Ferreira, "Humidity sensing properties of a thick-film titania prepared by a slow spinning process," *Sensors and Actuators, B: Chemical,* vol. 101, pp. 183-190, 2004.

[108] A. Lozinski, "Thin pyroelectric PLZT film obtained with sol-gel technology," *Journal of Electroceramics,* vol. 19, pp. 303-306, 2007.

[109] B. M. Austin, "Thick-film screen printing," *Solid State Technology,* vol. 12, pp. 53-58, 1969.

[110] G. Galbiati, V. D. Mihailetchi, A. Halm, R. Roescu, and R. Kopecek, "Results on n-type IBC solar cells using industrial optimized techniques in the fabrication processing," in *1st International Conference on Crystalline Silicon Photovoltaics, SiliconPV 2011, April 17, 2011 - April 20, 2011*, Freiburg, Germany, 2011, pp. 421-426.

[111] S. Joo and D. F. Baldwin, "Advanced package prototyping using nano-particle silver printed interconnects," *IEEE Transactions on Electronics Packaging Manufacturing,* vol. 33, pp. 129-134, 2010.

[112] A. Hobby, *Printing Thick Film Hybrids*: DEK Printing Machines Ltd, 1997.

[113] D. A. Alsaid, E. Rebrosova, M. Joyce, M. Rebros, M. Atashbar, and B. Bazuin, "Gravure printing of ITO transparent electrodes for applications in flexible electronics," *IEEE/OSA Journal of Display Technology,* vol. 8, pp. 391-396, 2012.

[114] J.-W. Kang, S.-P. Lee, D.-G. Kim, S. Lee, G.-H. Lee, J.-K. Kim, S.-Y. Park, J. H. Kim, H.-K. Kim, and Y.-S. Jeong, "Reduction of series resistance in organic photovoltaic using low sheet resistance of ITO electrode," *Electrochemical and Solid-State Letters,* vol. 12, pp. H64-H66, 2009.

[115] K. Lim, S. Jung, J.-K. Kim, J.-W. Kang, J.-H. Kim, S.-H. Choa, and D.-G. Kim, "Flexible PEDOT: PSS/ITO hybrid transparent conducting electrode for organic photovoltaics," *Solar Energy Materials and Solar Cells,* vol. 115, pp. 71-78, 2013.

[116] G. Zha, H. Zhou, J. Gao, T. Wang, and W. Jie, "The growth and the interfacial layer of CdZnTe nano-crystalline films by vacuum evaporation," *Vacuum,* vol. 86, pp. 242-245, 2011.

[117] M. L. Vega, H. Libardi, R. M. Faria, R. F. Bianchi, and A. Marletta, "Surface morphology, optical and electrical characterization of poly(p-phenylenevinylene) multilayer films," in *2005 12th International Symposium on Electrets, ISE 12, September 11, 2005 - September 14, 2005*, Salvador, Bahia, Brazil, 2005, pp. 520-523.

[118] M. Voigt, J. Pflaum, and M. Sokolowskr, "Growth morphologies and charge carrier mobilities of pentacene organic field effect transistors with rf sputtered aluminium oxide gate insulators on ITO glass," *Physica Status Solidi (A) Applications and Materials Science,* vol. 205, pp. 449-460, 2008.

[119] K. Arshak, O. Korostynska, J. Harris, D. Morris, A. Arshak, and E. Jafer, "Properties of BGO thin films under the influence of gamma radiation," *Thin Solid Films,* vol. 516, pp. 1493-1498, 2008.

[120] K.-S. Shin, H.-J. Park, B. Kumar, K.-K. Kim, S.-G. Ihn, and S.-W. Kim, "Low-temperature growth and characterization of ZnO thin films for flexible inverted organic solar cells," *Journal of Materials Chemistry,* vol. 21, pp. 12274-12279, 2011.

[121] S. Tamulevicius, "Stress and strain in the vacuum deposited thin films," *Vacuum,* vol. 51, pp. 127-139, 1998.

[122] J. Wu, F. Ang, C. Zhao, and J. S. Smith, "Electrical properties of N-type CdS and P-type CdTe thin films in CdS/CdTe solar cells," in *2013 20th IEEE International Symposium on the Physical and Failure Analysis of Integrated*

Circuits, IPFA 2013, July 15, 2013 - July 19, 2013, Suzhou, China, 2013, pp. 385-389.

[123] A. M. Whited and P. S. H. Park, "Atomic force microscopy: A multifaceted tool to study membrane proteins and their interactions with ligands," *Biochimica et Biophysica Acta (BBA) - Biomembranes,* vol. 1838, pp. 56-68, 2014.

[124] D. H. Staelin;, A. W. Morgenthaler;, and J. A. Kong, *Electromagnetic waves*. Englewood Cliffs, N.J.: Prentice Hall, 1998.

[125] S. Grimnes and Ø. G. Martinsen, "Chapter 3 - DIELECTRICS," in *Bioimpedance and Bioelectricity Basics (Second Edition)*, ed New York: Academic Press, 2008, pp. 57-92.

[126] D. M. Pozar, *Microwave engineering*: Wiley, 1997.

[127] C. A. Balanis, *Antenna Theory: Analysis and Design*, 3rd ed. Hoboken, New Jersey: John Wiley & Sons, 2005.

[128] O. Korostynska, A. Mason, and A. I. Al-Shammaa, "Flexible microwave sensors for real-time analysis of water contaminants," *Journal of Electromagnetic Waves and Applications,* vol. 27, pp. 2075-2089, 2013.

[129] O. Korostynska, K. Arshak, V. Velusamy, A. Arshak, and A. Vaseashta, "Recent Advances in Point-of-Access Water Quality Monitoring," in *NATO Advanced Study Institute on Technological Innovations in Detection and Sensing of Chemical, Biological, Radiological, Nuclear - (CBRN) Threats and Ecological Terrorism, 6-17 June 2010*, Dordrecht, Netherlands, 2012, pp. 261-8.

[130] O. Korostynska, A. Mason, and A. I. Al-Shamma'A, "Proof-of-concept microwave sensor on flexible substrate for real-time water composition analysis," in *2012 6th International Conference on Sensing Technology, ICST*

2012, December 18, 2012 - December 21, 2012, Kolkata, India, 2012, pp. 547-550.

[131] B. Kapilevich and B. Litvak, "Microwave sensor for accurate measurements of water solution concentrations," in *APMC Asia-Pacific Microwave Conference*, Bangkok, 2007, pp. 1-4.

[132] M. Ortoneda-Pedrola, O. Korostynska, A. Mason, and A. I. Al-Shamma'A, "Real-time sensing of NaCl solution concentration at microwave frequencies using novel Ag patterns printed on flexible substrates," in *17th Conference in the biennial Sensors and Their Applications, September 16, 2013 - September 18, 2013*, Dubrovnik, Croatia, 2013.

[133] M. Ortoneda-Pedrola, O. Korostynska, A. Mason, and A. I. Al-Shamma'A, "Real-time microwave sensor for KCl, MnCl2 and CuCl solutions concentration with Ag patterns printed on flexible substrates," in *17th Conference in the biennial Sensors and Their Applications, September 16, 2013 - September 18, 2013*, Dubrovnik, Croatia, 2013.

[134] J. D. Boon and J. M. Brubaker, "Acoustic-microwave water level sensor comparisons in an estuarine environment," in *OCEANS*, Quebec, Canada, 2008, pp. 1-5.

[135] B. Jackson and T. Jayanthy, "A novel method for water impurity concentration using microstrip resonator sensor," in *Recent Advances in Space Technology Services and Climate Change (RSTSCC)*, Chennai, India., 2010, pp. 376-379.

[136] C. Bernou, D. Rebière, and J. Pistré, "Microwave sensors: a new sensing principle. Application to humidity detection," *Sensors and Actuators B: Chemical,* vol. 68, pp. 88-93, 2000.

[137] T. Nacke, A. Barthel, C. Pflieger, U. Pliquett, D. Beckmann, and A. Goller, "Continuous process monitoring for biogas plants using microwave sensors," in *12th Biennial Baltic Electronics Conference (BEC)* Tallinn, Estonia, 2010, pp. 239-242.

[138] K. Y. You, J. Salleh, Z. Abbas, and L. L. You, "A rectangular patch antenna technique for the determination of moisture content in soil," in *Progress in Electromagnetics Research Symposium, PIERS 2010 Cambridge, July 5, 2010 - July 8, 2010*, Cambridge, MA, United states, 2010, pp. 850-854.

[139] A. Mason, O. Korostynska, S. Wylie, and A. I. Al-Shamma'a, "Non-destructive evaluation of an activated carbon using microwaves to determine residual life," *Carbon,* vol. 67, pp. 1-9, 2014.

[140] O. Korostynska, A. Arshak, P. Creedon, K. Arshak, L. Wendling, A. I. Al-Shamma'a, and S. O'Keeffe, "Glucose monitoring using electromagnetic waves and microsensor with interdigitated electrodes," in *IEEE Sensors Applications Symposium, SAS*, New Orleans, LA, USA, 2009, pp. 34-37.

[141] A. Mason, S. Wylie, A. Thomas, H. Keele, A. Shaw, and A. Al-Shamma'a, "HEPA Filter Material Load Detection Using a Microwave Cavity Sensor," *International Journal on Smart Sensing and Intelligent Systems,* vol. 3, pp. 322-337, Sep 2010.

[142] A. Al-Shamma'a, A. Mason, and A. Shaw, "Patent: Non-Invasive Monitoring Device," US2012150000 (A1), WO2010131029 (A1), EP2429397 (A1), 2012.

[143] A. Mason, O. Korostynska, and A. I. Al-Shamma'a, "Microwave Sensors for Real-Time Nutrients Detection in Water," in *Smart Sensors for Real-Time Water Quality Monitoring*, S. C. Mukhopadhyay and A. Mason, Eds., ed: Springer Berlin Heidelberg, 2013, pp. 197-216.

[144] E. M. Georgiadou, A. D. Panagopoulos, and J. D. Kanellopoulos, "Millimeter Wave Pulse Propagation through Distorted Raindrops for LOs Fixed Wireless Access Channels," *Journal of Electromagnetic Waves and Applications,* vol. 20, pp. 1235-1248, 2006/01/01 2006.

[145] Z. Wu, B. Fan, A. Li, F. Xue, and J. Ouyang, "Low-band gap copolymers of ethynylfluorene and 3,6-dithiophen-2-yl-2,5-dihydropyrrolo[3,4-c]pyrrole-1,4-dione synthesized under microwave irradiation for polymer photovoltaic cells," *Organic Electronics,* vol. 12, pp. 993-1002, 2011.

[146] W. N. Liu, Y. Yang, and K. M. Huang, "A Radio Frequency Sensor For Measurement Of Small Dielectric Property Changes," *Journal of Electromagnetic Waves and Applications,* vol. 26, pp. 1180-1191, 2012/06/01 2012.

[147] R. Simons, *Coplanar Waveguide Circuits, Components, and Systems*: John Wiley & Sons, 2001.

[148] D. M. Pozar, "Microwave resonator," in *Microwave Engineering*, Second ed: John Wiley & Sons, inc, 1998, pp. 313-323.

[149] R. Bansal, *Handbook of engineering electromagnetics*. USA: Marcel Dekker, 2005.

[150] D. M. Pozar, "Circular Waveguide," in *Microwave Engineering*, 3rd ed New York: John Wiley and Sons, 2005, pp. 119-20.

[151] P. Kumar, D. M. Kim, M. H. Hyun, and Y.-B. Shim, "An all-solid-state monohydrogen phosphate sensor based on a macrocyclic ionophore," *Talanta,* vol. 82, pp. 1107-1112, 2010.

[152] M. Mehdizadeh, *Microwave/RF Applicators and Probes for Material Heating, Sensing, and Plasma Generation*: William Andrew, 2010.

[153] U. A. Bakshi and A. V. Bakshi, *Transmission lines and waveguide*: Technical Publications Pune, 2008.

[154] V. Guillard, M. Mauricio-Iglesias, and N. Gontard, "Effect of novel food processing methods on packaging: Structure, composition, and migration properties," *Critical Reviews in Food Science and Nutrition,* vol. 50, pp. 969-988, 2010.

[155] J. Goh, "Real Time Water Pipes Leak Detection Using Electromagnatic Waves for The Water Industry," 2011.

[156] L. H. Chua and D. Mirshekar-Syahkal, "Accurate and direct characterization of high-Q microwave resonators using one-port measurement," *Microwave Theory and Techniques,* vol. 51, pp. 978-985, 2003.

[157] J. Lee and K. Sarabandi, "Synthesizing microwave resonator filters," *Microwave Magazine, IEEE,* vol. 10, pp. 57-65, 2009.

[158] R. C. Taber and C. A. Flory, "Microwave oscillators incorporating cryogenic sapphire dielectric resonators," *Ultrasonics, Ferroelectrics and Frequency Control,* vol. 42, pp. 111-119, 1995.

[159] L. Wendling, J. D. Cullen, A. Al-Shamma'a, and A. Shaw, "HFSS Analysis of Online Electromagnetic Wave Alcohol Sensor," presented at the GERI Annual Research Symposium, Liverpool, UK, 2008.

[160] J. H. Goh, A. Mason, A. I. Al-Shamma'a, M. Field, M. Shackloth, and P. Browning, "Non Invasive Microwave Sensor for the Detection of Lactic Acid in Cerebrospinal Fluid (CSF)," presented at the Sensors and their Applications XVI, Cork, Ireland, 2011.

[161] A. J. Cano, P. J. Plaza-Gonzalez, F. Penaranda-Foix, and J. M. Catala-Civera, "Non-invasive Microwave Sensors for the Monitoring of the state of Liquids

Used in the Polyurethane Industry," in *International Conference on Sensor Technologies and Applications.*, 2007, pp. 56-61.

[162] J. Sheen, "Measurements of microwave dielectric properties by an amended cavity perturbation technique," *Measurement,* vol. 42, pp. 57-61, 2009.

[163] M. J. Prest, Y. Wang, F. Huang, and M. J. Lancaster, "Tuning of a superconducting microwave resonator at 77 K using an integrated micromachined silicon vertical actuator," *Journal of Micromechanics and Microengineering,* vol. 20, 2010.

[164] C. O. Kappe, A. Stadier, and D. dallinger, *Microwaves in organic and medical chemistry*, second ed. Austria: John Wiely & sons, 2012.

[165] Y. Carmel, K. Minami, W. Lou, R. A. Kehs, and W. W. Destler, "High-power microwave generation by excitation of a plasma-filled rippled boundary resonator," *Plasma Science,* vol. 18, pp. 497-506, 1990.

[166] A. Gokhale, *Introduction To Telecommunications*, second edition ed.: Thomson Delmar, 2004.

[167] N. Baloian, J. A. Pino, and H. U. Hoppe, "Dealing with the students' Attention Problem in computer supported face-to-face lecturing," *Education Technology & Society,* vol. 11, pp. 192-205, 2008.

[168] D. M. Pozar, "Microwave Engineering ", 3rd ed New York: John Wiley and Sons, 2005, pp. 143-149.

[169] P. K. Kundu, A. Chatterjee, and P. C. Panchariya, "Electronic Tongue System for Water Sample Authentication: A Slantlet-Transform-Based Approach," *Instrumentation and Measurement, IEEE Transactions on,* vol. 60, pp. 1959-1966, 2011.

[170] E. Garcia-Breijo, J. Atkinson, J. Garrigues, L. Gil, J. Ibanez, M. Glanc, and C. Olguin, "An electronic tongue for monitoring drinking waters using a fuzzy ARTMAP neural network implemented on a microcontroller," in *Industrial Electronics (ISIE), 2011 IEEE International Symposium on*, 2011, pp. 1270-1275.

[171] F. Völgyi, "Microstrip Transmission- and Reflection-Type Sensors Used in Microwave Aquametry," in *Electromagnetic Aquametry*, K. Kupfer, Ed., ed: Springer Berlin Heidelberg, 2005, pp. 243-256.

[172] A. Zucchelli, M. Chimenti, E. Bozzi, and P. Nepa, "Application of a Coaxial-fed Patch to Microwave Non-Destructive Porosity Measurements in Low-Loss Dielectrics," *Progress In Electromagnetics Research M,* vol. 5, pp. 1-14, 2008.

[173] U. Kaatze, "Electromagnetic Wave Interactions with Water and Aqueous Solutions," in *Electromagnetic Aquametry*, K. Kupfer, Ed., ed: Springer Berlin Heidelberg, 2005, pp. 15-37.

[174] S. Sardeshpande and A. Chatterjee, "Electromagnetic Wave Propagation in Linearly Dispersive Media Using Higher-Order Weno Scheme," *Journal of Electromagnetic Waves and Applications,* vol. 23, pp. 2135-2142, 2009/01/01 2009.

[175] D. A. Boyarskii, V. V. Tikhonov, and N. Y. Komarova, "Model of Dielectric Constant of Bound Water in Soil for Applications of Microwave Remote Sensing," *Journal of Electromagnetic Waves and Applications,* vol. 16, pp. 411-412, 2002/01/01 2002.

[176] D. Kajfez, "Temperature characterization of dielectric-resonator materials," *Journal of the European Ceramic Society,* vol. 21, pp. 2663-2667, 2001.

[177] O. Korostynska, A. Mason, and A. I. Al-Shamma'a, "Flexible microwave sensors for real-time analysis of water contaminants," *Journal of Electromagnetic Waves and Applications,* vol. 27, pp. 2075-2089, 2013/11/01 2013.

[178] C. A. Balanis, *Antenna Theory: Analysis and Design* 3rd ed. United States: Wiley-Blackwell, 2005.

[179] D. Guha and Y. M. M. Antar, *Microstrip and Printed Antennas: New Trends, Techniques and Applications*. Chichester, West Sussex, United Kingdom: Wiley, 2010.

[180] S. Couris, E. Koudoumas, F. Dong, and S. Leach, "Nonlinear optical properties of fullerenes," in *Proceedings of the 1996 Conference on Lasers and Electro-Optics Europe, CLEO/Europe, September 8, 1996 - September 13, 1996*, Hamburg, Ger, 1996, p. 292.

[181] S. Couris, E. Koudoumas, A. A. Ruth, and S. Leach, "Concentration and wavelength dependence of the effective third order susceptibility and optical limiting of C60 in toluene solution," *Journal of Physics B: Atomic, Molecular and Optical Physics,* vol. 2, pp. 4537-4554, 1995.

[182] E. Koudoumas, F. Dong, S. Couris, and S. Leach, "High order nonlinear optical response of fullerene solutions in the nanosecond regime," *Optics Communications,* vol. 138, pp. 301-304, 1997.

[183] C. Bounioux, R. Itzhak, R. Avrahami, E. Zussman, J. Frey, E. A. Katz, and R. Yerushalmi-Rozen, "Electrospun fibers of functional nanocomposites composed of single-walled carbon nanotubes, fullerene derivatives, and poly(3-hexylthiophene)," *Journal of Polymer Science, Part B: Polymer Physics,* vol. 49, pp. 1263-1268, 2011.

[184] L. Oneill, P. J. Lynch, N. McGoldrick, H. J. Byrne, and M. McNamara, "Kinetic studies of the photo-degradation of poly(arylene vinylenes)," *Journal of Luminescence,* vol. 132, pp. 2217-2223, 2012.